Annual Report 2016

Institute for Pulsed Power and Microwave Technology
Institut für Hochleistungsimpuls- und Mikrowellentechnik

John Jelonnek (Ed.)

KIT Scientific Publishing

John Jelonnek (Ed.)

Annual Report 2016

Institute for Pulsed Power and Microwave Technology
Institut für Hochleistungsimpuls- und Mikrowellentechnik

Karlsruhe Institute of Technology

KIT SCIENTIFIC REPORTS 7745

Annual Report 2016

Institute for Pulsed Power and Microwave Technology
Institut für Hochleistungsimpuls- und Mikrowellentechnik

Edited by
John Jelonnek

Report-Nr. KIT-SR 7745

Impressum

⊿KIT Scientific Publishing

Institute for Pulsed Power and Microwave Technology (IHM)

Institut für Hochleistungsimpuls- und Mikrowellentechnik (IHM)

Director: Prof. Dr.-Ing. John Jelonnek

The Institute for Pulsed Power and Microwave Technology (Institut für Hochleistungsimpuls- und Mikrowellentechnik (IHM)) is doing research in the areas of pulsed power and high-power microwave technologies. Both, research and development of high power sources as well as related applications are in the focus. Applications for pulsed power technologies are ranging from materials processing Jto bioelectrics. High power microwave technologies are focusing on RF sources (gyrotrons) for electron cyclotron resonance heating of magnetically confined plasmas and on applications for materials processing at microwave frequencies.

The IHM is doing research, development, academic education, and, in collaboration with the KIT Division IMA and industrial partners, the technology transfer. The IHM is focusing on the long term research goals of the German Helmholtz Association (HGF). During the ongoing program oriented research period (POF3) of HGF (2015 – 2020), IHM is working in the research field ENERGY. Research projects are running within following four HGF programs: "Energy Efficiency, Materials and Resources (EMR)"; "Nuclear Fusion (FUSION)", "Nuclear Waste Management, Safety and Radiation Research (NUSAFE)" and "Renewable Energies (RE)".

During 2016, R&D work has been done in the following areas: fundamental theoretical and experimental research on the generation of intense electron beams, strong electromagnetic fields and their interaction with biomass, materials and plasmas; application of those methods in the areas of energy production through controlled thermonuclear fusion in magnetically confined plasmas, in material processing and in energy technology.

Mentioned long-term research areas require the profound knowledge on modern electron beam optics, high power micro- and millimeter waves, sub-THz technologies, vacuum electronics, material technologies, high voltage technologies and high voltage measurement techniques.

Department for Pulsed Power Technologies:

(Head: Prof. Dr.-Ing. Georg Müller)

In environmental- and bio-technology the research is devoted to pulsed power technology in the Giga Watt range. The research is concerned with short pulse (µs) - and with ultra-short pulse (ns) treatment of biological cells (electroporation). The focus is related to large-scale applications, treatment of large volumes, to realization high component life time and overall process integration. Research directions of the work are the electroporation of biological cells for extraction of cell contents (PEF- process), the dewatering and drying of green biomass, the pre-treatment of micro algae for further energetic use and sustainable reduction of bacteria in contaminated effluents. Another key research topic is related to the surface modification and corrosion protection of metals and alloys using high-energy, large-area pulsed electron beams (GESA process). The research is focused on electron beam physics, the interaction of electron beams with material surfaces and the corresponding investigations on material specific characterization. The goal is to develop a corrosion barrier for improved compatibility of structural materials in contact with liquid metal coolants (Na, Sn, Pb or PbBi). (Programs: EE, NUSAFE).

In the area of PEF-assisted microalgae downstream processing, it could be shown that parasitic microalgae precipitation is controlled by the cell's zeta potential. Appropriate adjustment of the zeta potential and the application of short pulses of several microseconds and shorter can impede unwanted biomass deposition at the electrodes of the treatment chamber. Protocols for lipid extraction from wet microalgae biomass were optimized for recovery rates of up to 97% of the lipid inventory. Preceding analysis of various reference methods for absolute lipid content determination revealed, that Soxhlet extraction with Hexane is the most suited method. Investigations on basic effects of nsPEF stress responses demonstrated, that nsPEF treatment at non-lethal doses can arrest cell cycle and cause pamella states due to oxidative bursts. Optimization of cultivation strategy reduced microalgae suspension conductivity by a factor of more than 3, which is an important step for further improving energy-efficiency of PEF-assisted microalgae processing.

Efforts to elevate PEF-processing to a new technology platform of operator-friendly semiconductor (SC) based pulsed power generators has been approached. The use of power SCs as pulse switches allows for significantly higher pulse repetition rates at moderate voltage levels at a given specific processing energy. Hence, generator size can be reduced accordingly. Currently, a 30-stage pulse generator with 30 kV rated output voltage and 600 A peak pulse current has been set up.

The use of liquid metals as heat-transfer- and storage media for CSP is a new research area started 2015 in the frame of POF3. In addition to Na, Pb-alloys and Sn are investigated as possible CSP heat transfer materials. Based on fundamental aspects of material liquid metal compatibility material concepts and related experimental investigations are the major target of research. Surface alloying of materials using pulsed electron beams is the technology for corrossion barrier development. Therefore, in-situ diagnostics of beam formation and target beam interaction are targeted combining experimental work and simulations using MAGIC3D, COMSOL and other software tools.

The aim of the institute's contribution, in the field of transmutation of radiactive waste (NUSAFE program), is the development of a suitable corrosion protection especially for parts under high loads like fuel claddings or pump materials in contact with liquid Pb or PbBi. Pulsed large area electron beams (GESA) are used to modify the surface of steels such that they fulfill the requirements of their surrounding environment. Corrosion test stands for exposure of specimens under relevant conditions are developed and operated. Test facilities for combined loads like erosion and corrosion and fretting corrosion were developed, built and operated. Conditioning the Pb with regard to its oxygen concentration and the transport of oxygen in PbBi are additional aspects of the work.

Department for High Power Microwave Technologies:
(Head: Dr. Gerd Gantenbein)

The Department for High Power Microwavea Technologies is focusing on the research and development of high power RF sources (gyrotrons) and related components for electron cyclotron resonance heating and current drive (ECRH&CD) of magnetically confined nuclear fusion plasmas. Additionally, it is doint research and development in the field of and on the application of microwaves to chemical processes, materials and composites.

- Collaboration within the W7-X project PMW for planning, construction and testing of the 10 MW CW, 140 GHz electron cyclotron resonance heating (ECRH) system for the stellarator W7-X at IPP Greifswald. In particular, the 1 MW CW, 140 GHz gyrotrons have been developed in cooperation with EPFL-CRPP Lausanne and Thales Electron Devices (TED), Vélizy, France. In 2015, the last gyrotron of the initial installation has been delivered to KIT for FAT test. The final SAT and FAT tests are expected at IPP Greifswald for 2016. Start of operation and first plasma in the Wendelstein 7-X fusion research device at IPP Greifswald has been at December 10, 2015.

- Within the European GYrotron Consortium (EGYC) and in collaboration with its industrial partner Thales Electron Devices (TED), Vélizy, France, EGYC is developing gyrotrons for the International Thermonuclear Experimental Reactor (ITER). According to a change in the delivery strategy for ITER, Europe will provide a total of 6 MW CW RF power at 170 GHz for the 24 MW CW ECRH system. Fusion for Energy (F4E) is coordinating the project. Institutional partners are CNR, Italy, EPFL-CRPP, Switzerland and HELLAS, Greece. In 2015, the testing of the 1 MW 170 GHz short-pulse gyrotron has been completed. This gyrotron has fulfilled all required key performance parameters. Additionally, the first CW prototype has been delivered to KIT during 4th quarter of 2015. Tests are expected for 2016.

- KIT is pushing forward the development of multi-MW (2 MW) coaxial-cavity gyrotrons in frame of EUROfusion and as prerequisite for future DEMO gyrotrons. In 2015, the tube has been upgraded, extensive design work has been performed, aiming at long pulse operation of the existing coaxial gyrotron by introducing advanced cooling systems to the components.

- In frame of EUROfusion, KIT has continued its investigations on advanced gyrotrons for future DEMO. Target is the design of an 240 GHz gyrotron with frequency step-tunability and the possibility for operation at 170 GHz and 204 GHz additionally. In 2015 the design of coaxial cavity gyrotron and, alternatively, a conventional cavity gyrotron has been progressed. Studies on multi-staged depressed collectors which have the potential of significantly increasing the gyrotron efficiency have been continued.

- In the frame of studies of advanced technologies for future high-power gyrotrons a methodology has been progressed to determine the emitter emission homogeneity from the measurement of the current voltage characteristics of a magnetron injection gun. Within this work the influence of trapped electrons and low frequency oscillations on the operation of a gyrotron has been studied.

- KIT is in collaboration with EPFL-CRPP, Lausanne, to design a new (126 GHz / 84 GHz) dual-frequency 1 MW gyrotron based on design of ITER for TCV tokamak. In 2015, interaction calculations for the design of the cavity have beeen performed and simulations and design of a triode MIG have been completed.

- The erection of the new gyrotron test facility, FULGOR, with up to 10 MW electrical power has been progressed. The final design of the high voltage power supply has been agreed with the manufacturer and substantial progress has been achieved in the planning of several auxiliary systems for plant operation.

- The possibilities for in-situ dielectric characterization have been extended towards chemical reactions in pressurized liquids and dispersions. In addition to that, a Fabry Perot resonator has been developed for dielectric characterization of low loss solids and liquids within the Ku-Band.

- New research activities in the field of microwave plasma chemistry have been initiated. For experimental investigations a new lab was established that so far comprised a 6 kW atmospheric plasma source as well as an optical emission spectrometer.

- Systematic investigations on microwave assisted extraction of oil from micro algae by use of a special lab-scale applicator design demonstrated promising results with respect to energy efficiency and degree of extraction.

- The ZIM project "Development of selective microwave assisted gluing of textile leather to plastic base plates" has been successfully finished. Based on the convincing results the application for a follow-up project with additional industrial partners has been initiated.

- Within the H2020-SPIRE-2015 project SYMBIOPTIMA an optimised industrial-scale reactor design for the energy efficient microwave assisted depolymerisation has been developed.

- A new technology transfer project has been started with the license partner Vötsch Industrietechnik GmbH to further improve the HEPHAISTOS technology by use of novel control algorithms.

Table of Contents

1 Nuclear Fusion (FUSION): Plasma Heating Systems – Microwave Plasma Heating & Current Drive Systems –

1.1 Microwave Heating System for W7-X (PMW)

Electron cyclotron resonance heating (ECRH) and current drive (ECCD) are the standard methods for localized heating and current drive in future fusion experiments and the only CW heating methods available today. Thus, ECRH will be the basic day-one heating system for the stellarator W7-X which started operation end of 2015 at IPP Greifswald. The ECRH system for W7-X and the project PMW were finalized in 2016. In its first stage W7-X will be equipped with a 10 MW ECRH system operating at 140 GHz in continuous wave (CW).

The complete ECRH system is coordinated by the project "Projekt Mikrowellenheizung für W7-X (PMW)". PMW has been established by KIT together with IPP and several EU partners in 1998. The responsibility of PMW covers the design, development, construction, installation and system tests of all components required for stationary plasma heating on site at IPP Greifswald. PMW coordinates the contribution from Institute of Interfacial Process Engineering and Plasma Technology (IGVP) of the University of Stuttgart too. IGVP is responsible for the microwave transmission system and part of the power supply (HV-system). IPP Greifswald is responsible for the in-vessel components and for the in-house auxiliary systems. PMW benefits from the collaboration with Swiss Plasma Center (SPC, former Centre de Recherche de Physique des Plasmas, CRPP) Lausanne, Commissariat à l´Energie Atomique (CEA), Cadarache and Thales Electron Devices (TED), Vélizy.

Additional to the successfully running two prototypes, seven series gyrotrons have been ordered from the industrial partner Thales Electron Devices (TED), Vélizy. First operation and long pulse conditioning of these gyrotrons is being performed at the teststand at KIT. Pulses up to 180 s duration at full power are possible (factory acceptance test, FAT) whereas 30 minutes shots at full power are possible at IPP (necessary for site acceptance test, SAT). Including the pre-prototype tube, the prototype tube and a 140 GHz CPI tube, in total 10 gyrotrons will be available for W7-X. To operate these gyrotrons eight superconducting magnet systems have been manufactured at Cryomagnetics Inc., Oak Ridge, USA and in addition one system at Oxford Instruments and Accel.

In 2016 the Site Acceptance Tests of the TED series gyrotron SN5i could be finished successfully at IPP Greifswald. Stable operation of the tube at RF power of 900 kW has been shown and quasi steady state operation (1440 s) at full power has been demonstrated. Since 2016 there are 8 TED Gyrotrons operable on site at IPP Greifswald with a total RF power above 7000 kW.

Due to successful operation, IPP ordered an additional series gyrotron (SN8). Delivery and installation is expected for 2017.

The ECRH system has been used as regular plasma start-up and heating system for the first Hydrogene experimental campaign of W7-X. With the ECRH system up to 6 MW RF power has been injected into the plasma, reliable plasma operation has been achieved up to 6 s.

1.2   Experimental Verification of the EU 170GHz, 1MW industrial prototype gyrotron for ITER

1.2.1   Introduction

The European GYrotron Consortium (EGYC), in cooperation with its industrial partner Thales Electron Devices (TED), has designed and developed the EU 1 MW - 170 GHz gyrotron for ECH&CD on ITER, under the coordination of the European domestic agency F4E. According to the project strategy followed by F4E, two prototypes were developed. The first one is a modular short-pulse (SP) prototype tube built for validating the design, in terms of generated RF power, efficiency and quality of the RF output beam of the main gyrotron components for millisecond pulses. The second prototype is a long-pulse industrial tube with the additional goal to fulfill the ITER requirements in terms of pulse length and continuous wave (CW) operation regime. The technological design of the gyrotron was decided to resemble as much as possible the 1 MW, 140 GHz CW Wendelstein W7-X gyrotron in order to take advantage of the experience gained during the manufacturing of the 7 tubes of the industrial series production (+2 prototypes). The CW tube was delivered to KIT and prepared for the operation at the beginning of 2016. The first experiments with the goal to optimize the operation of the CW prototype in the short-pulse regime started in February 2016. In June 2016 preparation for the CW operation of the tube started with the goal to extend the pulse duration up to 3 minutes. The tests with the 1MW CW prototype will be continued at longer pulse lengths in the European Gyrotron Test Stand at EPFL-SPC in Lausanne.

1.2.2   Delivery and installation

The 1MW, CW gyrotron prototype has been delivered at KIT on January 18, 2016 together with all the necessary auxiliaries, such as the collector water jacket, the longitudinal and transversal sweeping coils and ion-getter pump power supplies (Fig. 1.2.1). After delivery the shock sensors have been examined thoroughly and it was confirmed that there were no incidents during the transportation from Velizy to Karlsruhe. In order to check the internal pressure of the tube, a power supply has been connected to one of the Ion-Getter-Pumps of the gyrotron and the measured current was found smaller than 10^{-7} A ($< 10^{-9}$ mbar), confirming the excellent vacuum conditions of the tube. Fig. 1.2.2 shows the gyrotron after installation in the cryostat and connection of all auxiliaries and cooling systems.

Fig. 1.2.1: Delivery and unpacking of the gyrotron

Fig. 1.2.2: First industrial ITER gyrotron after final installation at KIT in the OI Magnet.

1.2.3 Preparation for the experiments

Magnetic field alignment

Before the gyrotron was installed in the magnet, a verification of the alignment magnetic field axis of the magnet, was performed by using the measurement equipment available at KIT. The device consists of a system of hall-probes that deliver the information of the magnetic field components in longitudinal and radial direction. By moving of the probe along the mechanical axis of the magnet and additional azimuthal rotation the data were collected. Based on further computation of the data a position of the magnetic field axis with respect to the mechanical axis of the magnet was defined. The performed tests confirmed a perfect alignment of the magnet. The maximal displacement of the magnetic and mechanical axis was below 0.1 mm in the whole analyzed region, which is below the mechanical accuracy of the measurement system. The tilt of the magnetic field axis was estimated to be close to 0.14 mrad.

Preparation of the oil tank

One of the most critical regions of the gyrotron setup is the oil tank, where HV connections, cooling pipes and electric supply cables for the electron gun and NC-coil exist is very limited space. The following connections have been established before the start of the tests inside the oil tank (Fig. 1.2.3):

1) Cathode voltage
2) Filament heating
3) Cooling of the emitter cathode
4) Depression "body" voltage (using "wire" connection)
5) Cooling of the NC-coil
6) Electric supply cables for NC-coil
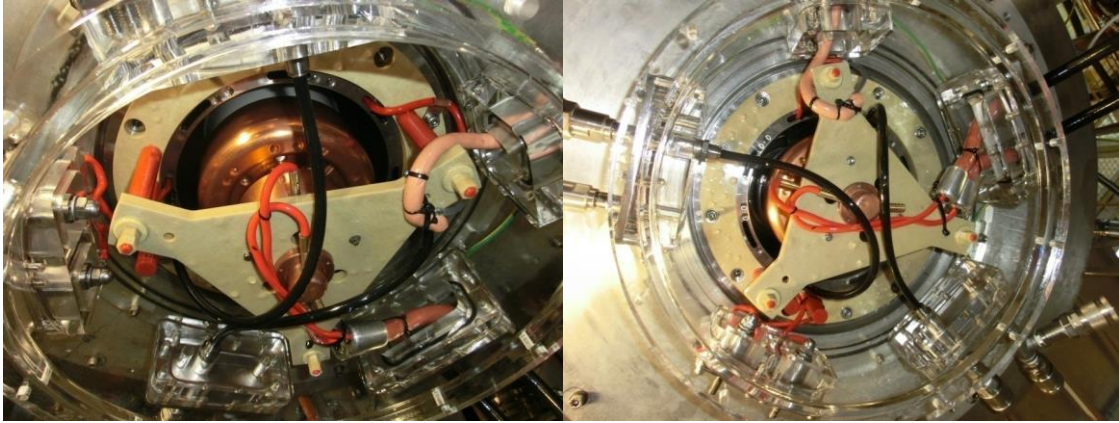
Fig. 1.2.3: Oil tank after installation of HV, electrical connections and cooling pipes.

Voltage Stand-off

The voltage stand-off properties of the gyrotron were tested with the gyrotron installed in the cryostat and with all auxiliaries prepared for CW operation. The measurements were repeated both with the magnetic field activated and deactivated. It is worthwhile to mention that before continuing to CW operation of the tube, the isolating oil that was used during the SP phase of the experimental campaign and after the stand-off measurement was replaced by fresh oil of the same type and quality in order to ensure that the isolation quality was the maximum possible.

The HV properties of the cathode to ground were measured with the gyrotron installed in the cryostat and prepared for CW operation. For such a measurement the cathode and the filament are short circuited between each other and connected to the negative pole of the high-impedance power supply, whereas the body is connected to the ground. Fig. 1.2.4 summarizes the measurements of this configuration using the typical Fowler-Nordheim curves. In detail, the red curve corresponds to measurements with the magnetic field activated and the black curve in the absence of magnetic field. In the same figure the green line presents the corresponding measurements performed by TED at Velizy during the FAT test and before the delivery of the tube at KIT. It was possible to increase the voltage up to 96 kV without any particular reaction of the tube. This value is much higher from the highest voltage that would be needed for operation of the gyrotron at the HVOP, namely 80 kV. For this reason no further attempt to increase the voltage was performed.

Similar measurements were performed with the cathode and filament short-circuited between each other and connected to ground, while the body was connected to the positive pole of a current limiting high-voltage power supply. The measurement taken are summarized in Fig. 1.2.5, the black line corresponds to the voltage stand-off properties that were measured during the FAT test, The red and green curves corresponds to measurements without and with the magnetic field activated, respectively, yet without water flow in the cooling circuit. Finally the blue and orange curves correspond to the case where water is flowing in the cooling system. In this configuration it is possible, both in the presence and the absence of the magnetic field, to increase the voltage of the body up to 32 kV without arcing incidents or changes in the quality of the vacuum.
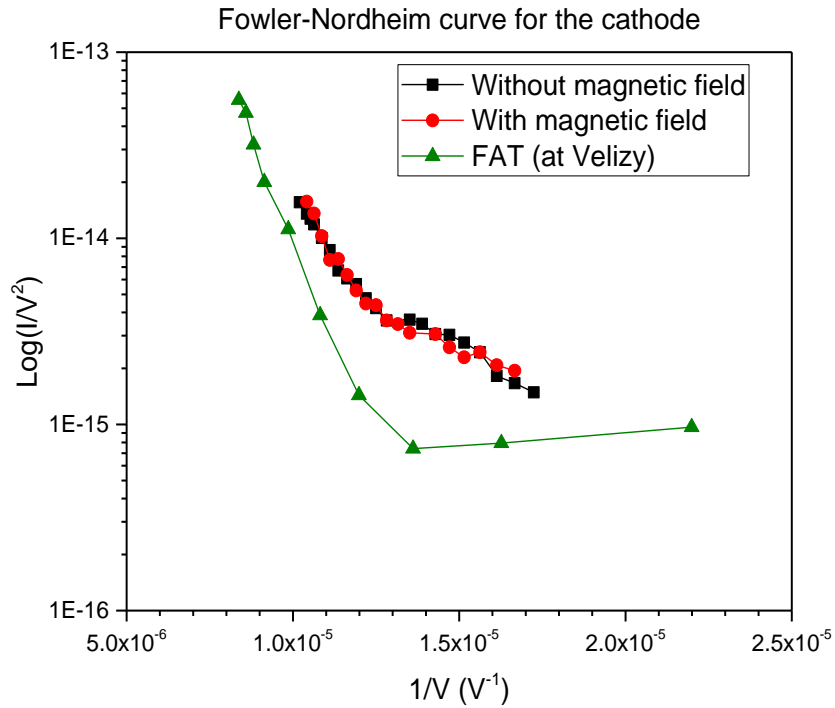
Fig. 1.2.4: Fowler-Nordheim diagram with the cathode on high voltage and the body grounded (maximum voltage applied 96 kV).
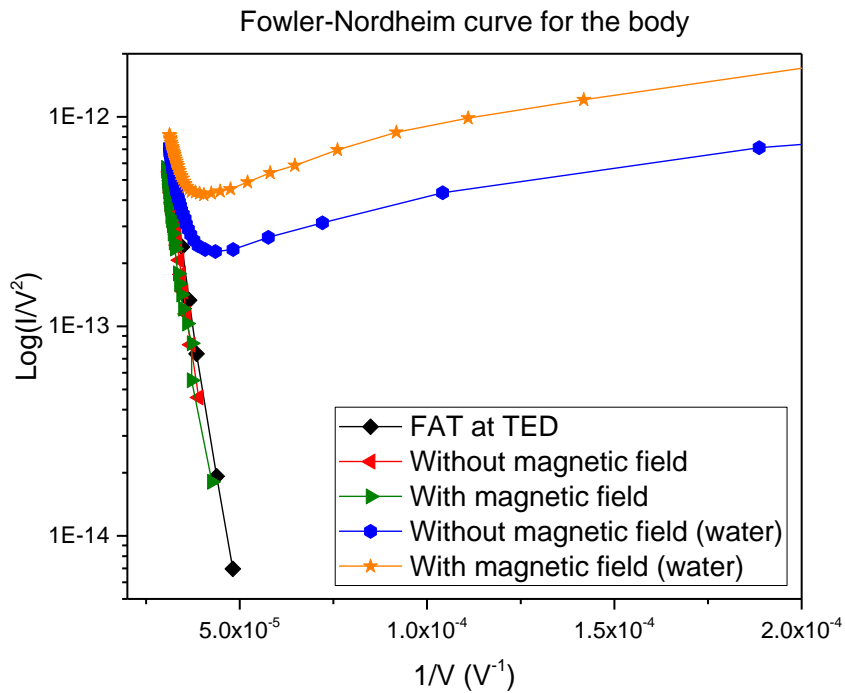
Fig. 1.2.5: Fowler-Nordheim diagram with the body on high voltage and the cathode grounded (maximum voltage applied 32 kV).

Verification of the filament heater

The test of the filament heater was performed by investigating the dependence of the voltage on the applied current. The achieved V/I-profile has been plotted and compared with similar measurements from other gyrotrons (i.e. from W7-X project), equipped with similar type of filament heater. The comparison of the measured data (SAT) are presented in Fig. 1.2.6.
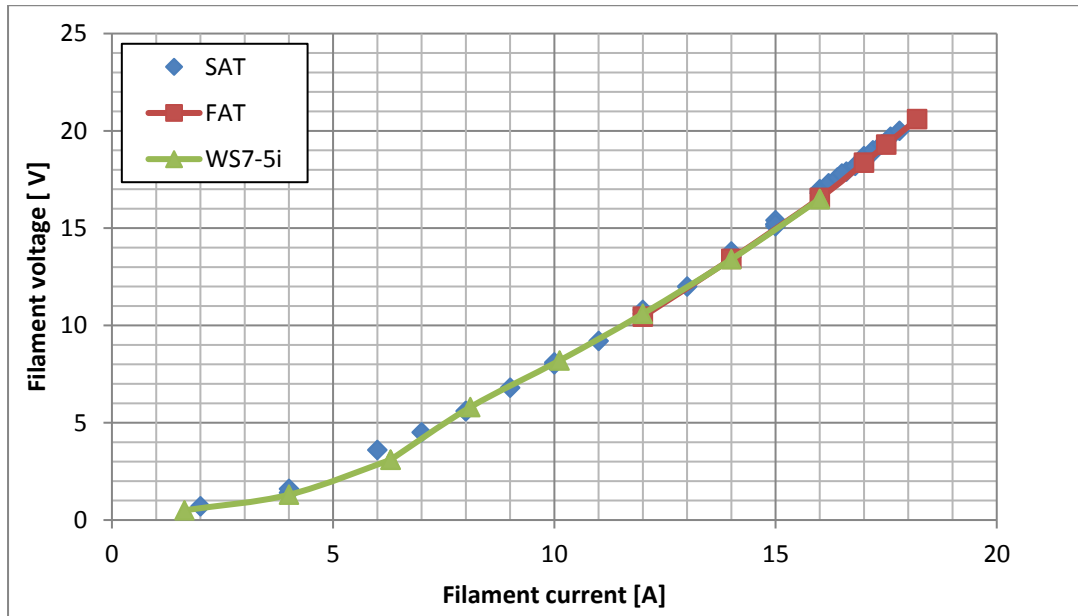
Fig. 1.2.6: Filament current vs. filament voltage (SAT) as comparison with the FAT and W7-X SN5i gyrotron results.

Electron gun emission uniformity investigation

In order to characterize the emission uniformity of the gun, the emitted current with respect to the accelerating voltage (V/I curves) was measured (Fig. 1.2.7). Based on that data, a study of the transient region between the space charge limited and temperature limited regions was performed, giving feedback about the distribution of the electron emission from the cathode. V/I curves were measured for different temperatures (filament heating current values) of the emitter ring. For each of them the standard deviation of the normalized current density distribution δJ was calculated. This factor is a measure of the emission uniformity and a small value corresponds to good uniformity in emission density. In this case it has been calculated to be around 0.24. Although it is not very small, it is an acceptable value.
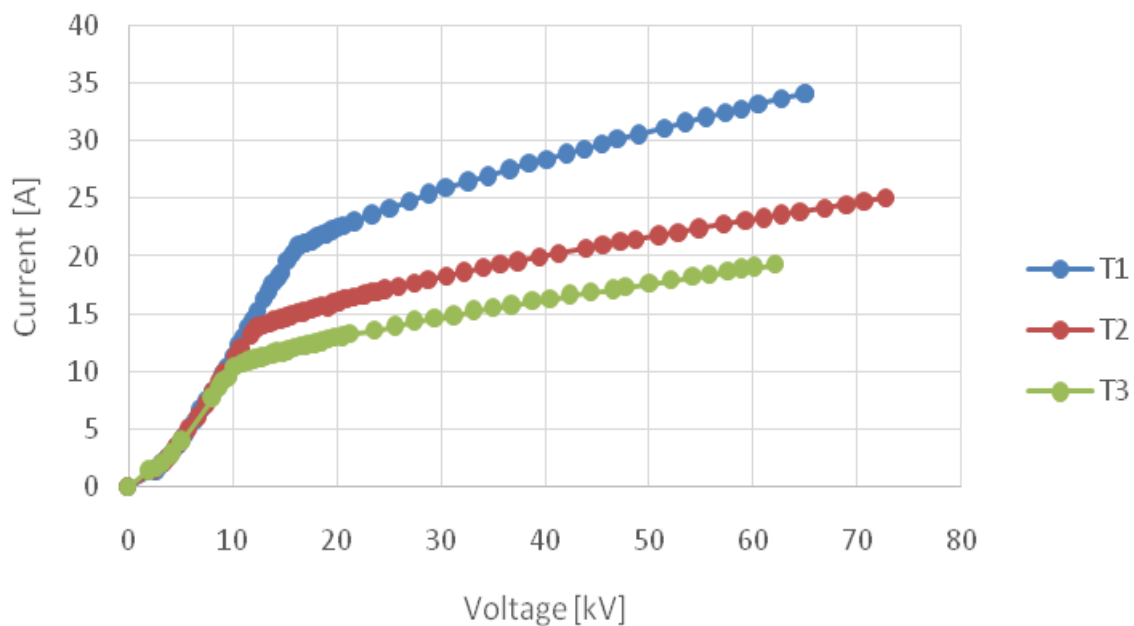
Fig. 1.2.7: Emitted current vs. accelerating voltage for three different temperatures of the emitter (T1>T2>T3).

1.2.4   Short-Pulse (SP) Operation

Experimental Setup

In order to get an overview of the performance of the tube and to compare the experimental results achieved with the SP prototype tube, the CW version was at first operated in the short pulse regime (pulse length <10 ms). The gyrotron was equipped with power diagnostic systems such as a low power flow calorimeter and a bolometer. The flow calorimeter delivered information about the actual RF output power transmitted through the window and the bolometer information regarding the internal stray radiation. In addition, the gyrotron was connected to the frequency measurement system (filter bank and frequency time analyzer (FTA), and/or PSA-system). The frequency measurement systems delivered information about the output frequency of the main mode, mode competition in the cavity and parasitic modes excitation inside the tube.
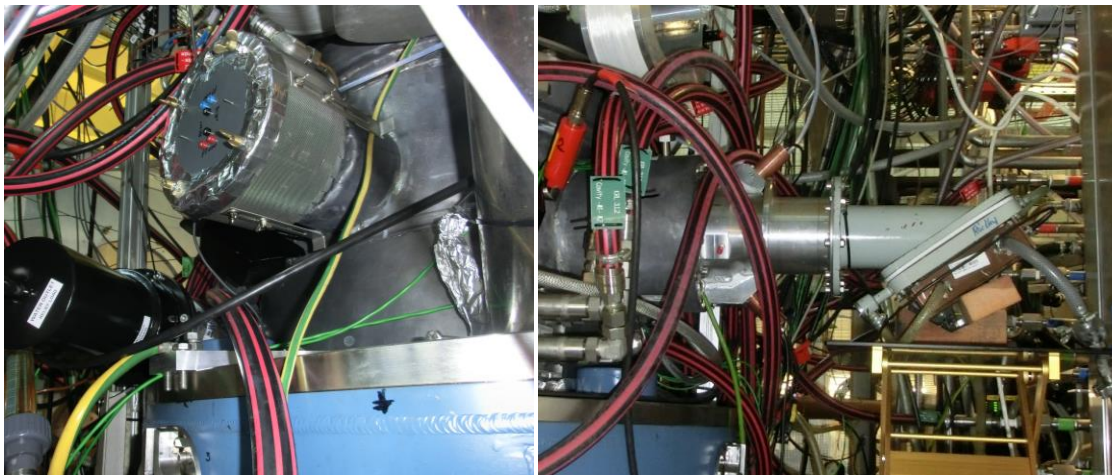
Fig. 1.2.8: Bolometer (stray radiation level monitoring) (left) and flow-calorimeter (measurement of the output power) (right).

Gyrotron Alignment

The verification of the alignment of the magnetic field with respect to the axis of the gyrotron cavity has been performed using a method developed at KIT and used with several other high-power gyrotrons. It is based on the symmetry study of the excitation region of the main mode. The idea is to introduce a radial displacement of the electron beam at the cavity by energizing a set of dipole coils and monitor the influence of this displacement on the excitation of a cavity mode. During the displacement of the electron beam using the dipole coils, a switching point between the main mode and its neighboring competitors is recorded and presented graphically. In the optimal case a circle is formed, which surrounds the dipole currents region, where the main mode is being excited. The displacement of the center of the mode excitation circle from the origin of the dipole coils coordinate system (zero current in both directions) provides an indication regarding the misalignment of the magnetic field to the gyrotron cavity axis. For the industrial prototype, the center of the mode excitation circle of the main mode $TE_{32,9}$ was estimated to be at I_X/I_Y=15 A/11 A ($I_{X,Y}$ = 1 A corresponds to a shift of 0.037 mm according simulation). In order to align properly the beam in the cavity dipole coils current +15A/+11A were used. Note, that the compensation of the electron beam position take place only in the cavity region, the position of the magnetic field at the gun region is not affected by that.

Operational Maps

Setting properly the three independent currents of the OI magnet it is possible to have the appropriate magnetic field intensity at the cavity for different combinations of the angle of the magnetic field lines on the surface of the emitter and the beam radius R_b in the cavity region. Note that the magnetic field angle in the emitter region φ_B, with respect to the gyrotron axis, is a significant operating parameter related to the average pitch factor of the electron beam. Fig. 1.2.9 represents the operational map of the gyrotron i.e. the RF power generated (Fig. 1.2.9a) and the achieved efficiency (Fig. 1.2.9b) with respect to the magnetic field angle and the beam radius in the cavity. For each operating point the maximal possible accelerating voltage has been applied before switching to the neighboring mode. The corresponding simulated values of the average pitch factor of the electron beam are presented in Fig. 1.2.9c. The measurements for the operational map have been performed after proper alignment of the electron beam in the cavity using the dipole coils of the OI superconducting magnet. Based on the operational maps, the optimal operation points in terms of power and efficiency have been defined. The most interesting operation region was discovered at φ_B = -2° and R_b = 9.55 mm. As an alternative, the operating point at φ_B = -1° and R_b = 9.45 mm can also be taken into account.

(a)

(b)
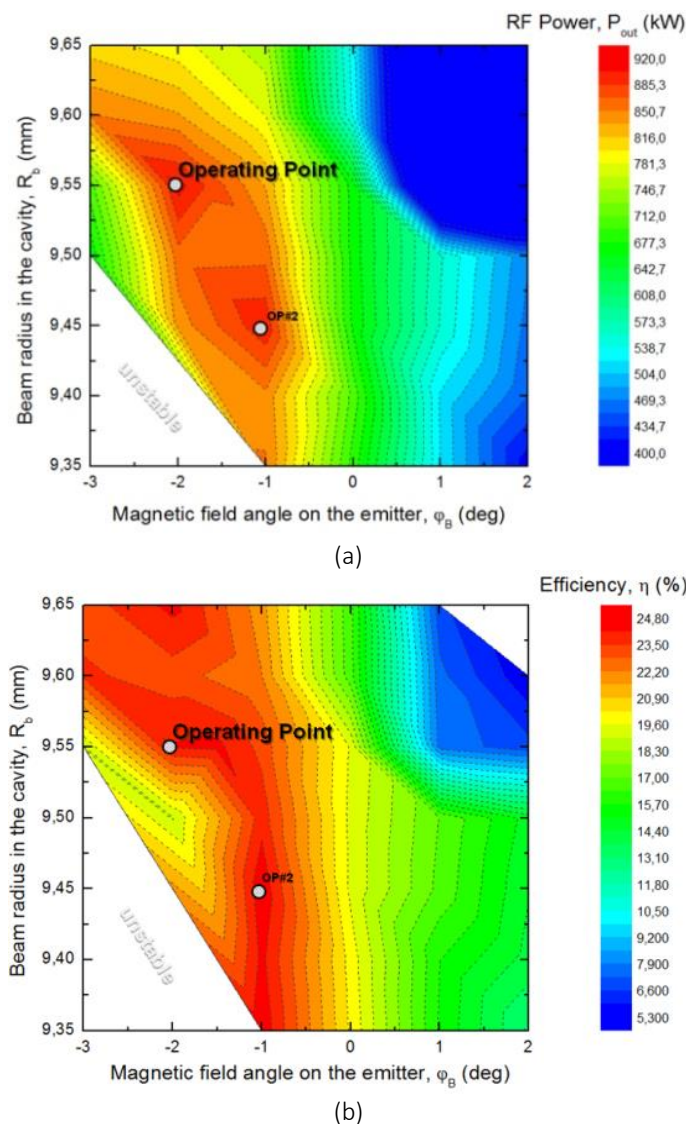
Fig. 1.2.9: (a) Generated RF power and (b) Efficiency with the magnetic field angle φ_B and the beam radius R_b in the cavity.
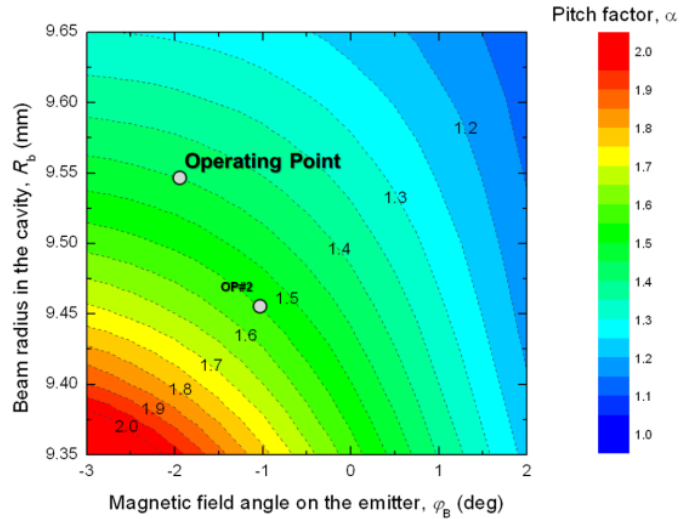
Fig. 1.2.10: Simulated Electron beam pitch factor

RF Power with respect to acceleration voltage

Due to the very stable performance of the gyrotron, the Low-Voltage Operating Point (LVOP) has been selected for the first experiments in non-depressed collector operation. Based on the above described optimal operating point the gyrotron was operated with electron beam radius R_b = 9.55 mm and magnetic field angle at the emitter φ_B = -2°, using dipole coils currents I_x = 15 A and I_y = 11 A. Operation with beam current I_b = 48 A and accelerating voltage 76.8 kV gave RF power ~930 kW with efficiency ~25 %. By increasing the electron beam current higher than the nominal parameters (I_b = 53 A and V_a = 78 kV) and after adjustment of the dipole coils (I_X/I_Y=20 A/13 A), it was possible to obtain 980 kW.

The dependency of the power and the efficiency on the accelerating voltage are presented in Fig. 1.2.11 The resulted RF power has been compared with theoretical calculations from the in-house EURIDICE code, and were found in agreement as presented in Fig. 1.2.12 The measured and theoretically expected dependency of the output frequency on the accelerating voltage is presented in Fig. 1.2.13. Taking into account the accuracy of cavity fabrication (20 µm), which corresponds to ~200 MHz frequency shift, very good agreement has been achieved between theory and experiment.
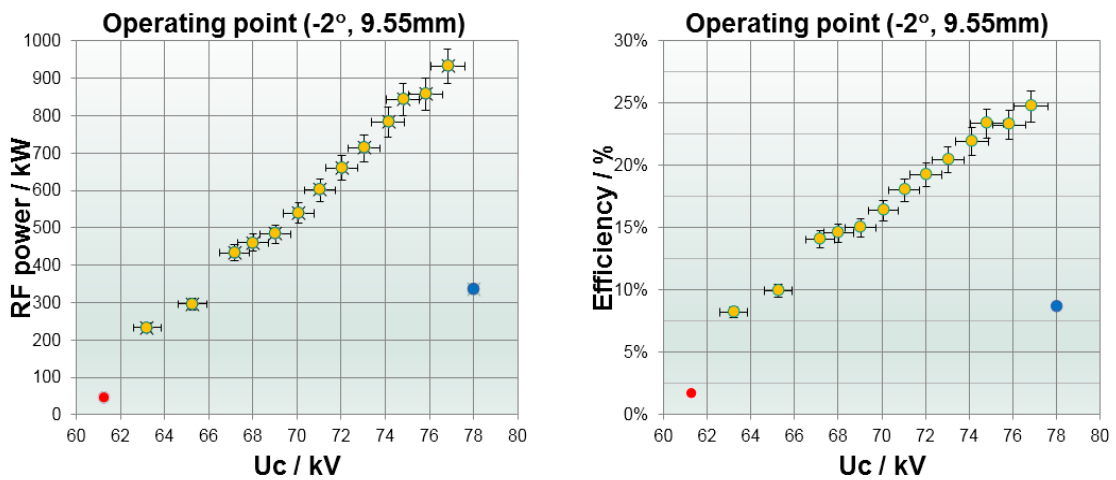
Fig. 1.2.11: RF generated power and efficiency vs. accelerating voltage achieved at LVOP with the beam current ~48 A.
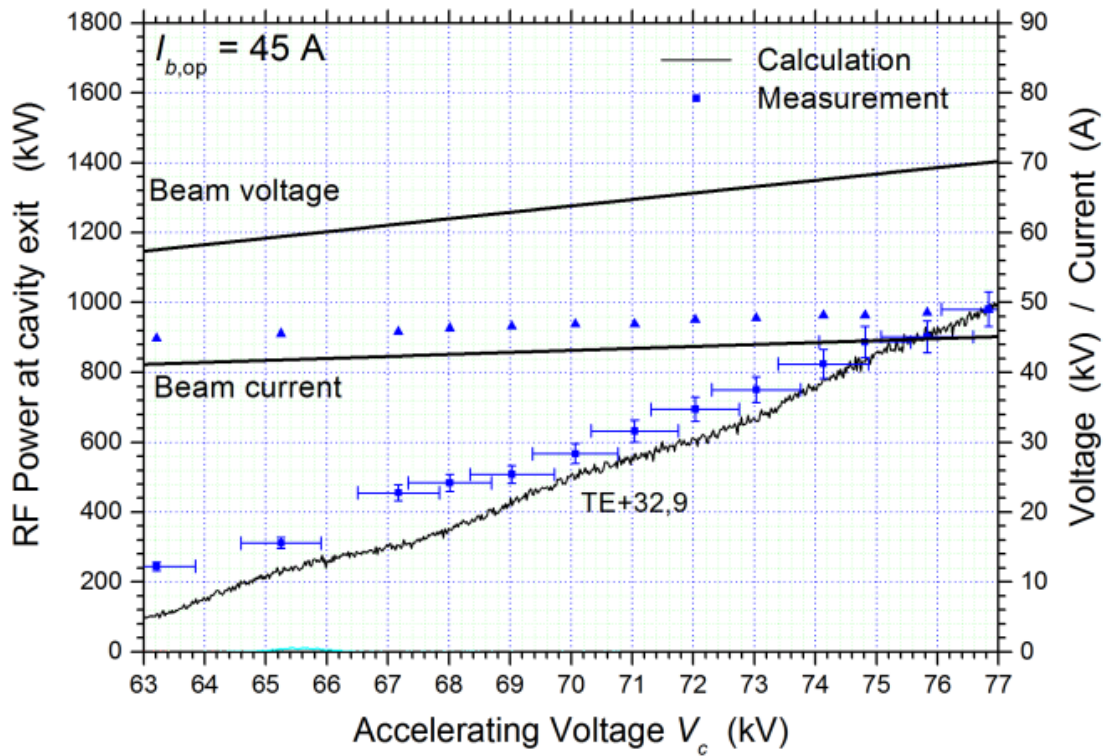
Fig. 1.2.12: Generated power vs. the beam voltage and comparison with simulated results from the code suite EURIDICE.
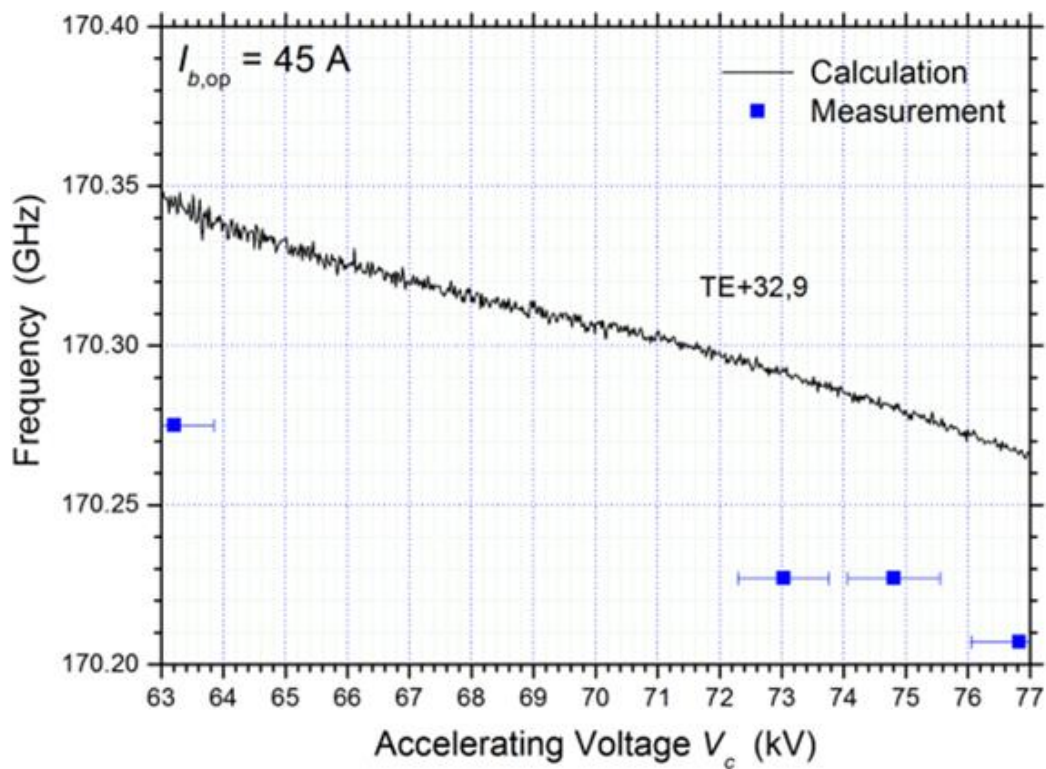
Fig. 1.2.13: Dependency of the gyrotron output frequency on accelerating voltage.

Parasitic oscillations

There are three diagnostic systems which are available for the assessment of the parasitic oscillations activity in the tube. In detail, a bolometer is installed in front of the relief window of the tube in order to assess the level of the stray radiation in the tube. In addition a waveguide is installed either on the side of the relief window or on the diamond window and transmits signal to a nine 2 GHz channel filter-bank, as well as to the more sophisticated PSA frequency measurement system. Depending on the actual value of the accelerating voltage and the beam current, it was possible in some cases to identify parasitic signals with frequencies approximately 20 GHz lower than the frequency of the operating mode. However, these signals did not seem to limit the operation of the tube.

RF Beam Profile Measurements

The first preliminary verification of the position and shape of the RF beam is usually performed using a simple thermal paper placed at the output window. The gyrotron operates in the short pulse regime (<1 ms) and delivers enough energy to create a burn spot on the thermal paper which corresponds to the real shape of the RF beam and indicates the position of the microwave at the window. Based on that procedure first verification of the efficiency of the mode converter and adjustment of its q.o subcomponents (launcher, mirrors) can be done. The information about the position of the RF beam at the output window is extremely important for the continuation of the experimental campaign and further conditioning procedure of the tube, bevor the more accurately investigation on the Gaussian mode content with the IR camera is taking place. The preliminary result of the measurement with thermo-paper are presented in the Fig. 1.2.14. They confirmed that the RF beam seems to be well aligned to the window center with the estimated shift to be approximately 5 mm to 5 o'clock position.
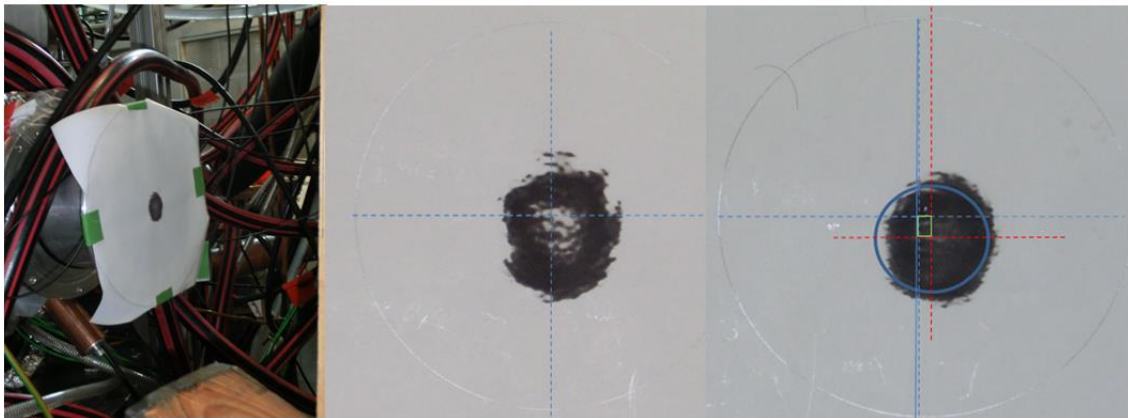
Fig. 1.2.14:   Preliminary results of the beam profile measurements at the output window achieved with thermal paper.

The thermal footprint of the gyrotron RF beam has been imaged on 200 mm diameter target plates, made either from PVC (with the thickness adjusted for 170 GHz, in order to avoid any reflections) or regular office printer paper. The targets were positioned along the RF beam path at distances between 180 and 1300 mm (in 100 mm increments) from the gyrotron output window using a motorized movement stage. It is extremely important to have several measurements inside the Rayleigh range and near to the beam waist position otherwise the phase reconstruction method will fail. The targets were perpendicular to the nominal beam axis of the gyrotron, with a 3° horizontal tilt to avoid direct reflection of the beam into the gyrotron. The IR camera was looking at the target from behind, with the camera offset horizontally from the beam axis by about 300 mm. The beam dump behind the target was a 50 mm thick PVC plate angled horizontally to be fully absorbing and to avoid any reflection. The arrangement of the measurements setup is presented in Fig. 1.2.15. Pulse lengths between 0.3 ms and 3 ms were used in order to achieve an optimal

temperature and measurement dynamic depending on the size of the RF beam spot on the target (Fig. 1.2.15) and its distance from the output window. According to the post processing of the measurements, the Gaussian content of the beam is found to be 97 %. The most important beam parameters are summarized in Table 1.2.1.
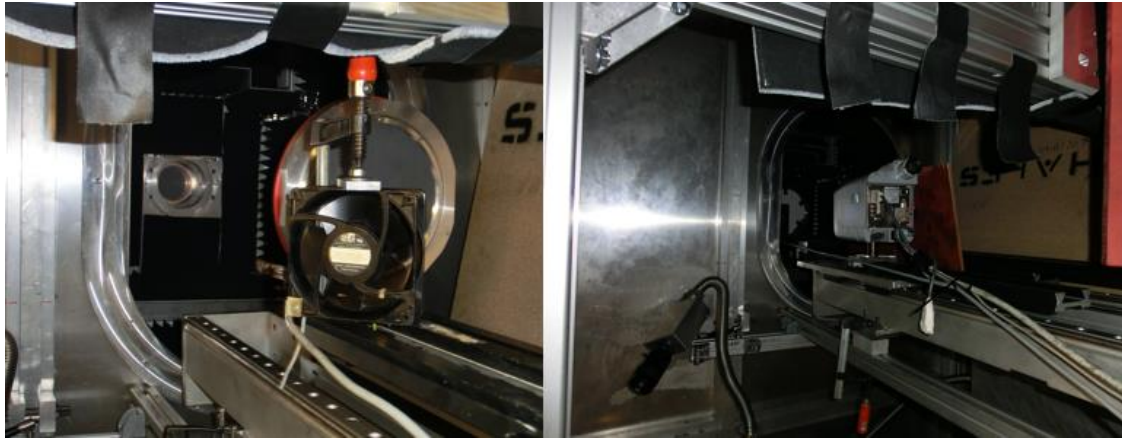
Fig. 1.2.15:   Arrangement of the IR beam profile measurement setup.
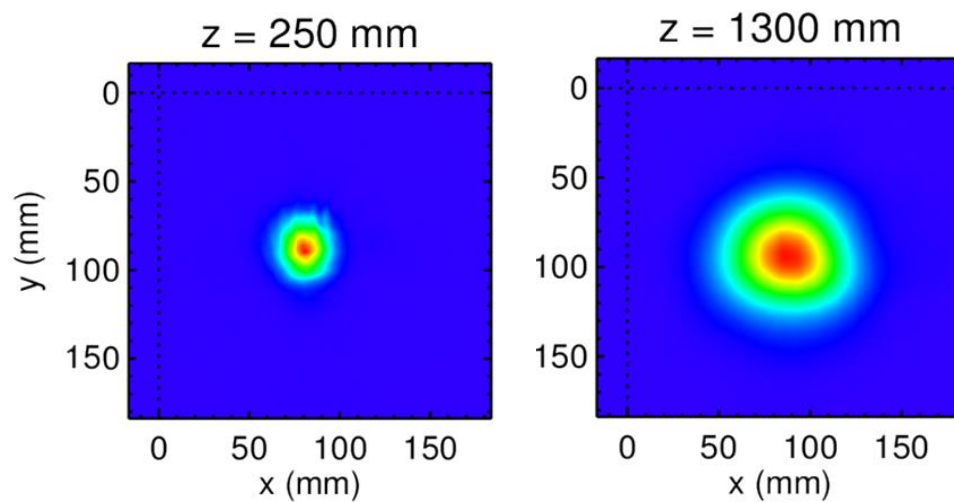
Fig. 1.2.16.   Thermographic images from the microwave output beam of the gyrotron recorded on a PVC-target at different distances z from the gyrotron window.

Table 1.2.1: RF beam properties

Parameter	X direction	Y direction
Gaussian content	0.97	
Beam waist (mm)	18.3	21.5
Waist position (mm)	28	28
Beam tilt (mm/m)	7.8	6.0
Beam shift at the window plane (mm)	-4.9	2.7

1.2.5   Long Pulse (CW) Operation

Microwave Box and Diagnostics

Fig. 1.2.17 depicts the main quasi-optical components and diagnostics installed inside the microwave box of the KIT test-stand. The RF beam that exits the diamond window of the gyrotron is driven to the load entrance by subsequent reflections on four mirrors. The position of the mirrors is carefully adjusted by recording the footprint of the beam on thermal paper in order to have the beam well aligned around their center. Fig. 1.2.18 presents the footprint of the RF beam on thermal paper placed at the back side of the microwave load, at the position where a conical mirror is placed in order to scatter and distribute the microwave power along the surface of the load by subsequent reflections on the load wall.

Special care is given also on the angle of mirror 1 with respect to the RF beam line, since this control the coupling factor of the waveguide coupler that is realized on the surface of the mirror 1 and in turn the amplitude of the signal that is guided by a short waveguide to a RF diode that is used to detect mode loss and deactivate the gyrotron to avoid possibility of damage due to excitation of a wrong mode (mode loss interlock). An additional signal taken from the relief window is also transmitted with a waveguide to the frequency measurement related systems, namely the filter-bank, frequency measurement and the PSA system. The signal from the relief window is preferred for such measurements, since the extraction efficiency of parasitic signals is low from the diamond window, especially in a distance similar to the one between the diamond window and mirror 1.
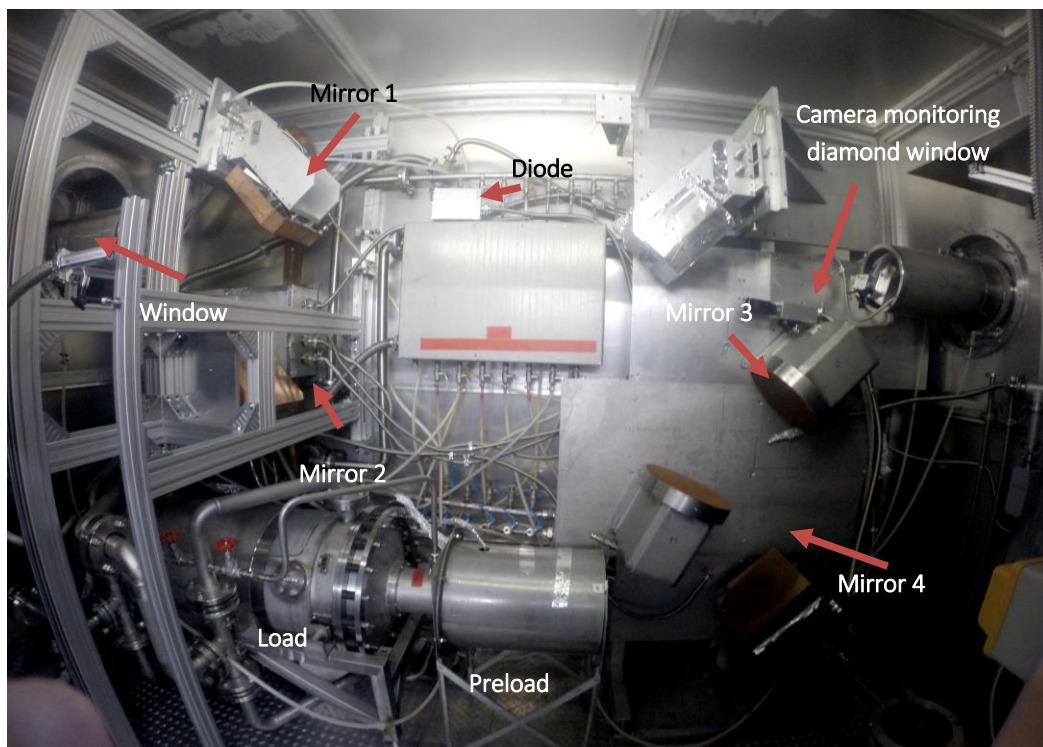
Fig. 1.2.17:   Microwave box prepared for CW operation of the gyrotron.

Fig. 1.2.18: Thermal paper shot at the back side of the microwave load (at the position where the conical mirror is mounted).
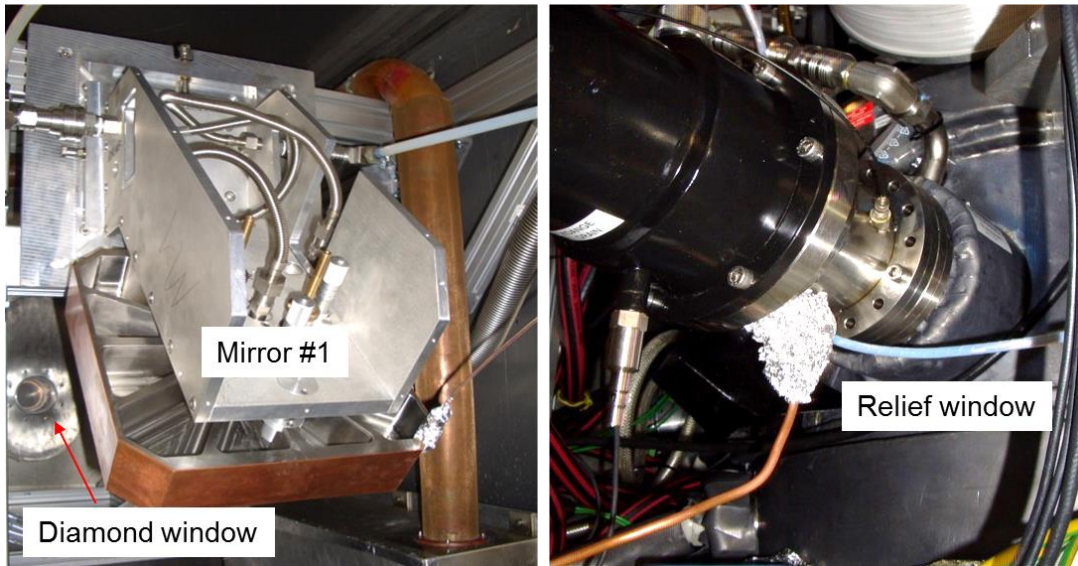
Fig. 1.2.19: Diagnostics installed inside the microwave box and at the relief window.

Performance in CW

After the conditioning of the collector the operational parameters were progressively increased to excite RF oscillations with the goal to elongate the pulse duration from the millisecond regime to the three minutes regime. Fig. 1.2.20 represents the length of some representative pulses (in terms of length and output power) that were achieved during several days of the CW experimental campaign with respect to the date. The RF conditioning started a few weeks earlier (approximately on 15/9/2016), increasing the necessary time to proceed from short pulse to long pulse regime to approximately seven weeks.

14
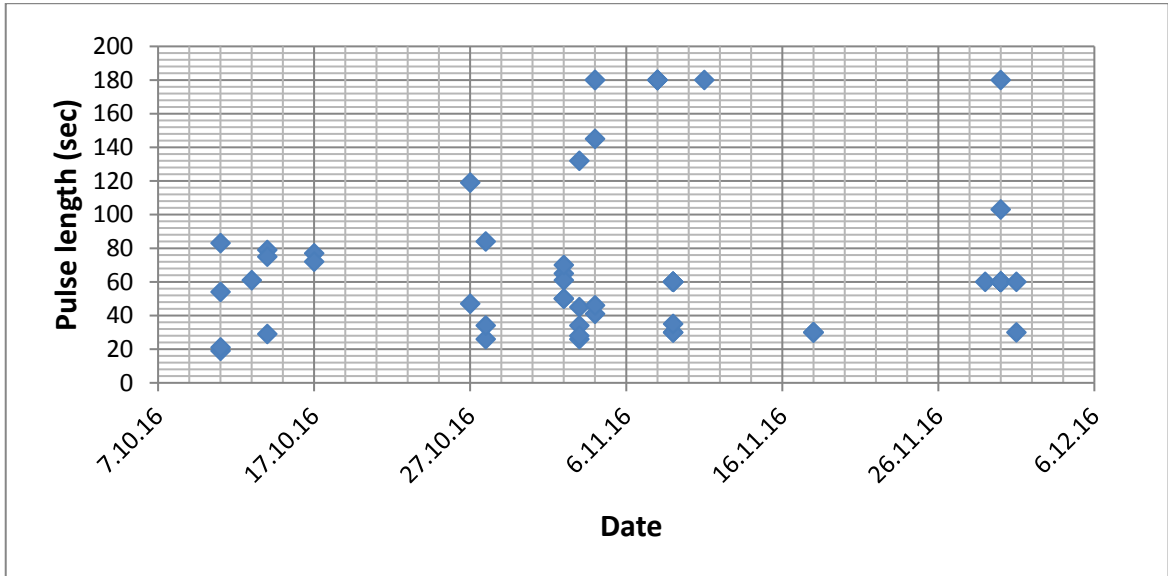
Fig. 1.2.20: Evolution of the pulse length achieved during the conditioning of the tube with RF.

Fig. 1.2.21 presents the operational parameters of a three minutes pulse that was achieved with the industrial prototype. During this pulse the average generated power was 786 kW with accelerating voltage 72.2 kV (including 24.6 kV of depression voltage) and beam current 44.4 A, getting in this way an overall efficiency of 37.2 %. During the pulse the vacuum level was less than 1 μA, whereas a few visible peaks are a result of conditioning events. Considering that at the moment the tube is sufficiently conditioned with RF a vacuum level in the range 0.6-0.8 V (Midivac power supply) should be expected, which corresponds to less than 1 μA.

Fig. 1.2.22 presents the temperature of all the collector thermocouples with respect to the time during the same pulse. The maximum temperature of the collector at the end of the pulse reaches almost 190 °C mainly due to the low depression voltage that is used.

Fig. 1.2.23 presents the typical light distribution that is observed on the surface of the diamond window during the operation of the tube with long pulses.

Fig. 1.2.21: 180 sec pulse achieved during the experiments. In the figure it is visible the beam current (blue), the accelerating voltage (black), the cathode voltage (green), the depression voltage (red), the vacuum reaction (yellow) and the mode-loss diode signal (magenta).

Fig. 1.2.22: Collector's thermocouple temperature and I$_{beam}$ during a 180 sec pulse.
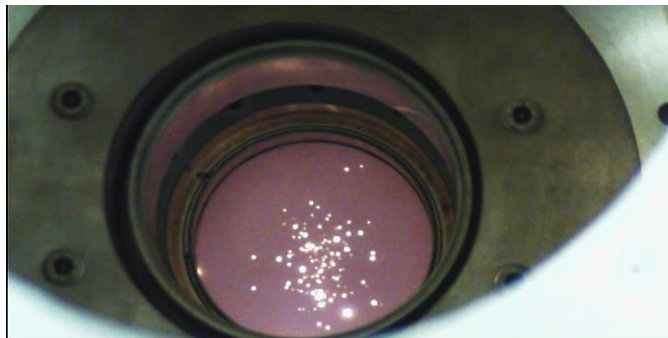
Fig. 1.2.23: Stars constellation" on the diamond window during CW operation

Calorimetry system

The generated power and the dissipated losses on the internal component of the gyrotron as well as of the auxiliaries in the microwave box are monitored using a calorimetry system. Fig. 1.2.24 presents the power measurements that were recorded for a ~800 kW - 180 s pulse. All measured values expressed as a percentage of the input and the generated power are summarized in Table 1.2.2 It is interesting to note that in most cases the calorimetrically measured power approaches 99 % of the electrical input beam power. In addition the internal losses (internal components of the tube) are in the level of 5 % with respect to the RF power at the diamond window, whereas the external losses (inside the microwave box) are in the range of 2-3 %.
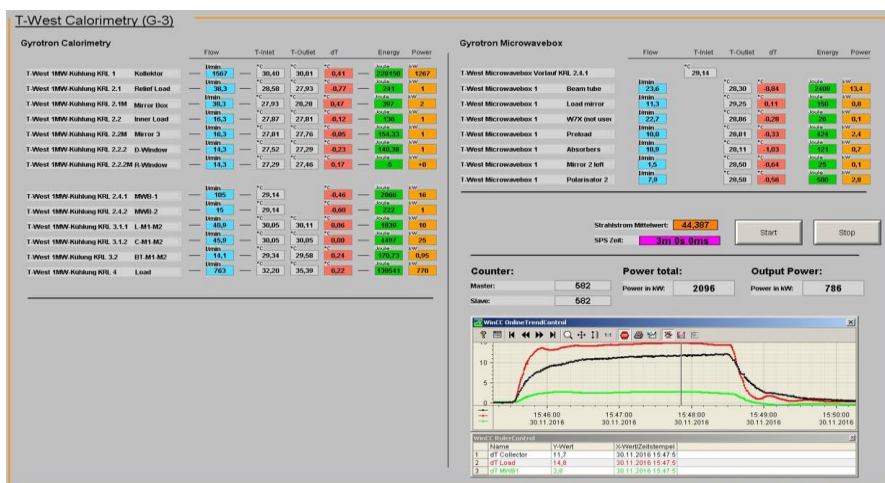
Fig. 1.2.24: Calorimetry measurements during a 180sec pulse.

Table 1.2.2: Power balance for a 180 sec pulse.

ITER CW, 30.11.2016			Power [kW]	Power [%] w.r.t. total generated	Power [%] w.r.t. output power	Power [%] w.r.t. input power
	Ucath (kV)	Ib (A)				
Input power	47.6	44.4	2133.44			
Measurements						
Window			1	0.1	0.1	0.0
Mirror 3			1	0.1	0.1	0.0
Cavity M1-M2			25	3.0	3.2	1.2
Beam tunnel M1-M2			0.95	2.3	0.1	0.0
Mirror Box			2	0.2	0.3	0.1
Launcher M1-M2			10	1.2	1.3	0.5
Kollektor			1267	153.0	161.0	59.9
Inner Load			1	0.1	0.1	0.0
Relief Load			1	0.1	0.1	0.0
Relief Window			0	0.0	0.0	0.0
Water Load			770	93.0	97.8	36.4
Messbox 1			16	1.9	2.0	0.8
Messbox 2			1	0.1	0.1	0.0
Output power			787			99.2
Total generated power			828			
Internal RF losses			41	5.2	5.0	1.9
External RF losses			17	2.2	2.1	

Power and Efficiency

Fig. 1.2.25 presents with colored squared the achieved RF power in long pulse operation with respect to the beam radius at the cavity and with the orientation of the magnetic field lines in the emitter region as a parameter. In the same figure the colored circles represent the corresponding overall efficiency in depressed operation. Although the experimental measurements are quite sparse, there is a visible tendency for increased power and efficiency towards lower beam radii at the cavity and more negative

angles of the magnetic field in the emitter region. The maximum achieved power in 180 s pulses is 786 kW with 37.2 % total efficiency. In detail the cathode voltage was 47.6 kV, the body voltage 24.6 kV and the average beam current 44.4 A.

It is important to mention that the reported power values were obtained for the different operating points using different values of the accelerating voltage and of the beam current. In addition, at each operating point the accelerating voltage is, usually, slightly lower than the maximum possible one, in order to minimize the risk of a mode jump during the cooling phase of the cathode, where the beam current decreases ~2 A, depending also on the current boosting scheme that is employed. In addition, the dipole coil currents that are used to better align the electron beam in the cavity, where not further optimized during the long pulse operation of the tube. The values used during power optimization in short pulse were applied. Summarizing, it would be quite possible to further optimize the tube in CW operation in order both to produce slightly more power, as well as to increase the total efficiency of the gyrotron.

Fig. 1.2.26 presents the generated power and the corresponding achieved total efficiency with respect to the depression voltage for the operating point (-3°/9.50 mm). The generated power is almost constant with the increase of the depression voltage, which results in an increase of the total efficiency. Depression voltage values higher than 26 kV resulted in body current in the range of 50 mA and instabilities during the first seconds of the pulses, including arcing and current fluctuations.
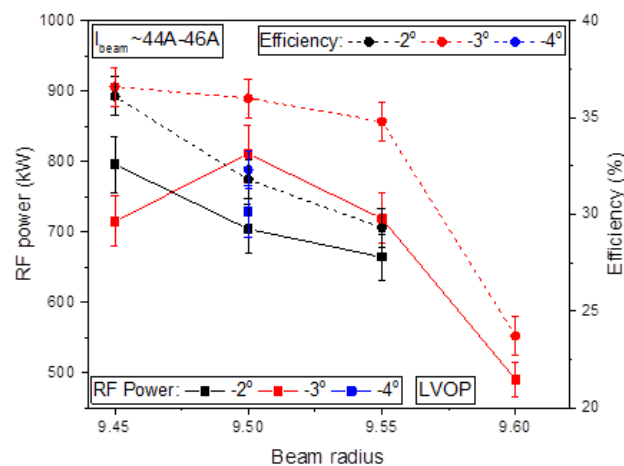
Fig. 1.2.25:   RF Power and corresponding overall efficiency with respect to the beam radius and with the orientation of the magnetic field lines at the emitter as a parameter. Operation only at the LVOP.
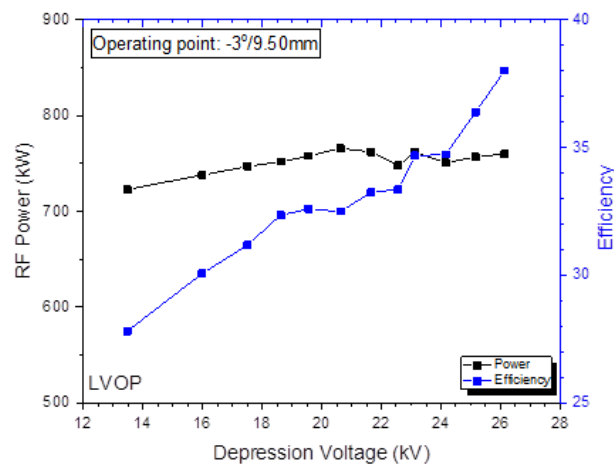
Fig. 1.2.26:   RF power and corresponding overall efficiency with respect to the depression voltage for the LVOP.

Frequency dependence

The time dependence of the frequency for the nominal mode TE$_{32,9}$ was recorded using the PSA (Pulsed Spectrum Analysis) measurement system that is available at KIT. Since the maximum acquisition length with full sampling resolution is limited to 14 ms, it is not possible to record continuously a single pulse in CW operation of the gyrotron. For this reason, multiple pulses with similar accelerating voltage and beam current properties were made and by controlling the delay time between the trigger signal of the pulse and the PSA system activation, 1 ms measurements were recorded at different points of time of the respective pulse. Taking into account that the relative spread of the accelerating voltage as well as of the beam current of these pulses are both below 0.1 % we consider this approach to give an adequately accurate image of the frequency drop during the first seconds of a single pulse.

Fig. 1.2.27 presents the frequency of the nominal operating mode of the tube with respect to the time for two different cases of the orientation of the magnetic field line in the area of the emitter, namely -2° (red circles) and -3° (black squares). In both cases the oscillation frequency starts approximately from 170.3 GHz and drops progressively towards 169.95 GHz (frequency drop in the range of 350 MHz) meeting very well the ITER specifications.
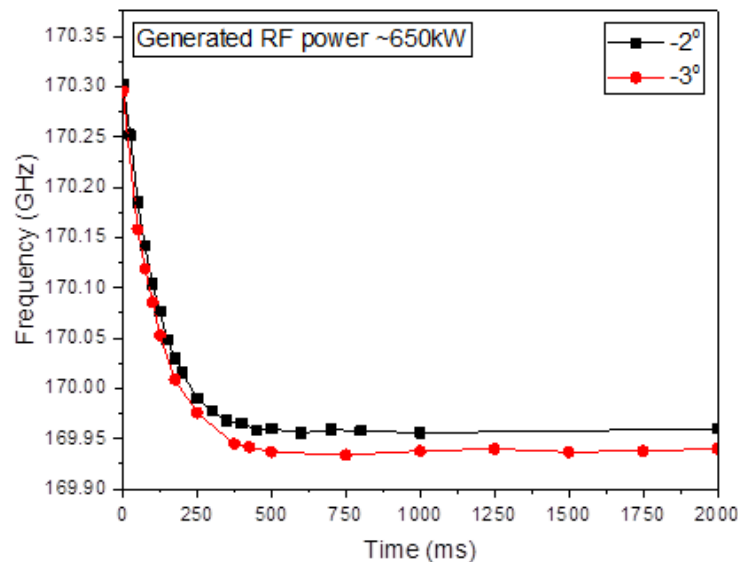
Fig. 1.2.27:   Frequency drop with respect to the time.

The above described frequency drop during the pulse is, in general, attributed to the neutralization of the beam during the pulse as well as to the thermal expansion of the cavity, which strongly depends on the generated RF power. In both presented operating points the generated RF power was in the level of ~650 kW. The dependence of the frequency drop on the generated power is presented in Fig. 1.2.28, using experimental data from different operating points and making the assumption that the frequency drop is governed by the total generated power and not on the specific operating parameters of the different operating points. Although the data in the 700-800 kW power level are quite scattered, there is approximately 400 MHz frequency drop for 0.8 MW of generated power.
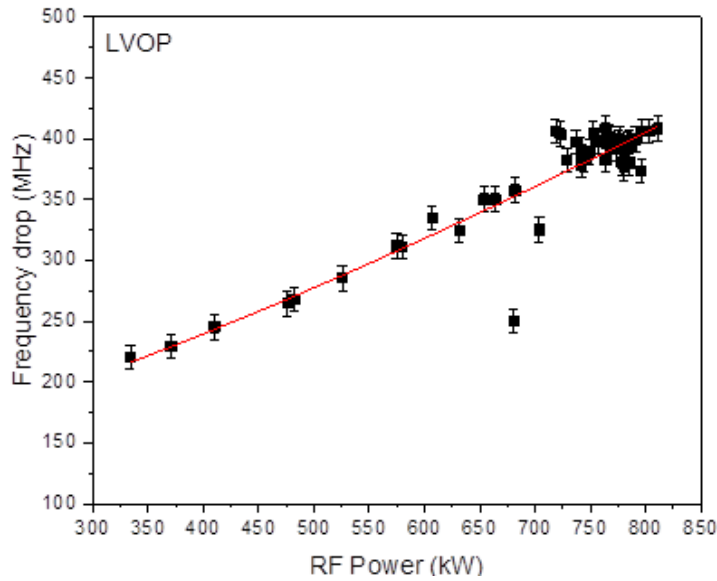
Fig. 1.2 28: Frequency drop with respect to the generated RF power.

Parasitic oscillations during CW operation

For most of the operating points in CW operation of the tube there was minor activity in the filter-bank channels. In detail at the most conditioned operating point of -2° there is no other signal than the one of the nominal mode, except if we decrease the beam radius to values as low as 9.45 mm. For this operating point (-2°, 9.45 mm) there is a visible signal in the filter-bank channel that covers the frequency range 159 GHz to 161 GHz, which, however, decays and vanishes after approximately 500 ms (Fig. 1.2.29). This signal is more persistent and remains visible for the complete duration of longer pulses when changing the gyrotron operating point to (-3°, 9.50 mm).
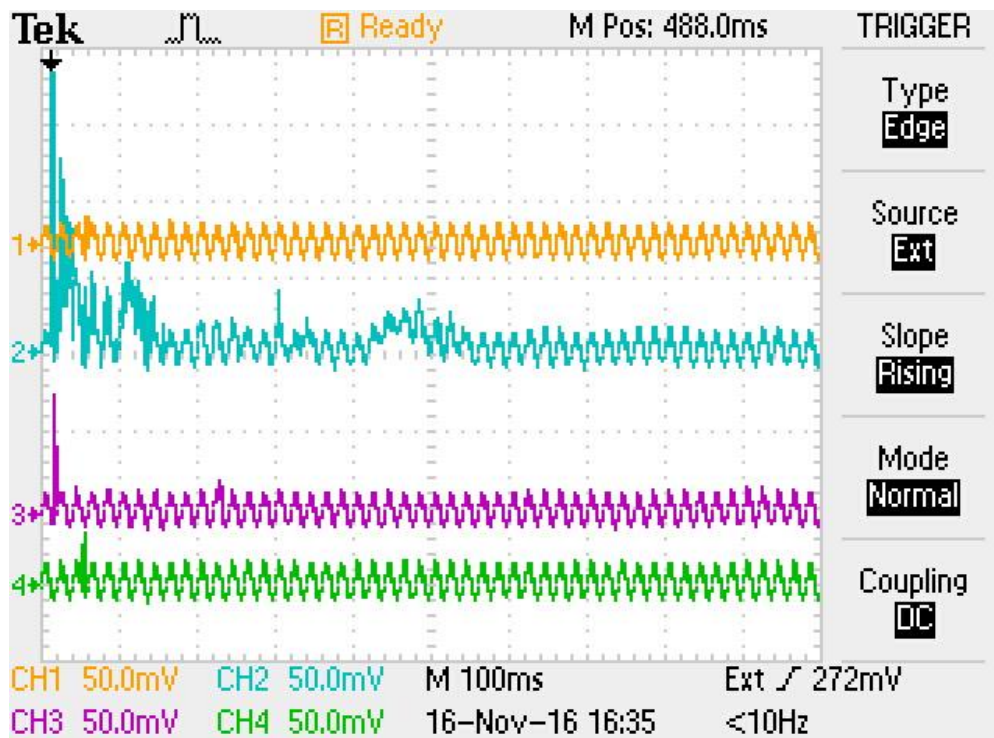
Fig. 1.2.29: Decay of the parasitic signal (blue) in the filter-bank after 300 msec.

Energy consumption

The scientific assessment of the experiment is based on pulses with total duration of approximately one hour. At the time of writing this report this sum includes eight 180 s pulses that where performed in series in order to verify that the three minute limit has been successfully and reproducibly achieved. The distribution of the duration of the pulses that are used in the scientific assessment of the CW operation of the industrial prototype gyrotron is presented in Fig. 1.2.30. In this histogram there are two primary peaks at 30 s and at 60 s. The reason that these two pulse duration were selected was to minimize the waiting time between pulses in order to speed up the search procedure for the optimal operating parameters. Of course much more pulses were performed, the total pulse duration in CW operation is approximately four hours. The filament heating was activated for approximately 417 hours.
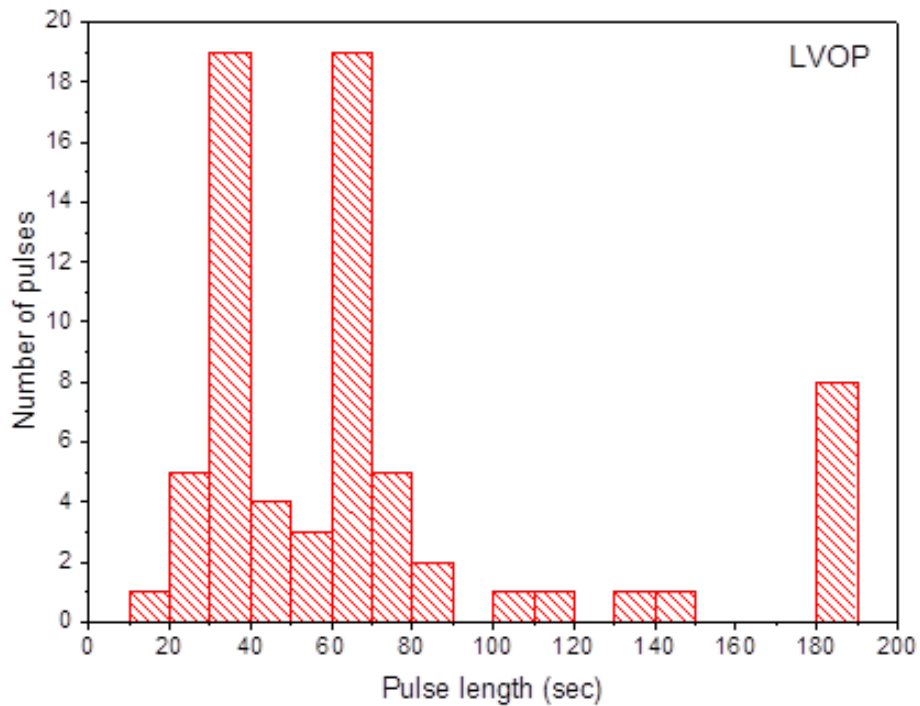
Fig. 1.2.30: Histogram of the duration of the pulses used for the scientific assessment.

High Voltage operating point

Due to maximizing the effort for optimizing the performance of the gyrotron for the LVOP, limited time was spent in CW operation of the tube at the High Voltage Operating Point (HVOP). Similarly to the LVOP and in order to minimize the waiting time between consequent shots, mostly pulses with duration 30 s and 60 s were performed, as it is visible in Fig. 1.2.31 where a statistical analysis of the pulse duration is presented.

At the HVOP the gyrotron was mainly operated with the magnetic field angles at the emitter region -2° and -3° and beam radii 9.50 mm and 9.55 mm. Fig. 1.2.32 summarizes the achieved output power and the corresponding efficiency for the attempted operating points. It is evident that in most cases approximately 800 kW were generated with the corresponding efficiency around 35 %. Although the operational time for the HVOP was significantly lower than for LVOP it can be concluded that the performance and limitations of the tube was very similar.

Fig. 1.2.33 presents the frequency drop with respect to the generated RF power as it was recorded in the HVOP. The situation is not much different from the LVOP resulting to approximately 400 MHz frequency drop for power in the range of 800 kW.
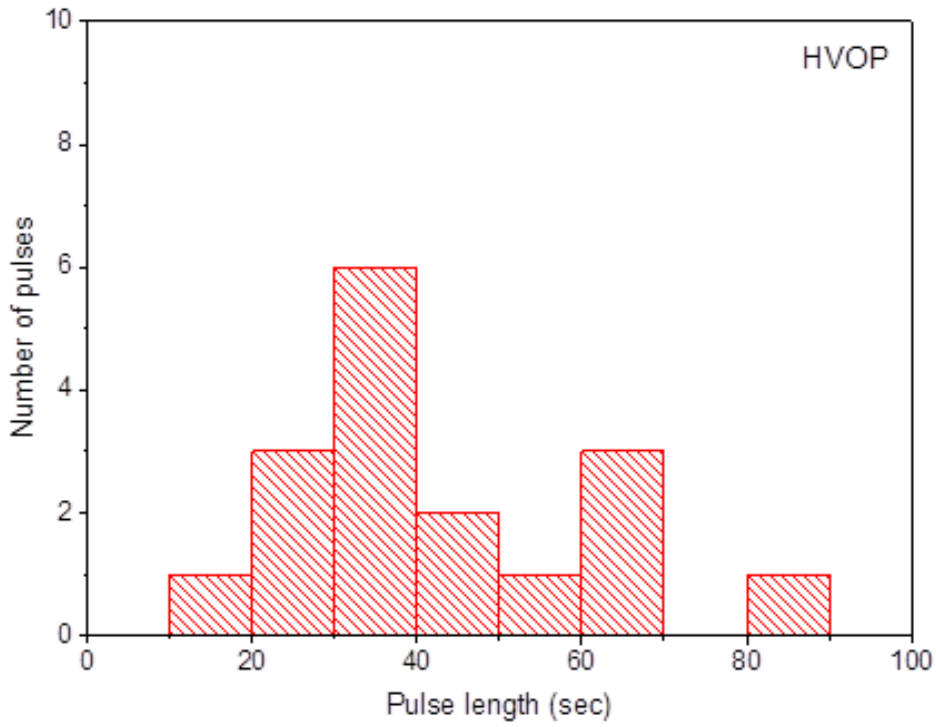
Fig. 1.2.31: Histogram of the duration of the pulses used for the scientific assessment.
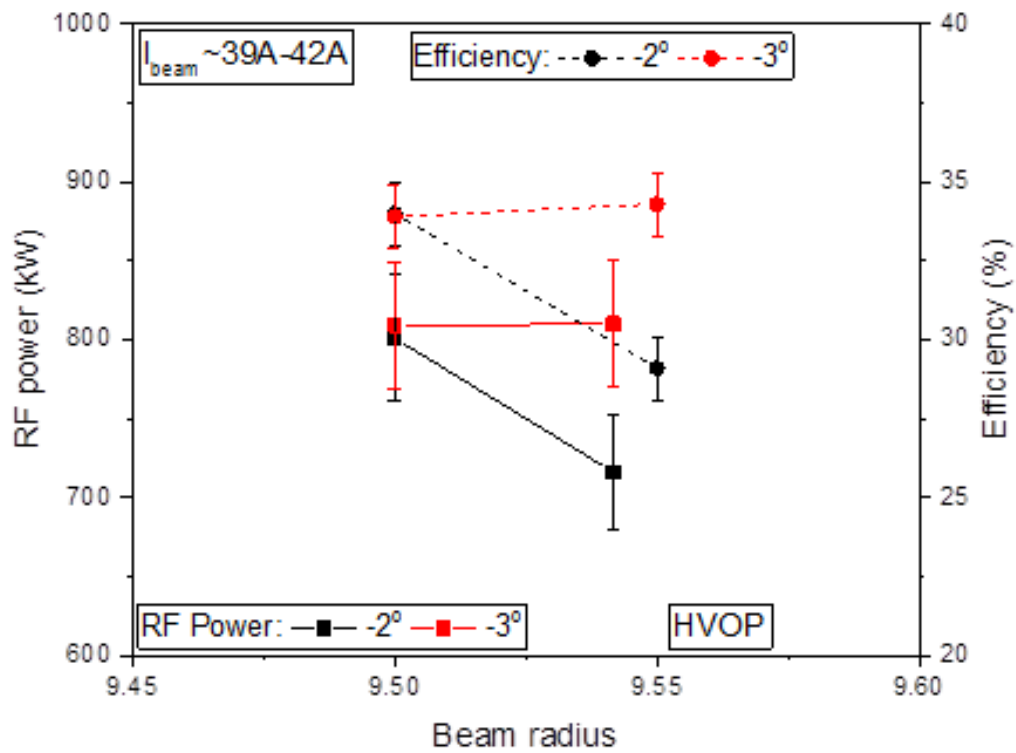
Fig. 1.2.32: RF power and corresponding efficiency at different operating parameters at the HVOP.
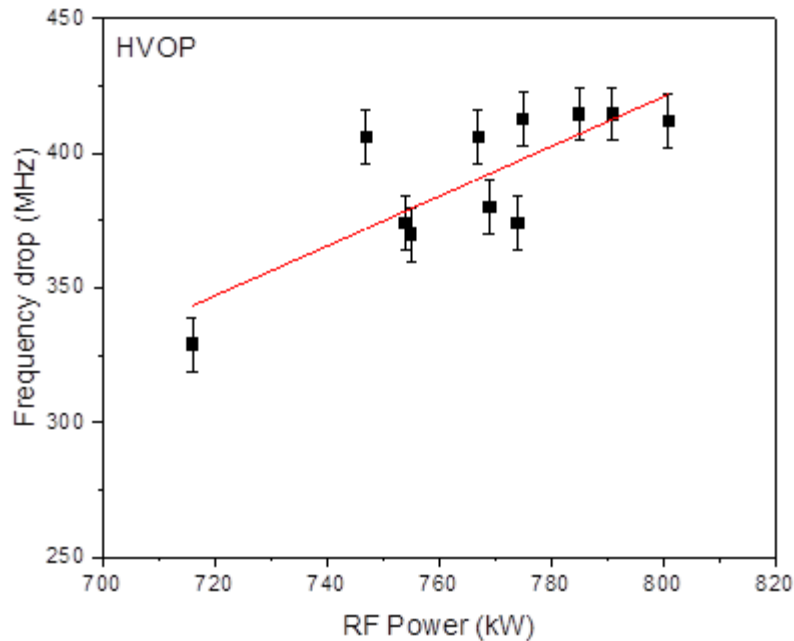
Fig. 1.2.33: Frequency drop with respect to the generated RF power at the HVOP.

1.2.6 Summary

The 1 MW, 170 GHz CW industrial prototype gyrotron, which has been developed by the European GYrotron Consortium in cooperation with the industrial partner Thales Electron Devices (TED) and under the coordination of the European domestic agency F4E, has been delivered at KIT on January 18, 2016. Since then, the gyrotron has been thoroughly tested, at different operating points in terms of accelerating voltage, beam current and magnetic field profile, both in the SP and LP regime with pulses up to 180 s.

Operation of the CW gyrotron with millisecond pulses resulted in stable excitation of the nominal mode at 170.22 GHz for a wide range of operating parameters and with a level of stray radiation comparable with the SP version of the tube. The Gaussian mode content of the RF beam was found to be at least 97 %.

In the SP regime and after optimization of the alignment of the gyrotron as well as of the operating parameters, it was possible to generate RF power in the 1 MW level. In detail with near nominal parameters, the highest obtained power was 930 kW with efficiency approximately 25 %. By increasing the electron beam current higher than the nominal parameters, namely I_b = 53 A with accelerating voltage V_a = 78 kV, power as high as 980 kW was achieved with slightly lower efficiency.

After proper conditioning of the tube with and without RF (which lasted approximately seven weeks), the experiments were continued in the LP regime with 180 s long pulses, which is the maximum possible with the available HV power supply at the KIT test facility. The maximum achieved power in 180 s pulses with nominal operating parameters is 786 kW with 37.2 % total efficiency, in depressed-collector operation. In detail the cathode voltage was 47.6 kV, the body voltage 24.6 kV and the average beam current 44.4 A. There were multiple cases were the generated power was slightly higher than 800kW, yet with pulses of 60s. It should be noted that the pulse duration was reduced in order to reduce proportionally the waiting time between pulses, which for the case of 180 s pulses is half an hour.

The experiments with the industrial prototype will be continued at EPFL Lausanne during 2017, whereas additional experiments with the SP tube with be performed in parallel at KIT it order to better understand the performance of the CW gyrotron and identify ways to further optimize the generated power.

1.3   Numerical Simulations

1.3.1   Design approaches for new multi-stage depressed collectors

A design approach for the collection of a sheet electron beam is proposed (shown in Fig. 1.3.1). Based on several considerations, analytical equations have been extracted for the design optimization and the estimation of the collection efficiency. This type of collector is appropriate for devices which operate with a sheet beam confined by a strong magnetic field, such as a free-electron laser (FEL) or a sheet-beam gyrotron. In order to apply the proposed design approach to conventional gyrotrons, the transformation of the cylindrical hollow beam to one or more sheet beams is proposed using appropriate magneto-static fields. A conceptual design for a gyrotron MDC system based on that idea is proposed. In order to illustrate this idea, two preliminary slightly optimized designs were simulated with efficiencies 80 % and 86 %.
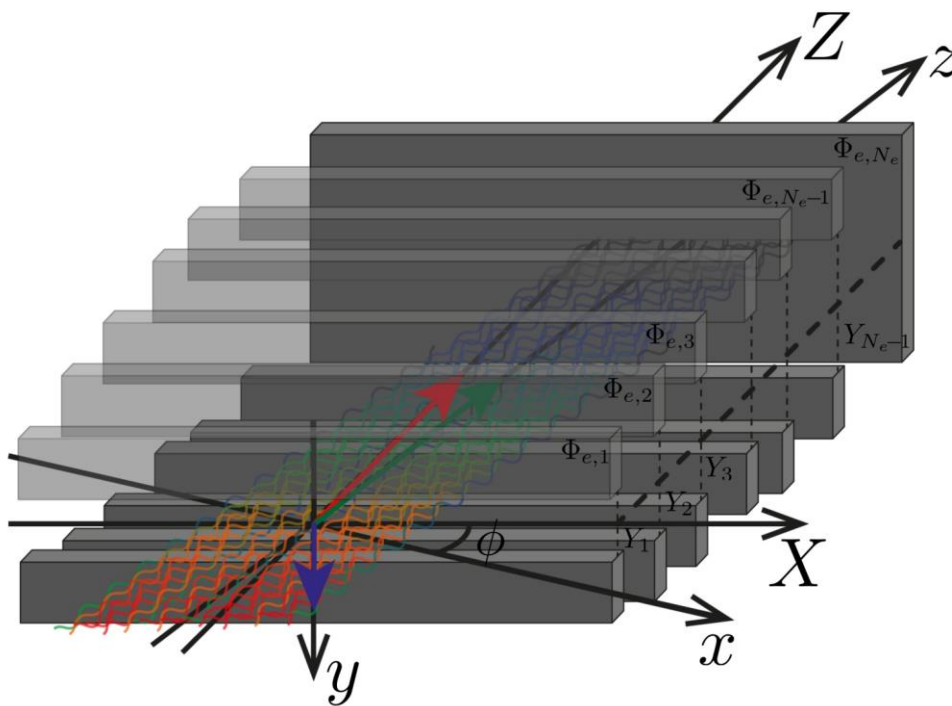
Fig. 1.3.1: Conceptual drawing of the proposed multistage depressed collector for sheet electron beam.

1.3.2   Influence of trapped electrons on the gyrotron performance

The presence of trapped electrons in the MIG region can cause many problems to the gyrotron operation such as decreased efficiency, failure of the excitation of the nominal operating mode at the cavity, voltage stand-off instabilities, parasitic oscillations, and increased stray radiation level. Several issues related to the two types of electron trapping mechanisms which can take place in gyrotrons were studied. Two MIG design criteria were proposed for the suppression of electron trapping in order to minimize the risk of possible problems. The major advantage of the proposed design criteria is that checking whether a design satisfies them or not is an easy and quick process requiring just a self-consistent electrostatic trajectory simulation code. The importance of the design criteria was also demonstrated by comparison and analysis of the experimental results of three different high power gyrotron tubes. Finally, several empirical design principles were defined for the satisfaction of both criteria. Influence of manufacturing tolerances in the emitter ring region.

An important sensitivity of the electron beam parameters of a MIG to the manufacturing imperfections in the emitter ring region has been demonstrated. In particular, it has been shown that not only the velocity spread can be significantly increased due to emitter ring imperfections but also the average pitch factor which can influence the mode excitation and the interaction efficiency at the gyrotron cavity. Furthermore, the formation of harmful long tails in the pitch factor distribution was also observed. This sensitivity can theoretically explain possible stochastic behavior of gyrotron tubes with identical scientific designs. It has also been shown that this sensitivity becomes more critical for thinner emitter rings. A factor has been defined for the quantification of the sensitivity. Furthermore, the influence of a possible misalignment of the emitter ring with respect to its neighboring parts on the pitch factor distribution has been analytically investigated. Then, a possible solution of this major issue for the gyrotron MIG designs was proposed by introducing anti-emission regions on the two ends of the emitter ring as shown in Fig. 1.3.2. Using this idea, it was possible to significantly decrease the sensitivity factor. In addition, an alternative approach was proposed for the cases in which a conventional emitter is used in order to suppress the harmful long tails in the pitch factor distribution.
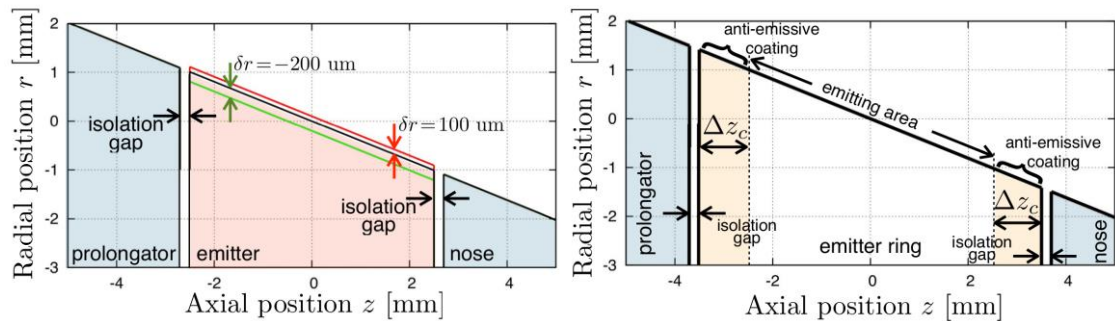
Fig. 1.3.2: Conventional (left) and the proposed type (right) of emitter ring which significantly decrease the sensitivity in the manufacturing tolerances.

1.3.3   Magnetic profile analysis

A simple analytical technique was proposed for the definition of the magnetic profiles used in the gyrotron experiments by three important parameters for the interaction and the beam quality instead of the arbitrary currents of the coils of the magnetic system. These parameters are (i) the magnetic field at the cavity, (ii) the beam radius at the cavity, and (iii) the angle of the magnetic field at the emitter. It was theoretically and experimentally demonstrated that two magnetic profiles are equivalent in terms of beam-wave interaction if the magnetic profile parameters are the same. Theoretical and experimental maps (see Fig. 1.3.3) were assembled in the magnetic profile parametric space for the SP prototype of the EU 170 GHz 1 MW CW gyrotron project. Many interesting conclusions were extracted while the magnetic profiles for the optimal operation of the tube were identified. Finally, it should be mentioned that the proposed methodology has been established as a standard procedure of the experimental investigation of the gyrotrons at IHM, KIT.
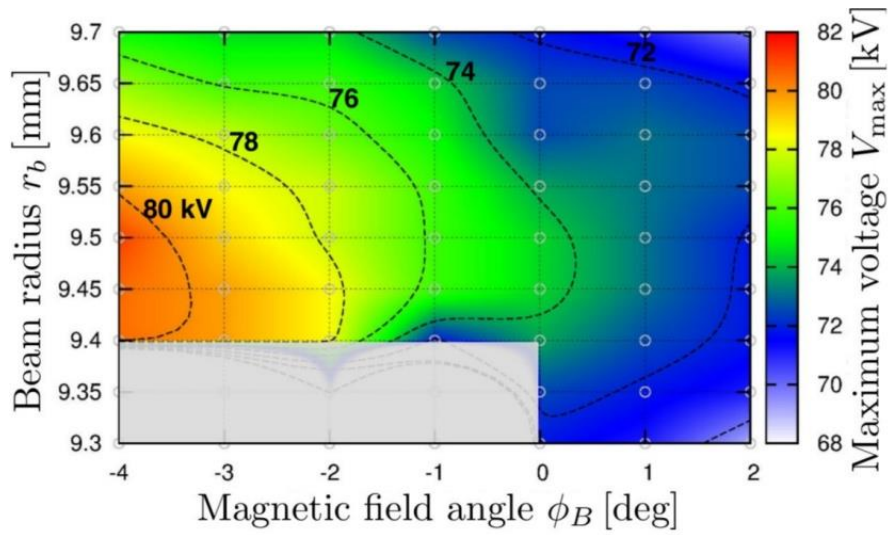
(a) Maximum voltage
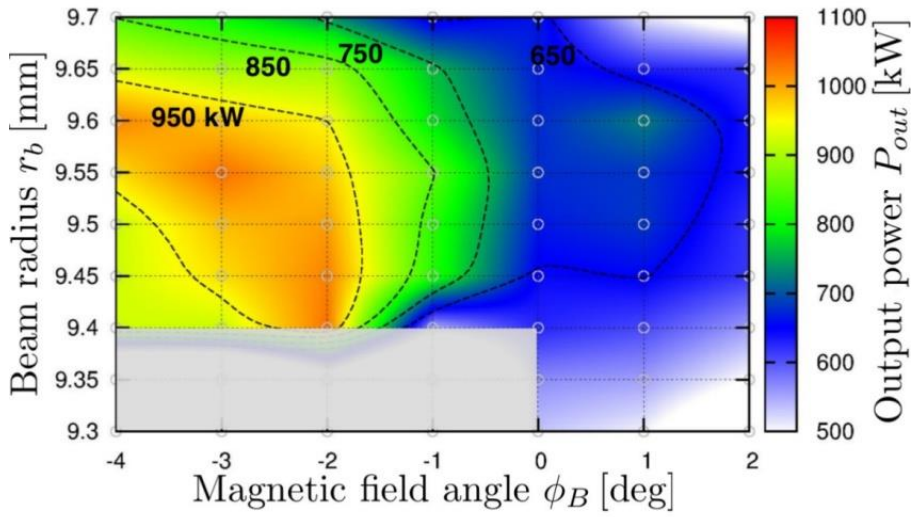
(b) Output power
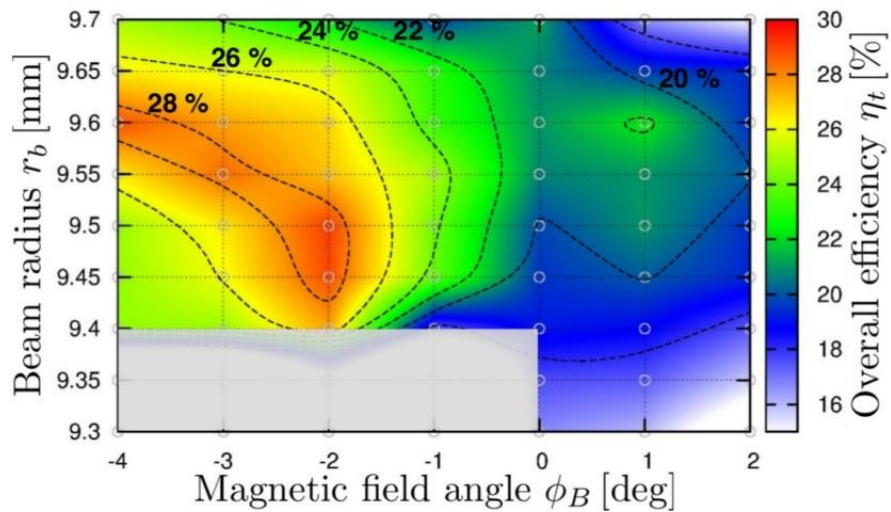
(c) Overall efficiency w/o depressed collector

Fig. 1.3.3: Operational maps of the short-pulse prototype of the 1 MW Gyrotron.

1.3.4 Investigation of the impact of tolerances on quasi-optical system

The first experiments with the EU 1 MW 170 GHz CW industrial prototype gyrotron for ITER have been completed in 2016. The mirror system in the CW gyrotron has been modified by reducing the thickness of the three mirrors by 200 μm. It is found that there are some misalignments in the 1st, 2nd and 3rd mirrors. The field distribution in the quasi-optical (QO) mode converter has been analyzed using SURF3D, and the simulation results show a good agreement with the long pulse high power experiment. Fig. 1.3.4 shows the field distribution at 0.25 m away from the gyrotron window.

The impact of tolerance on QO systems has been investigated. The possible fabrication errors of the launcher and the misalignment in the mirror system have been included in the analysis. For the mirror system in the EU ITER gyrotron, in order to keep the stray radiation in the quasi-optical mode converter to be <5 %, the deviation of the direction of the vector normal to the mirror surface should be smaller than 0.2° for each mirror.
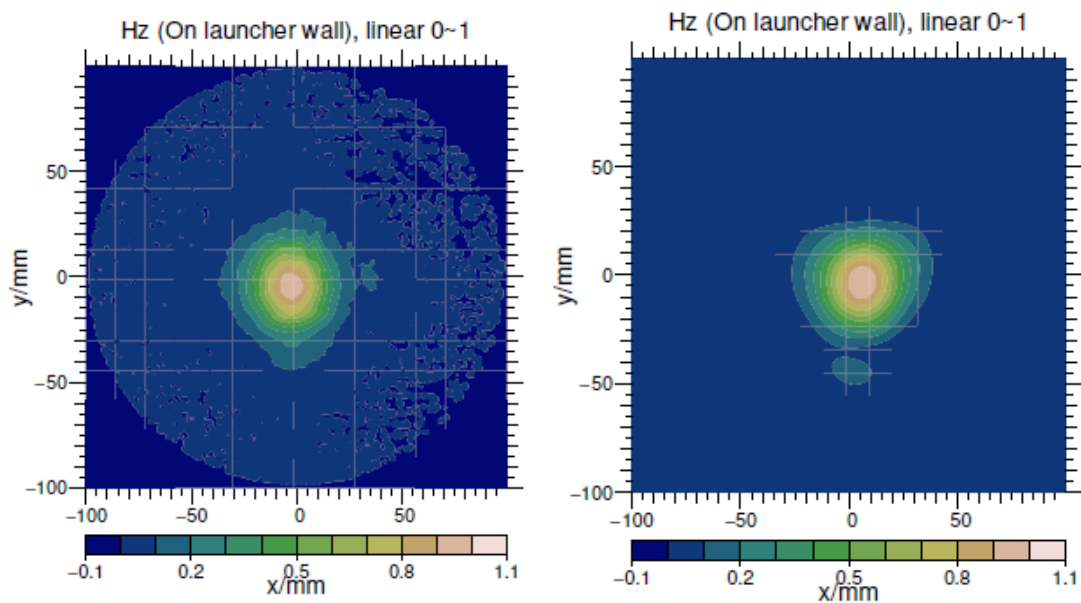
Fig. 1.3.4: The field distribution at 0.25 m away from the gyrotron window: experiment (left) and simulation (right).

1.3.5 Design of the quasi-optical mode converter and MOU for TCV gyrotrons

A quasi-optical (QO) mode converter has been designed for the dual-frequency TCV gyrotrons. The TCV gyrotrons will be operated at 84 GHz and 126 GHz, respectively. The simulation results show that the Gaussian mode contents are 98.74 % and 97.7 %, and the stray radiations are 3.42 % and 2.18 %, for the operation at 84 GHz and 126 GHz, respectively. A prototype of MOU for the TCV gyrotron has also been designed to transform the Gaussian-like distributions into an HE_{11} mode. The simulation results show that the conversion efficiency is quite sensitive to the parameters of the RF beams. It is impossible to achieve high conversion efficiency for both RF beams transformed in the same MOU mirror system.

A new subroutine for the transformation of the local coordinates of mirrors into the global coordinate system has been developed and integrated into the TWLDO code, and the global coordinates of the mesh points can be directly used as the input data for the SURF3D computer code. A subroutine for the propagation of the HE_{11} mode on the launcher wall has also been developed.

1.3.6   Development of a tool for the simulation of electromagnetic fields in quasi-optical systems of gyrotrons

Within the scope of a master thesis a simulation tool for the full wave calculation in quasi-optical (QO) mode converters based on the electric field integral equation (EFIE) was developed. The goal was a new, fast simulation tool, with a good scaling for highly oversized geometries and higher flexibility than available commercial tools. That provides a basis for further research and the development of new synthesis methods for QO systems. The mode converter separates the electron beam from the RF beam and transforms the cavity output, a high order cavity mode, to a fundamental Gaussian mode. Because of the high energy output and the continuous wave operation of gyrotrons used in fusion experiments, it is important to design very efficient quasi-optical mode converters with low stray radiation and a high Gaussian beam content in the output field. The developed simulation tool allows a full wave simulation of the electromagnetic fields in QO systems, based on the EFIE.

As a first example in Fig. 1.3.5 the simulation result for the QO system of the W7-X gyrotron is shown. The QO system consists of a launcher and three mirrors with a total area of 24700 λ^2, where λ is the wavelength at 140 GHz. Therefore, the QO system is highly oversized which is a challenge for every full-wave simulation method. Because of the high order method used in our simulation tool, the required number of unknowns for an accurate simulation can be reduced to $6 \cdot 10^5$ and we are able to simulate the whole system in only 90 minutes.
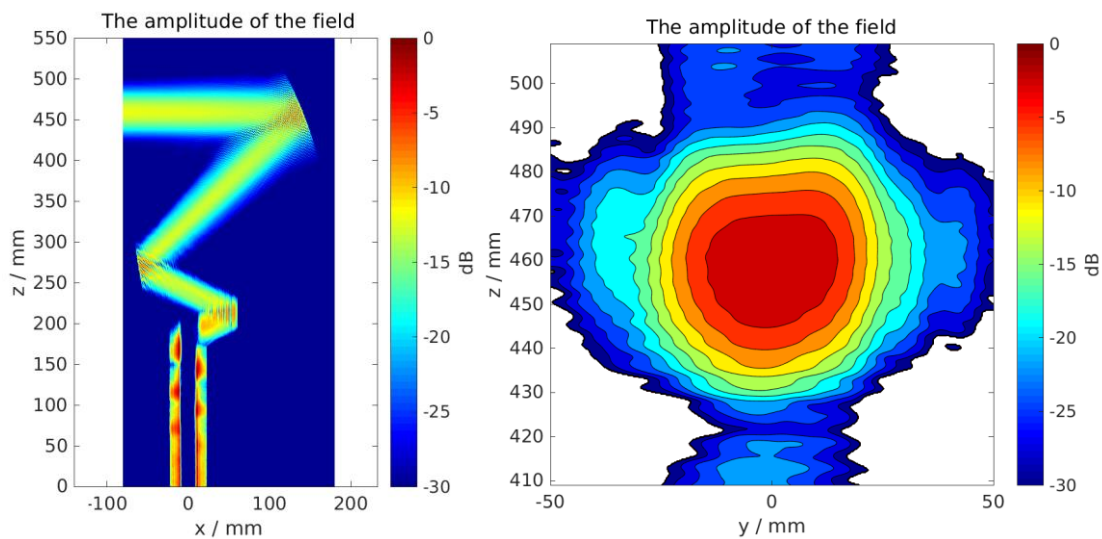
Fig. 1.3.5: Simulated electric field of the QO system for the W7-X gyrotron, in the x-z-plane (left) and at the output window (right).

1.4   Inverse Magnetron Injection Gun

1.4.1   Introduction

Gyrotrons are the unique RF sources which satisfy the exceptional requirements for ECRH of present and future fusion power plants. Previous experiments have already shown the operation of gyrotrons with an RF output power in the MW range, operating frequencies up to 170 GHz, and pulse lengths of several seconds up to continuous wave (CW). However, future nuclear fusion devices such as DEMO will require the development of gyrotrons with even higher frequencies (in the range from 200 GHz up to 300 GHz) at excellent efficiencies and multi-MW levels of RF output power in CW operation. To prevent mechanical

launcher steering, frequency step-tunable RF sources will be required for localized plasma stabilization. In order to fulfill the demanding requirements regarding increase of frequency and RF output power, an Inverse Magnetron Injection Gun (IMIG) has been designed and is under construction for the KIT 2 MW coaxial cavity gyrotron. This new IMIG (see Fig. 1.4.1) shall show the way towards a more robust operation at even higher output power levels. That shall be achieved by the implementation of a larger emitter ring, by doing a better post processing and by having significantly improved cooling conditions. Considering the fundamental beam and operating parameters, an excellent beam quality has been achieved in the simulations which results in a very low velocity spread. In addition, the IMIG fulfils the gun design criteria, which are published in and trapped electrons are suppressed in a much simpler way compared to the "conventional" MIG used in today's gyrotrons. Adapted from the triode configuration, the presented IMIG can also be operated in conventional hollow cavity gyrotrons as well as in the new KIT coaxial long pulse gyrotron under the fulfillment of the already mentioned gun design criteria.
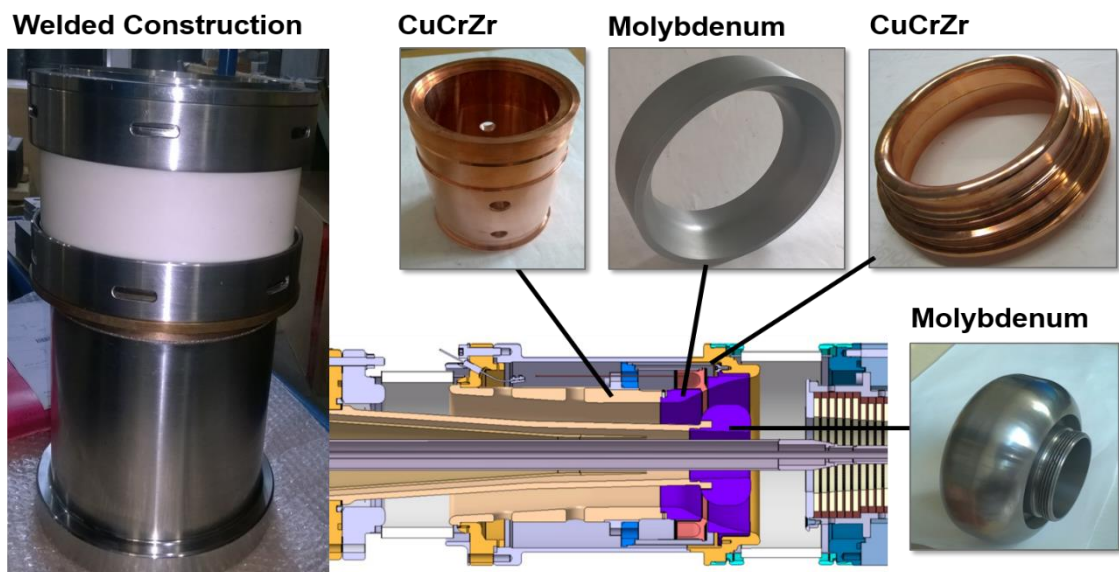
Fig. 1.4.1: 3D sketch of the Inverse Magnetron Injection Gun (IMIG) and the already manufactured subcomponents.

In the present design the emitter radius was fixed to 62 mm with a longitudinal emitter thickness of 5 mm. The emitter is slanted at an angle of 25 degrees with respect to the axis of the tube. The emitter is thermally isolated from the neighboring regions by the use of isolation gaps at both sides with a width of 200 μm. Due to the isolation gap an electric field enhancement is generated at the edges of the emitter. Hence, the emitter is embedded into the cathode structure by 70 μm.

The most important requirement of a MIG is the generation of a hollow helical electron beam with a high quality. Therefore, the design and tolerances of the beam forming components play an important role in the generation of a high quality electron beam. The displacement of the beam forming components is determined by (i) thermal expansion of the components during operation and (ii) by the manufacturing tolerances. The first item can be avoided by the consideration of the thermo-mechanical behavior, improved cooling conditions and the use of material compositions with high thermal conductivity.

The influence of the manufacturing tolerances (item ii) of the beam forming components regarding the beam quality will be explained and discussed in this paper. Furthermore, this work gives an estimation of the maximum permissible displacement of the main IMIG components. Therefore, a new mechanism for the investigation of three dimensional (3D) displacements of beam forming components will be proposed and presented.

1.4.2   Tolerance Study of the IMIG

The alignment and coaxiality of the anode, the position in the warm magnet borehole as well as the temperature distribution of the emitter has a significant influence on the quality of the electron beam, and therefore on the generated output power and efficiency. In the following, the influence and suppression of the mentioned tolerances will be discussed and benchmarked by the help of the simulation tool Ariadne.

Anode Misalignment

One of the most important criteria for a high-quality electron beam, is an homogenous distribution of the electric field strength at the emitter surface and therefore a perfectly aligned anode is required. Due to the large size of the anode (see Fig. 1.4.1) and the summation of all the mechanical tolerances, the correct alignment of the cathode to the anode is a critical issue and has to be minimized for mechanical implementation. In order to estimate the maximum allowable anode deviation, 3D simulations are required. Due to the fact that there is an 3D code missing to simulate the shifted geometry, a transformation of an 2D model into an 3D model was disposed. For this purpose, the anode was radially shifted in 5 µm steps in a range of ± 500 µm (d_1...d_n), which is shown in Fig. 1.4.2. For each distance the corresponding beam parameters were calculated and stored in a separate file. Subsequently, the different distances of the misaligned anode to the emitter were transformed into the 3D model and the resultant 3D beam parameters were recalculated. In Fig. 3d it is shown that the misaligned anode has no significant influence to the average pitch factor, however the pitch factor spread is increasing from 6.0 % (0 µm) up to 10 % (500 µm). With increasing anode misalignment, the pitch factor distribution is becoming wider (Fig. 3 b-c, blue colored). Assuming a thermal isolation gap of 300 µm instead of 200 µm the emitter is much more sensitive regarding the misalignment of the anode and the resultant beam parameters. Compared to the nominal gap width (200 µm) the pitch factor distribution at 300 µm (Fig. 1.4.3, red colored) is significantly wider for all radial anode deviations. Hence, the amount of electrons with higher pitch factor is increasing with increasing misalignment of the anode. With an anode misalignment of more than 300 µm the pitch factor exceeds the value of 2.2 which is more than the maximum allowable pitch value. Therefore, the generation of trapped electrons is starting and the generation of a Halo current will proceed. For the manufacturing process the presented tolerances were considered. A maximum gap width of 200 µm will be maintained in hot condition due to the consideration of the thermomechanical simulation results and the improved cooling conditions of the cathode by the use of advanced material compositions. Furthermore, the deviations of the anode will be smaller compared to a 'conventional' MIG, which is achieved by doing post processing after the brazing and welding process and by having significantly improved cooling conditions of the anode.
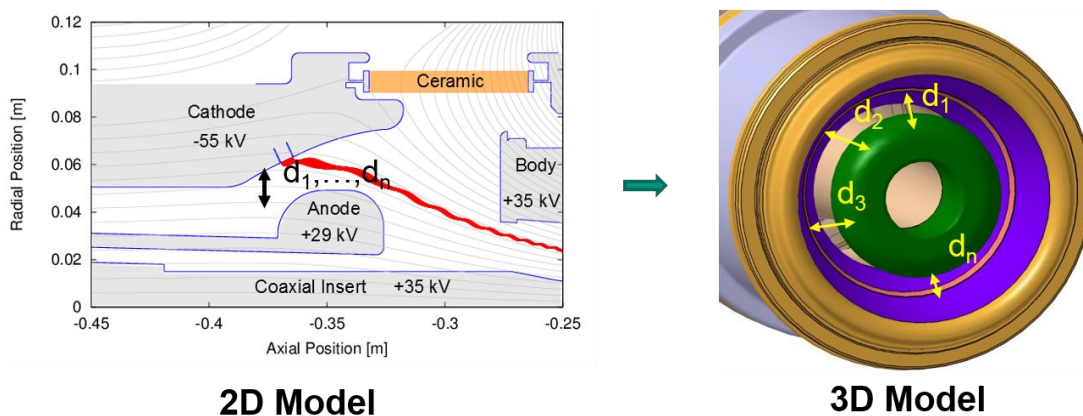
Fig. 1.4.2: Transformation procedure of the 2D into 3D model.

Emitter Misalignment

The radial emitter misalignment has also a significant contribution to the quality of the hollow electron beam. This radial misalignment is mostly related to a deviating emitter temperature and therefore a smaller or larger expansion of the emitter unit. In the following, the radial emitter displacements in the range of -150 µm up to +150 µm were investigated. The underlying assumption is a homogenous deviation over the full azimuthal emitter area. The definition of the positive and negative direction is shown in Fig. 1.4.4. The radial deviation of the emitter causes (i) a variation of the average pitch factor and (ii) a significant pitch factor variation of electrons which are emitted from the rear part of the emitter. In the nominal case (emitter deviation of 0 µm) the average pitch factor is 1.3 with a minimum spread of 6.0 % and a linear behavior over the investigated range, shown in Fig. 1.4.5. For a negative deviation of -150 µm the average pitch factor represents a value of 1.08, while the pitch factor at +150 µm amounts 1.58 with a spread of 10 % and 15.5 %, respectively.
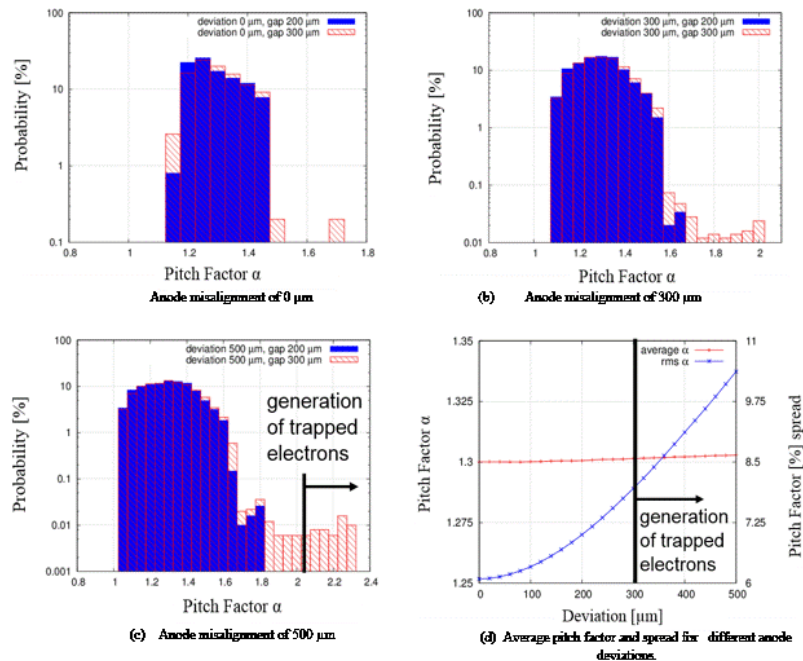
Fig. 1.4.3: Pitch factor distribution for different anode misalignments (a-c) with a gap width of 200 µm (nominal case, blue colored) and 300 µm (red colored), (d) describes the average pitch factor and spread for anode deviations in the range of 0 µm to 500 µm with a gap width of 200 µm.
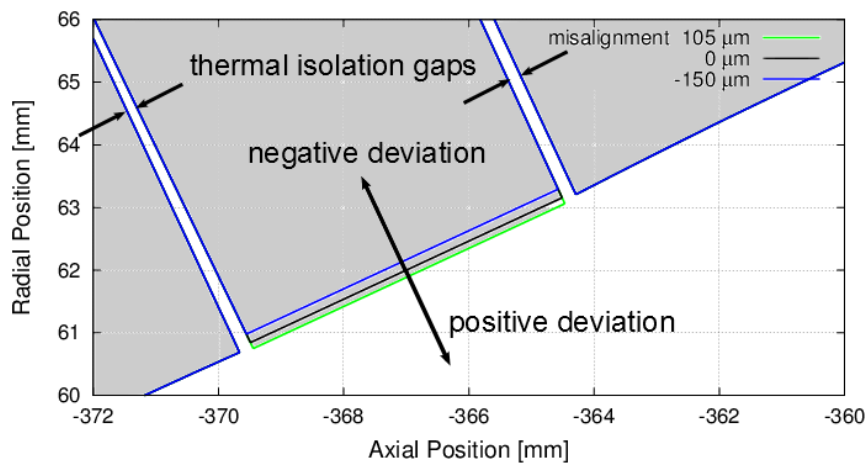
Fig. 1.4.4: Definition of the emitter deviation and representation of the thermal isolation gaps.
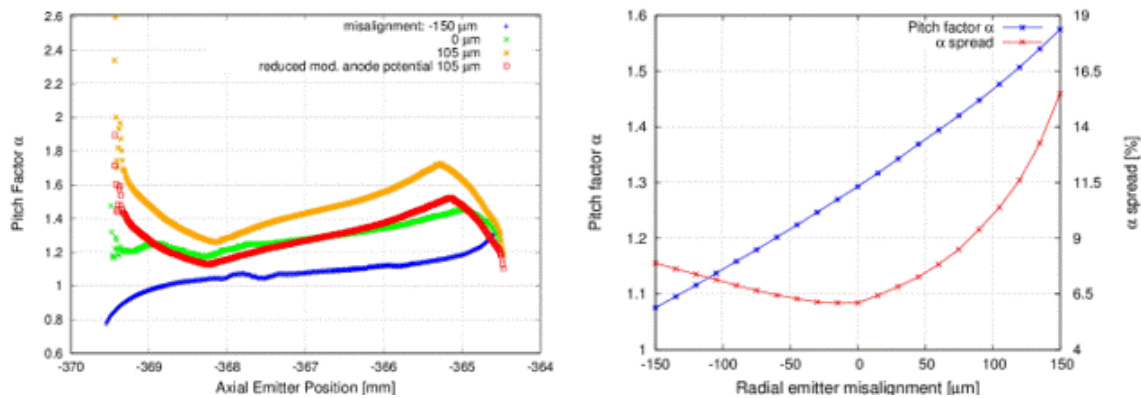
Fig. 1.4.5: Left: Pitch factor at the cavity as a function of the emitting point along the emitter surface for different radial misalignments. Right: Pitch factor and RMS α spread at the cavity center, regarding the radial misalignment

In particular, if the deviation is getting positive, the pitch factor of the electrons emitted from the rear part is increasing significantly and exceeds 2.6 for a misalignment of +105 µm, while for negative deviations the pitch factor of these electrons is decreasing. This effect is related to the strong variation of the electric field at the rear part of the emitter. The "edge effect" can be significantly reduced by the help of the modulation anode. Under the assumption of an average pitch factor of 1.3 and an emitter misalignment of 105 µm, the modulation anode potential has to be reduced from 29 kV (nominal case) to 26.5 kV. The pitch factor distributions for both cases are shown in Fig. 5a (orange and red color). It can be seen that the pitch factors of the electrons emitted from the rear part are reduced from 2.6 to 1.9, which is below the maximum pitch factor limit. Hence the misalignment of the emitter can be much easier compensated compared to the Magnetron Injection Guns which are currently used.

Temperature Inhomogenity at the Emitter Surface

The emission inhomogeneity of the gyrotron emitter depends mainly on the homogeneity of (i) the surface roughness, (ii) the BaO-layer, (iii) the electric field distribution and (iv) the temperature distribution. Those electron beam in-homogeneities create a non-uniform beam and an increase in the velocity spread of the emitted electrons. Measurement of the Current-Voltage characteristics is a simple and fast method to determine the emission inhomogeneity. The main contribution to the inhomogeneity of the electron beam is a non-uniform temperature distribution.

The temperature measurement of the inverse emitter at 1000 °C has shown an excellent temperature distribution of ± 7°C, which is 46 % less compared to a currently used MIG emitter. Under consideration of the temperature inhomogeneities the simulated pitch factor spread is slightly increasing from 6.5 % up to 6.7 %, shown in Fig. 1.4.6. With increasing temperature deviation the average pitch factor remains constant, while the spread is increasing to 10 % at ± 27 °C. The inhomogeneity of the temperature distribution has also a significant influence on the kinetic energy distribution. In Fig. 7 the kinetic energy of 20200 simulated electrons versus the azimuthal position in the cavity for a deviation of ± 0 °C (red colored) and ± 7 °C (nominal case, blue colored) can be seen. In case of ΔT = 7 °C the kinetic energy is lower in the regions of high temperatures, because the space charge is higher and therefore the resultant electric field lower. Consequently, the kinetic energy is higher at regions with lower temperature. As a result, the maximum decelerating voltage at the single stage depressed collector has to be reduced to the energy of the slowest electron, which decreases the overall gyrotron efficiency.
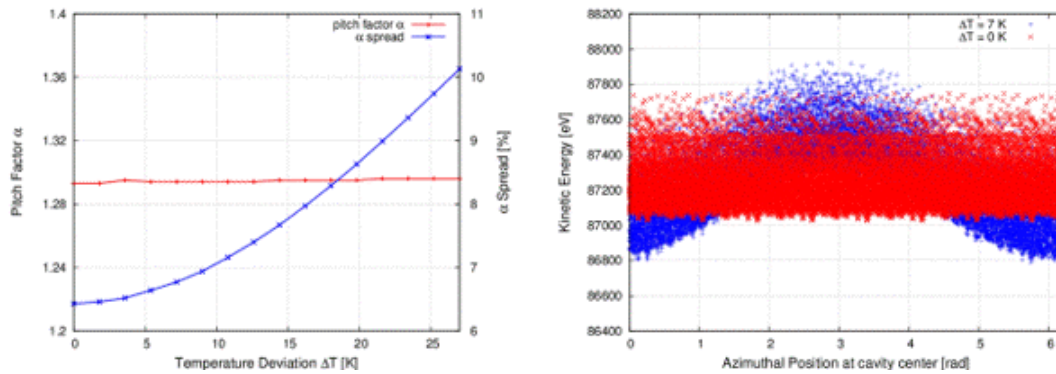
Fig. 1.4.6: Left: Pitch factor and RMS α spread simulated at the cavity center for different temperature deviations. Right: Kinetic energy as function of the azimuthal position at the cavity center for emitter temperature deviations of 7 K (blue points) and 0 K (red points).

Summary

In this work, the tolerance study of the Inverse Magnetron Injection Gun (IMIG) appropriate for the KIT coaxial- cavity gyrotron has been presented. The results have shown the dependency between misalignments, manufacturing tolerances, temperature distribution and the electron beam parameters, mainly the pitch factor and its RMS.

The work has also shown that the misalignment of the emitter, anode as well as the isolation gap has a significant contribution to the excitation of an electron beam halo and consequently the generation of low frequency oscillations. Therefore, the maximum acceptable displacement of each component has been presented in order to guarantee a stable gyrotron operation. It has been figured out, that the sensitivity of the IMIG is lower compared to the currently used 'conventional' MIGs and shows great promise for a stable operation without the generation of trapped electrons.

Additionally, the effect of emitter temperature inhomogeneity regarding the beam quality has been investigated based on IR-measurements.

Furthermore, the components were already manufactured with an excellent surface quality, taking into account the calculated permissible tolerances. Furthermore, excellent welding and solder joints for perfect vacuum conditions have been achieved.

1.5 EUROfusion: Research and Development towards a Gyrotron for future DEMO

1.5.1 Design and manufacturing of active-cooled subcomponents for a longer pulse 170 GHz, 2 MW coaxial-cavity gyrotron

Performance requirements for the gyrotrons for DEMO are operating frequencies above 200 GHz and output powers of 1-2 MW. Coaxial-cavity gyrotrons with inner conductor offer some advantages in comparison to conventional gyrotrons with a hollow circular waveguide cavity. Therefore, gyrotrons of coaxial-cavity type are a promising option for future fusion applications, and especially a promising solution for the operation at DEMO.

Impressive experimental results obtained with the KIT 2 MW, 170 GHz short-pulse coaxial-cavity pre-prototype have shown the large potential of the coaxial concept in the multi-MW operation regime.

Therefore, the main focus is the development and verification of a 2 MW, 170 GHz longer-pulse coaxial gyrotron with a pulse length up to a few seconds. This verification of the coaxial concept at longer pulses will open the path towards a mature coaxial gyrotron technology for DEMO.

In order to increase the gyrotron pulse length of the 2 MW coaxial cavity gyrotron all components have to be equipped by active cooling systems. The example of the conceptual design is shown in Fig. 1.5.1. One of the main requirements is the conservation of the modularity of the gyrotron. The concept is based on an independent cooling system implemented for each component. At a first step, the launcher, cavity and beam tunnel, are optimised for longer-pulse operation. The modifications will be described in the following and are shown in Fig. 1.5.2. Start of operation of the Coaxial Longer-Pulse Gyrotron is planned for the middle of the year 2017.

Launcher: The launcher together with the mirror system is responsible for the conversion of the main $TE_{34,19}$ mode into a fundamental Gaussian mode. During the mode conversion process the power loading at the launcher surface is very high. Especially the loading at the top part of the launcher and in the area of the launcher cut, where the complete RF-power is finally focused, is critical. In order to guarantee a stable operation also the top of the launcher will be cooled. This requirement meets some challenges, because the top part of the launcher is extended by 60 mm into the mirror box where no access for cooling pipes from outside of the gyrotron is possible. Therefore, the water entrance and outlet have to be supplied from the bottom and the water flow is implemented in a helix-like flow. At the top of the launcher, both helical channels will be connected in the so called "breakthtrough". In lower regions of the launcher the channels go into "reservoirs", where the channels end. Due to the complex structure, the channels have to be milled with a 5-axis milling cutter. In order to seal the channels, a stainless steel cover will be imposed and welded from the outside of the launcher. Due to the fact that the launcher and cover consist of different materials that have different thermal extension coefficient, a bellow is necessary to compensate the forces. In 2016 the launcher was successfully manufactured with an excellent surface quality. Furthermore, excellent soldered and brazed joints with a leakage rate $<10^{-12}$ mbar l/s were achieved with different material compositions.
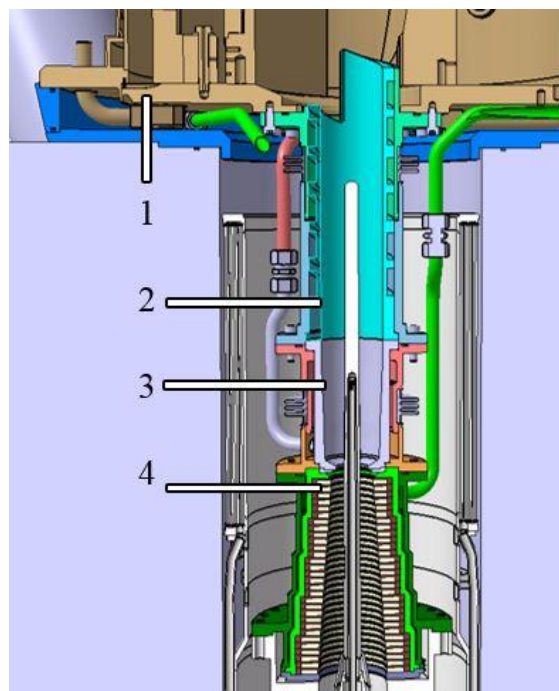
Fig. 1.5.1: Overview of the proposed cooling system for the most critical gyrotron subcomponents (1-mirror box, 2-launcher, 3-cavity, 4-beam tunnel).

Cavity: The cavity is the region where the RF power is generated due to interaction between the electrons and the RF field. The power loss at the surface of the cavity is 50 kW. The highest power loading (~2 kW/cm²) takes place at the centre of the cavity (region with constant diameter). It leads to a very high temperature gradient at the inner cavity wall, which results in thermal stress and deformation. The frequency of the RF wave depends strongly on the diameter of the cavity and hence strongly on the deformation and thermal expansion. Therefore it is essential to implement a water cooling system for the cavity in the longer pulse operation regime. The approach of the active cooling system is similar to the design of the launcher. However, due to the position and orientation a helical channel system is not necessary. The different temperatures, material properties of the cover and outer cavity wall require also the implementation of a bellow. The reduction of the water cooling gap (see Fig. 1.5.2) increases the flow velocity of the water and therefore the cooling efficiency. The limitation for the cavity is a maximum temperature of approximately 350°C at the inner surface. In a *COMSOL* simulation the temperature of a pulse with duration of 500 ms was calculated. At the centre of the cavity a maximum temperature of 280°C was predicted. The non-linear uptaper of the cavity was also extended and optimised. The simulation results predict a transmission efficiency of 99.85 % of the $TE_{34,19}$ mode and a low mode conversion in the uptaper. The design of the cavity was finalized and the manufacturing has started.
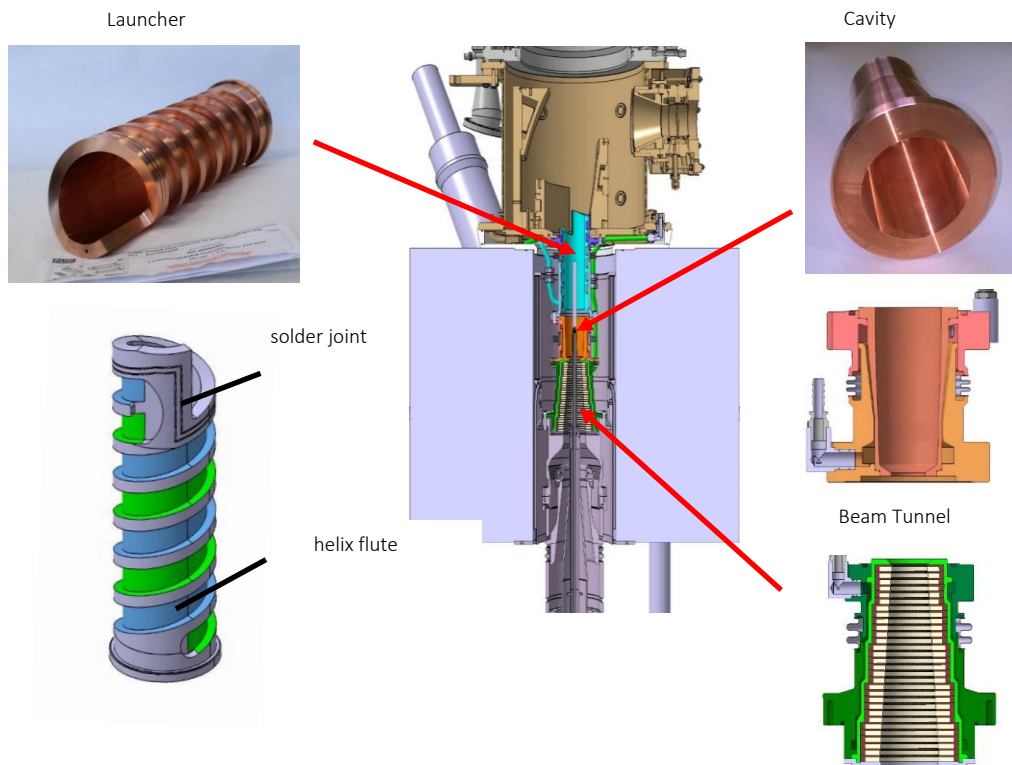
Fig. 1.5.2: Manufactured subcomponents of the coaxial long pulse gyrotron.

Beam tunnel: The beam tunnel consists of stacked copper and ceramic rings. The structure is very sensitive to the excitation of parasitic oscillations which might increase the power loading in the structure significantely (and destroy the good electron beam properties). Therefore an active cooling system is obligatory. Fig. 1.5.2 shows the construction of the beam tunnel including the water cooling system. An outer cover is also welded to the outside and forms with the outer metal layer an annular gap cooling. The subcomponents of the beam tunnel are already delivered and partly manufactured.

Mirror Box: In order to build a cost-effective gyrotron, the mirrors and the mirror box will be reused from an older industrial coaxial prototype gyrotron for ITER with slight modifications at the absorber ceramic,

collector, flanges, and window housing, in order to satisfy the requirements of the modularity. Currently, the mirror box is under preparation for the installation of the longer-pulse components. The water inlet for the beam tunnel, cavity and launcher is fixed at the bottom of the mirror box. Due to the fact that the gyrotron will operate in longer pulse operation it is necessary to bake it out at 350°C. Therefore, the water channels and connections have to be heat-resistant up to 350°C; hence metallic sealed components are required. In addition, a prototype metallic sealed water connection was made, which has shown excellent performance at the nominal operating water pressure.

1.5.2 Physical designs and tolerance studies of the key components for an 240 GHz gyrotron for DEMO

In-depth design studies of DEMO-compatible gyrotrons, starting with key components, are necessary to identify and overcome possible design and simulation obstacles and limitations. In order to obtain a full picture of such challenges, the two major concepts – conventional, hollow-cavity (or: cylindrical-cavity) and coaxial-cavity gyrotrons – are investigated in parallel in the frame of this work. Both gyrotron designs are based on the EUROfusion DEMO baseline 2012 (aspect ratio 4.0). However, most of the findings are applicable also to the updated DEMO baseline 2015 (aspect ratio 3.1). In 2016, the focus of work has been on fast frequency tunability (in steps of 2-3 GHz within roughly one second) and on multi-frequency operation (in leaps of 30-40 GHz without restrictions on tuning speed), as well as on tolerance studies. Investigations on output power maximisation (above 1 MW) with the conventional gyrotron concept were also performed. The coaxial-cavity design was optimised for good efficiency, while maintaining the technical boundary conditions at present-day conservative levels. The key parameters of the two designs are given in Table 1.5.1.

Table 1.5.1: Key parameters of the two gyrotron designs.

Parameters (ideal beams)	Coaxial Concept	Conventional Concept
Frequency (GHz)	237.5	236.0
Interaction mode	$TE_{49,29}$ (Eigenvalue ≈ 158)	$TE_{43,15}$ (Eigenvalue ≈ 103)
Beam Current (A)	69.3	43
Beam Voltage (kV)	85.6	61
Magnetic Field (T)	9.58	9.175
Output Power (kW)	1900	920
Interaction efficiency η_{elec} (%)	33	36

Coaxial-cavity 2 MW design

In 2014-2015, the basic coaxial-cavity design was finished, including multi-frequency compatible mode selection, cavity design with coaxial insert, Magnetron Injection Gun (MIG) based on a realistic magnet design, and initial concepts for the description of misalignments and nonuniform voltage depression. Those concepts have been developed further and applied to the DEMO gyrotron design in 2016.

The coaxial insert, fixed at the MIG of the gyrotron and reaching through the cavity area, is intended to rarefy the mode spectrum in the cavity, and consequently, reduce mode competition and increase operation stability. In order to achieve this, it is tapered and has longitudinal corrugations in the cavity. While the typical dimensions within the cavity are of the order of 1 mm (free-space wavelength at 238 GHz: 1.26 mm; required corrugation width/depth: ca. 0.3 mm), the insert length is around 50 cm, leading to a maximum permitted tilt of below 0.1°. As gyrotrons are welded and evacuated after assembly, misalignment compensation can only be achieved using the magnetic field (electron beam position) or external screws (insert position/tilt), which might be possible only up to a certain precision. Therefore, investigation on effects of residual misalignments of electron beam and coaxial insert is important.

Effect of insert misalignment on the TE modes

For insert misalignment below 1 mm, the deformed main mode as well as its competitors remain practically constant with the cavity wall, as has been demonstrated using the 2D eigenmodes solver of COMSOL. Correspondingly, mode eigenvalues (i.e. eigenfrequencies) and couplings to the electron beam do not change significantly. However, those small changes can influence the outcome of time-dependent multi-mode interaction simulations substantially, which is why the properties of the deformed modes have to be determined with high precision. In view of this, the code SCNCHIMP has been developed, which can express the Transverse Electric (TE) modes of a misaligned cavity in terms of TE modes in rotationally symmetric cavities. SCNCHIMP is developed to address

- Misalignment up to   1 mm,
- Eigenvalues up to   180,
- Eigenvalue precision of 10^{-7}, and
- Azimuthal indices m up to   60.

The corrugated insert is described using the surface impedance model (SIM), provided the corrugation width is sufficiently smaller than the azimuthal wavelength. The underlying calculations are based on a field decomposition over axial cross-sections that has been adapted from the literature to determine mode eigenvalues more efficiently, supplemented by routines that ensure consistent mode numbering along the cavity axis. An interface from SCNCHIMP to the code-package EURIDICE for gyrotron interaction simulations has been initiated and needs further verification until reliable interaction simulation results can be obtained.

Besides the stray radiation in the gyrotron due to parasitic modes generated by beam-wave interaction or by a non-perfect quasi-optical mode converter (launcher) and mirrors, there is additional stray radiation because of the coaxial insert. This stray radiation is caused by the inevitable mode conversion at the end of the insert and it increases rapidly with increasing insert misalignment. Increased levels of stray radiation can impede proper operation of the tube. Using the above mentioned field decomposition one can determine the ratio of powers between stray radiation and proper radiation. More details are given in Fig. 1.5.3.

For the coaxial-cavity design considered here, an insert misalignment above 150 μm would lead to an in-gyrotron stray radiation of 4 % (additionally to the other sources of stray radiation). This level would probably be too high for reliable operation at 2 MW.

Effect of insert misalignment on the electron beam

Since typical modes remain concentric with the cavity wall, as long as the coaxial insert is only moderately misaligned (which covers all reasonable scenarios), the electron beam has to be kept aligned with the cavity wall as well, in order to couple well to the operating mode. Unfortunately, such a configuration leads to

inhomogeneous electrostatic potential (voltage depression) around the beam circumference, and, consequently to an increase of the kinetic energy spread of the beam electrons and therefore a reduction of the interaction efficiency. In order to quantify this reduction a detailed description of the voltage depression distribution is necessary.
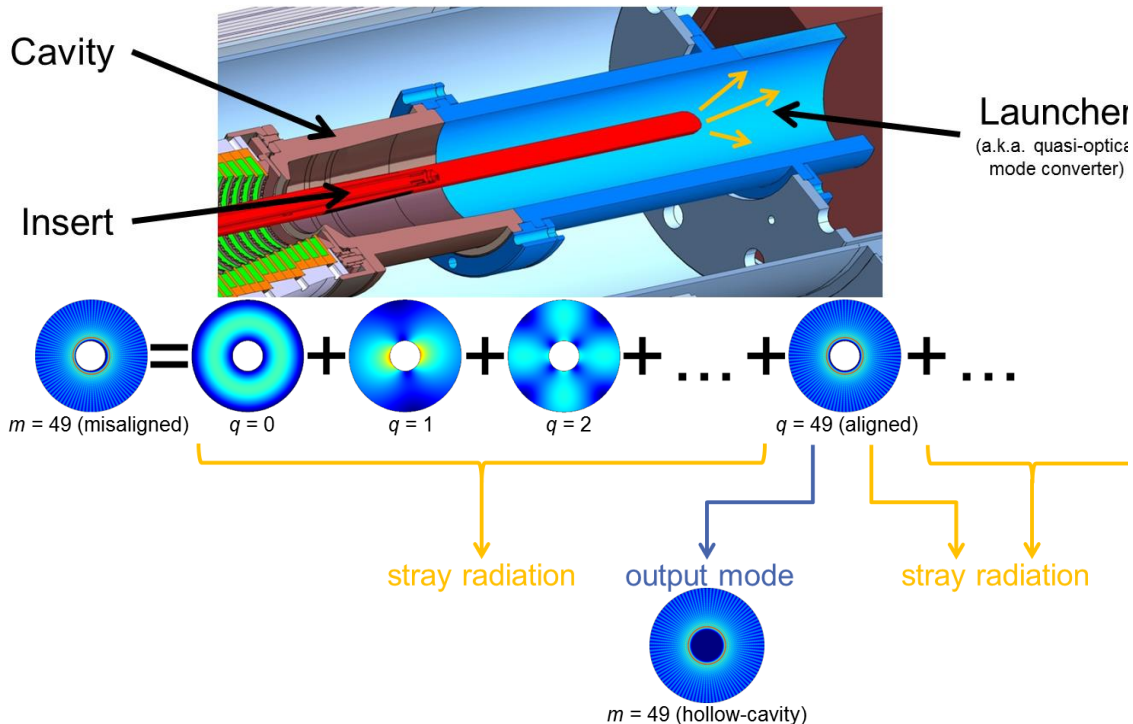
Fig. 1.5.3: Upper: Cavity, insert and launcher of a coaxial-cavity gyrotron. The origin of insert-induced stray radiation is indicated by orange arrows. Lower: Schematic field decomposition of the misaligned-cavity mode TE$_{49,29}$ into aligned-cavity field components q, and subsequent extraction of hollow-cavity mode TE$_{49,29}$ from the dominant field component $q=m=49$. Field components of azimuthal symmetries other than $q=49$,as well as (mostly) the Neumann part of component $q=49$ will contribute to stray radiation after the end of the coaxial insert, leaving only the Bessel part of component $q=49$ as the desired hollow-cavity mode TE$_{49,29}$ with the design frequency.

In practically no geometry, except for perfect alignment, voltage depression can be expressed in closed analytic form. However, using truncated series of mirror charges, it was shown that it is possible to find excellent approximations for the voltage depression on beam electrons in arbitrarily misaligned cavities (including hollow cavities) and with arbitrary beam shapes. In the coaxial-cavity design considered here, a misalignment of 500 μm leads to an energy variation of 1 keV (1.17 % of the beam kinetic energy), which would probably impede proper gyrotron operation severely. Therefore, the aforementioned maximum misalignment of 150 μm seems to be a reasonable value also if voltage depression is considered.

Hollow-cavity 1 MW design

For DEMO ECRH&CD, the fundamental design of a 236 GHz, 1 MW hollow-cavity gyrotron has been initiated in 2014. Considering the multi-frequency operation of the gyrotron for multi-purpose operations, suitable operating modes have been chosen at 170 GHz, 203 GHz, 236 GHz and 269 GHz. Using a systematic cavity design approach, all the physical parameters of the interaction section have been fixed and the optimum operating parameters of gyrotron have been finalised, taking into account the interaction efficiency requirement and a wall loading limit of 2 kW/cm^2. The feasibility of the design is further verified for a 2-3 GHz fast-frequency step-tunability, to achieve plasma instability control with a fixed EC launcher. The beam misalignment tolerance has also been estimated using a new macro-electron beam based technique.

The realistic electron beam parameters (velocity spread: 6 % (rms), radial width: $\lambda/4$) and realistic conductivity of Glidcop material have been used for the multi-mode, time-dependent simulations, which suggest stable output of 920 kW with an interaction efficiency of 36 % (without depressed collector). As per the EUROfusion baseline 2012, in total 50 MW power are required for ECRH&CD application. High output power per tube is always desirable, which eventually leads to a minimised number of tubes per plant, as this will increase reliability and cost-effectiveness of the heating system.

In 2016, different generic approaches were suggested to identify the mode eigenvalue limit for stable operation considering mode competition. This limit is directly related to the power limit for the hollow cavity concept. After obtaining the eigenvalue limit, a new cavity design and operating parameters are proposed for 1.5 MW, 236 GHz gyrotron operation. The possibilities of an advanced, triode start-up scenario were also investigated.

Eigenvalue Limit Analysis

The solution for high power operation is to use a very high order mode (e.g. eigenvalue > 103 for a 236 GHz gyrotron). For a particular hollow-cavity operating mode, its eigenvalue is a root of the derivative of the Bessel function. As the radius of a cavity is directly proportional to the mode eigenvalue, by using a high-order mode it is possible to increase the area of the cavity wall, which significantly reduces the maximum wall-loading. However, it should be noted that the mode spectrum density increases with high order modes and it may not be possible to excite the desired mode, due to critically high mode competition. For a particular operating frequency, it is very important to know the eigenvalue limits for stable operation, which would allow choosing the most suitable mode within the eigenvalue limit and thus achieve the highest output power.

The list of selected modes for this analysis is presented in Table 1.5.2. Within an eigenvalue range from 105 to 145, nine modes are selected with approximate eigenvalue separation of 5 and having a relative caustic radius of 0.41. The selected modes are named as 'DM1' to 'DM9' in ascending order of eigenvalue. Different cavity geometries are considered for analysis, in which the radius of the interaction section is selected according to the operating modes. The cavity radius increases with the eigenvalue, which increase the total power handling capability of the cavity for the same wall-loading. Due to the same relative caustic radius, the behavior of these modes is identical, except the mode competition: mode competition increases linearly with the increase in eigenvalue.

To investigate the effects of mode competition, two generic approaches are suggested using linear and non-linear gyrotron theory. Considering the linear, fixed-field theory of the gyrotron, the influence of the electron beam on the field profile is neglected and the mode eigenvalue limit is estimated using (i) starting current calculations and (ii) analysis of the mode coupling versus frequency. These methods suggest a stable gyrotron operation until a mode eigenvalue of 125 (DM5 mode), which corresponds to the output power of 1.5 MW.

Table 1.5.2: Selected high-order modes considered for this analysis with their corresponding parameters. All the selected modes are having nearly same relative caustic radius of 0.41-0.42.

Mode name	DM0	DM1	DM2	DM3	DM4	DM5	DM6	DM7	DM8	DM9
Mode	$TE_{43,15}$	$TE_{44,15}$	$TE_{45,16}$	$TE_{48,17}$	$TE_{50,17}$	$TE_{52,18}$	$TE_{53,19}$	$TE_{56,20}$	$TE_{58,20}$	$TE_{59,21}$
Eigenvalue	103.21	104.46	109.17	116.4	118.91	124.87	129.58	136.8	139.32	144.02
Cavity radius (mm)	20.88	21.14	22.09	23.55	24.06	25.26	26.22	27.68	28.19	29.14
Beam radius (mm)	9.06	9.28	9.49	10.10	10.51	10.93	11.13	11.75	12.16	12.37
Rel.caustic radius	0.41	0.42	0.41	0.41	0.42	0.42	0.41	0.41	0.42	0.41
Diffractive Q	1443	1445	1457	1483	1493	1573	1533	1553	1559	1567

In the case of non-linear, self-consistent theory, the modification of the axial field profile due to the high-frequency component of the electron beam is taken into account. Initially, the optimized operating parameters for the individual operating mode are determined considering only single-mode interaction without including the neighbouring modes in the self-consistent interaction simulations with EURIDICE. In the single-mode case, the stable operation is achieved with all selected modes (DM1-DM9). As a next step, all the neighbouring modes being within the -5 % to +10 % frequency range and having a relative coupling coefficient of more than 50% are selected for the multi-mode, time-dependent, self-consistent simulations of the diode start-up. In Fig. 1.5.4, the RF behaviour of the DM5 mode (eigenvalue ~ 125) and DM7 (eigenvalue ~ 135) are compared. In the case of DM5, the stable excitation of the operating mode $TE_{52,18}$ is possible. On the other hand, because of the dense mode spectrum, the desired operating mode $TE_{56,20}$ is not excited in the case of DM7. This analysis of the selected modes using non-linear, self-consistent, multi-mode simulations also suggests mode eigenvalue limit of 125 for a 236 GHz hollow-cavity gyrotron.

In summary, assuming diode start-up and realistic electron beam parameters, both suggested methods predict stable operation with modes having eigenvalues up to 125, which corresponds to a maximum output power of around 1.5 MW.
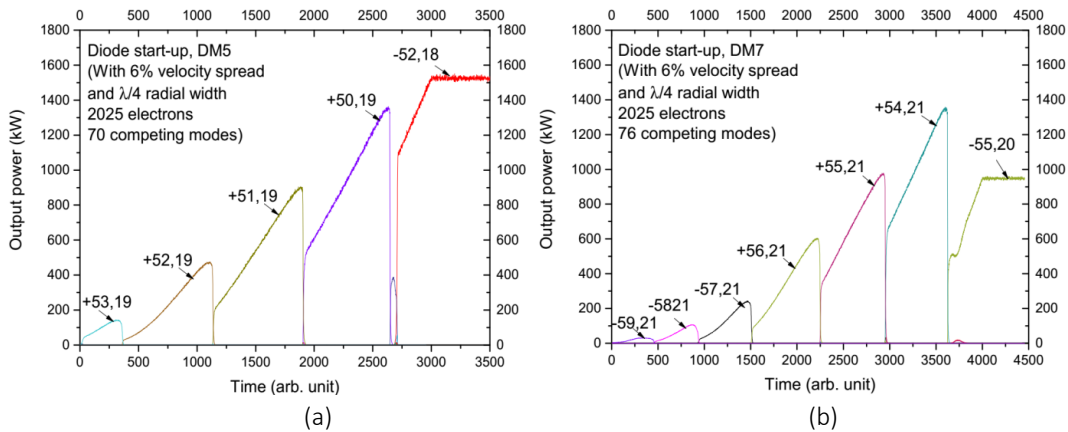
Fig. 1.5.4: Multi-mode, self-consistent, diode start-up analysis for (a) DM5 and (b) DM7 mode.

Triode type start-up scenario

The triode-type start-up scenario has been investigated to control mode competition with high-order modes, which can further increase the output power. In Fig. 1.5.5 the diode-type start-up scenario is compared with the triode-type start-up scenario: In diode start-up, the beam energy increases linearly with the applied accelerating voltage, while the velocity ratio α is increasing following the adiabatic approximation. In the case of triode start-up, using the modulation anode, the velocity ratio can be controlled individually. The triode start-up scenario was proven to be an effective method to control mode competition and stable output could be achieved until a mode eigenvalue of 145 (DM9). The modes excited during the start-up process can be controlled by a proper selection of the transition phase, i.e. of the voltage range in which the velocity ratio is quickly increased.

In the case of a hollow cavity gyrotron, the voltage depression is very critical for high-order volume modes. The detailed analysis of the effects of space charge neutralisation is under investigation. In addition to that, the possibilities of new hybrid-type start-up scenarios should be also studied, which consider neutralisation effects during a slow triode start-up.
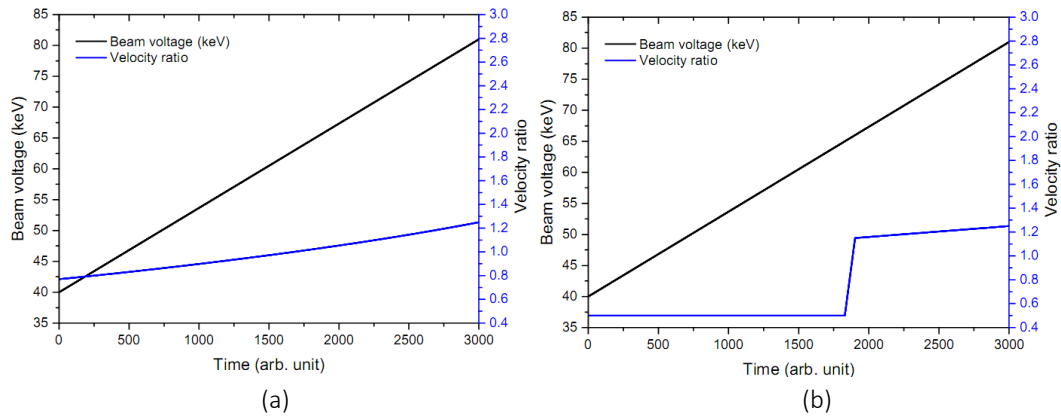
Fig. 1.5.5: Comparison of (a) diode type and (b) triode-type start-up scenarios.

1.5.3 Upgrade of the code-package EURIDICE to address coupled modes

An upgrade of the code-package EURIDICE for gyrotron interaction simulations and cavity design has been initiated, in order to simulate the interaction of an electron beam with azimuthally coupled electromagnetic modes in gyrotron cavities that are not rotationally symmetric. The motivation has been the support of studies, within EUROfusion PPPT WPHCD, involving such cavities. These are coaxial cavities with mode-converting corrugations on the outer wall (*Z. C. Ioannidis et al., Journal of Infrared, Millimeter, and Terahertz Waves 36, 2015*) and coaxial cavities with misaligned coaxial insert (see section 1.5.2). The upgrade has been completed in terms of mathematical formulation and programming. Work on creating interfaces between EURIDICE and the codes calculating the electromagnetic field structure in coaxial cavities with corrugated outer wall or misaligned insert has also been initiated.

Representation of the high-frequency electromagnetic field

In the gyrotron cavity, the electron beam is assumed to excite TE modes. The high-frequency electromagnetic field at the vicinity of the electron beam is represented as a sum of TE modes of a cylindrical (or coaxial) waveguide. All field components of a TE mode can be derived from its axial magnetic field $\text{Re}\{H_z\}$, where:

$$H_z = f(z)\psi(r,\varphi,z)e^{i\omega t} .$$

The eigenfunction ψ describes the transverse structure of the electromagnetic field and the field profile function $f(z)$ describes the axial structure along the cavity axis z. The eigenfunction ψ may slightly vary along z-axis, to account for the mild axial non-uniformity of the geometry. It obeys the Helmholtz equation at each cross section:

$$\nabla_\perp^2 \psi\left(r,\varphi;z\right) + k_\perp^2\left(z\right)\psi\left(r,\varphi;z\right) = 0, \qquad k_\perp = \chi/R_o \, ,$$

where χ is the mode eigenvalue, obtained from the characteristic equation involving the boundary conditions for the field in the transverse cross section, and R_o is the radius of the cavity's outer wall.

The average stored electromagnetic energy can be calculated as

$$W_{em} \approx 2W_e = \frac{1}{2}\int_{z_{in}}^{z_{out}} \frac{Z_0}{c}\left[\frac{\omega^2}{c^2 k_\perp^2}\right]\frac{\left|f\left(z\right)\right|^2}{k_\perp^2 C^2}dz, \quad Z_0 = \left(\mu_0/\varepsilon_0\right)^{1/2}, \quad C^2 \triangleq \frac{1}{\iint_{S(z)}\left|\nabla_\perp \psi\right|^2 dS} \, ,$$

where $S(z)$ is the surface of the resonator cross-section at position z. The average ohmic wall loading of the outer (o) and inner (i) wall at each cross section can be written as:

$$\rho_{o,i}\left(z\right) = Z_0 \frac{\pi}{2}\frac{\delta}{\lambda}\left[C_{zo,i}\left(z\right)\left|f\left(z\right)\right|^2 + C_{\perp o,i}\left(z\right)\frac{1}{k_\perp^2}\left|f'\left(z\right)\right|^2\right],$$

where $\lambda = 2\pi c/\omega$ and the unitless positive quantities $C_{zo,i}$, $C_{\perp o,i}$ can be evaluated using the expressions for the electromagnetic field.

EURIDICE upgrade

For rotationally symmetric gyrotron cavities, the eigenfunction $\psi_{mp}(r, \varphi; z)$ of a TE$_{mp}$ mode at the vicinity of the electron beam has the form:

$$\psi_{mp}\left(r,\varphi;z\right) = \left[AJ_m\left(k_{\perp mp}r\right) + BY_m\left(k_{\perp mp}r\right)\right]e^{-im\varphi}, \quad k_{\perp mp} = \frac{\chi_{mp}\left(z\right)}{R_o\left(z\right)}, \tag{1.5.1}$$

where the integer m is the azimuthal index of the mode, and J and Y are the Bessel and Neumann function, respectively. In the case of the hollow cylindrical cavity, $A = 1$, $B = 0$, and the eigenvalue χ_{mp} is the p-th root of the characteristic equation $J_m'(\chi) = 0$. In the case of a coaxial cavity with smooth insert or with an insert with impedance corrugation, we have $A = 1$, $B = -J_m'(\chi_{mp}) / Y_m'(\chi_{mp})$, and the eigenvalue χ_{mp} is the p-th root of the characteristic equation (9) in (*Iatrou et al., IEEE Trans. Microwave Theory Tech. 44, 1996*).

All these rotationally symmetric cases can be addressed by EURIDICE, that is, the eigenvalue χ_{mp}, the eigenfunction ψ_{mp}, and the relevant coefficients C^2, $C_{zo,i}$, $C_{\perp o,i}$ are calculated and are used for the simulation of the beam-wave interaction. However, in the case of non-rotationally symmetric cases, the eigenfunction has the following expression, which reflects the coupling of azimuthal modes invoked by the breaking of the rotational symmetry:

$$\psi_{mp}\left(r,\varphi;z\right) = \sum_{q=1}^{N}\left[A_q J_{m+n_q}\left(k_{\perp mp}r\right) + B_q Y_{m+n_q}\left(k_{\perp mp}r\right)\right]e^{-i\left(m+n_q\right)\varphi}, \quad k_{\perp mp} = \frac{\chi_{mp}}{R_o}. \tag{1.5.2}$$

Here, n_q is integer and the sum over q is limited to N terms (rather than infinite terms) for numerical reasons, assuming that N is chosen as large as necessary for the field to be described with the appropriate

accuracy. The expression 1.5.1) is consistent both with that for coaxial cavities with mode-converting corrugations on the outer wall, and with that for coaxial cavities with misaligned corrugated insert.

The calculation of the eigenfunctions of the resonant modes in the non-symmetric cases, i.e. the calculation of the eigenvalues χ_{mp} and the coefficients A_q, B_q, is a complex task and dedicated codes have been developed, namely CCCI (*Z. C. Ioannidis et al., Journal of Infrared, Millimeter, and Terahertz Waves 36, 2015*) for the coaxial cavities with corrugations on the outer wall, and SCNCHIMP (see section 1.4.2) for the coaxial cavities with misaligned insert. Since the eigenfunctions and the coefficients C^2, $C_{zo,i}$, $C_{\perp o,i}$ are necessary for beam-wave interaction simulations in EURIDICE, an interface file has been designed, which will be used to import these quantities from CCCI and SCNCHIMP to EURIDICE. The usage of the interface file has been implemented in EURIDICE.

The generalisation of the eigenfunction expression from (1.5.1) to (1.5.2) has additional consequences besides the change in the coefficients C^2, $C_{zo,i}$, $C_{\perp o,i}$. It also affects the coupling coefficient G_{mp} between the electron beam and the TE$_{mp}$ mode. The expression for G_{mp} in the rotationally symmetric case is the following:

$$G_{mp} = A J_{m-s}\left(k_{\perp mp} r_{gc}\right) + B Y_{m-s}\left(k_{\perp mp} r_{gc}\right),$$

where r_{gc} is the radius of the guiding centre of the electron on the transverse plane and s is the cyclotron harmonic number. After the generalisation (1.5.2) for the eigenfunction, the expression for the beam coupling coefficient has to be updated accordingly. This was done and the new expression was numerically implemented in EURIDICE, both in the interaction codes and in the code for the calculation of the starting currents of the modes.

1.5.4   Specifications for a superconducting magnet and contacts with suppliers

The objective has been the detailing of the specifications of a 10.5 T superconducting magnet (SCM), to support the > 200 GHz gyrotron development towards DEMO. Contact to magnet suppliers has been already initiated, kept up, and intensified during the years 2014 and 2015. At the beginning of 2016, it was decided to send requests for a tentative budgetary offer to possible suppliers. For this request, a list of requirements, which has been already defined in the year 2015 has been slightly relaxed to increase chances to get reasonable budgetary offers from possible suppliers. The maximum on-axis magnetic induction at the center oft the cavity will be 10,5 T, the minimum borehole diameter will be 240 mm. In order to ensure a high flexibility the different coils must be controlled individually.

In March 2016, a number of possible suppliers have been contacted and asked for budgetary offers based on the relaxed list of requirements. This started intensive discussions during the following months (via e-mail, video-conferences and direct visits of company representatives at KIT), indicating critical challenging problems of the proposed requirements. After July 2016, two additional companies were contacted and they also showed interest in this project.

The response received from several companies during 2016 finally indicated that the construction of the proposed 10.5 T magnet is feasible. Based on the gained information, a detailed list of specifications started to be compiled at the end of 2016, in order to launch a call for tender in the first quarter of 2017.

1.5.5   Investigations on multistage depressed collectors

The study of Multistage Depressed Collectors (MDC) has been continued. In particular, more studies on the collectors based on **E×B** drift have been done. The conceptual idea proposed in the previous year has been

studied in details. A systematic way has been found to optimise the auxiliary coils in the MDC to transform the annular electron beam to sheet beams. With this method, the thickness of the sheet beam can be optimised. Since the thickness of the sheet electron beam is related to the efficiency of the E×B MDC, the understanding of the way to optimise the magnetic field for the beam-shape transformation is important. Moreover, three new ideas on concepts for E×B collectors, intended to be simpler than the concept proposed in the previous year, have been investigated. Conceptual models have been simulated, yielding promising results. The first two concepts are based on the $B_z \times E_y$ drift. In the first concept, the annular electron beam is transformed to an elongated elliptic beam. The elongated elliptic electron beam can be handled like a sheet beam and a known technique for sheet electron beams (*Pagonakis et al., Physics of Plasmas 23, 2016*) can be directly used to collect this elliptic electron beam. The second concept splits the annular electron beam to two sheet beams in semi-circle shapes. It is based on the same principle as the first concept, but can handle the annular electron beams, which enclose high magnetic flux. The third concept is based on $B_z \times E_\varphi$ drift. The azimuthal component of electric field is created by a pair of helical electrodes and the drift is radial in this case.

Optimization of the magnetic field for the previous MDC concept

In the previous "wing" concept, the coils used to transform the electron beam should only have current in axial direction. The coils have arc-shape cross sections, shown in Fig. 1.5.6. This may not be the optimum shape. In order to describe the magnetic field lines in a better way, the flux coordinate (a.k.a. Clebsch form of magnetic field) is used. The magnetic flux density **B** in Clebsch form is formulated by the cross product of two scalars:

$$\boldsymbol{B} = \boldsymbol{\nabla}\alpha \times \boldsymbol{\nabla}\beta \ .$$

In this special case, all relevant coil currents are axial, i.e., $\boldsymbol{J} = \hat{\boldsymbol{z}} J_z$. After decomposing the 3D system into transversal (α) and axial (β) components, the field lines in a transversal cross section can be represented only with the parameter α:

$$\nabla^2 \alpha = J_z \tag{1.5.3}$$

The value for the magnetic field line indicator α in (1.5.3) can be obtained with Green's function. With this mathematical tool, the thickness of the transformed electron beam can be optimised. This optimisation results in an electron beam much thinner than before, as compared in Fig. 1.5.6 (blue curves denote the optimised beam). Since a thinner electron beam yields higher collector efficiency, for this specific design a simulation with 5 stages shows $86 - 88$ % collector efficiency. The secondary electrons and reflected electrons are totally recollected inside the collector; no electron returns to the mirror box. A collector efficiency of 82 % can thus be achieved even in the presence of secondary electrons.
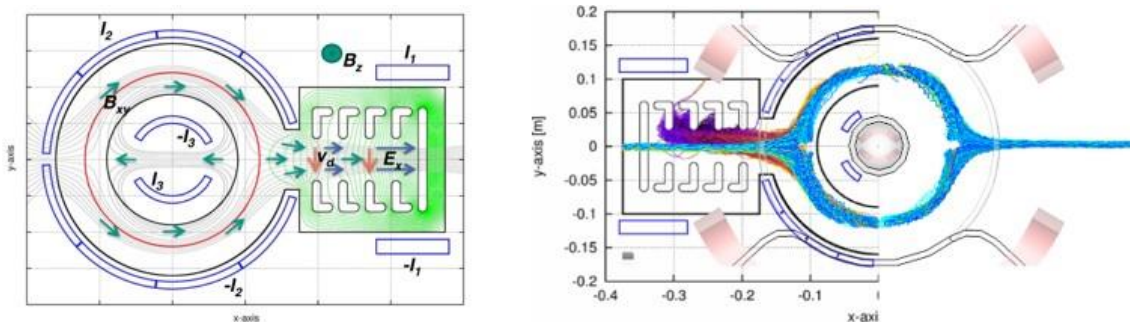
Fig. 1.5.6: Left: The previous E×B concept. Right: Beam thickness before and after optimizations.

Concept with an elongated elliptic electron beam

Another idea to obtain a thin electron beam is to use transversal currents, which refocus the small-orbit annular beam to a thin elliptic beam. The transform is done by four transversal currents, presented in Fig. 1.5.7 as the long edges of each coil. The injected electron beam travels towards the positive *z*-direction. The long edges of the left hand side coil defocus the electron beam only in *y*-direction, whereas the next coil on the right hand side refocuses the beam in *x*-direction. Additionally, ferromagnetic slices can be placed in the coil loops to reduce their current requirement.

Under the condition that no electron will return back to the mirror box the minimal length of the collector i.e., the minimal axial length of the electrodes can be calculated through

$$L > L_{\min} = \frac{2\,\Psi\,q}{\pi\,m_0\,\min\{v_0\}}$$

(1.5.4)

where Ψ is the magnetic flux (converged value) enclosed in the electron beam and v_0 are the initial velocities of the electrons.
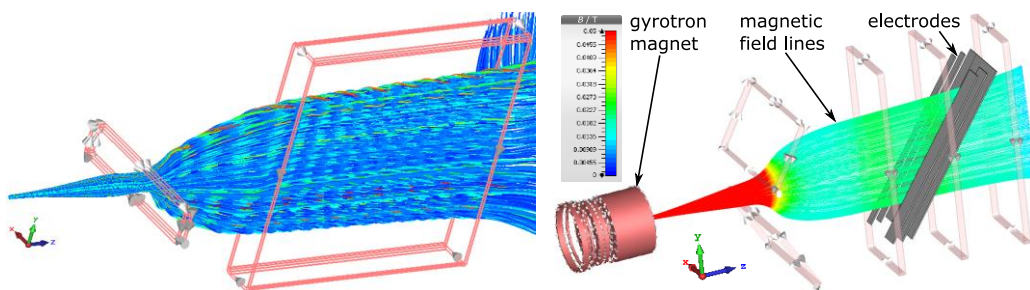
Fig. 1.5.7: Transformation of elliptic beam.

Concept with semi-circle electron beams

An additional idea to obtain thin sheet beams is to sacrifice a small fraction of the electrons. In this way, the hollow electron beam is split into two semi-circular beams, which then can be collected on several pairs of electrodes, where each pair of electrodes has the same depression voltage. Moreover, the shape of electrodes may not be straight like in the previous section. Instead, the edges are adapted to the profile of the electron beams, as shown in Fig. 1.5.8. The required length for this kind of MDC can also be analytically calculated in the way similar to (1.5.4). Splitting the electron beam does not only decrease the MDC length (compared to the full elliptic beam variant), but also improves efficiency, since the split beams are just as thin as the thickness of the cyclotron motion. The efficiency improvement gained from the wafer-thin beam overcomes the energy lost in the sacrificed electrons. A specific simulation of a three-stage collector based on this concept has 76.5 % efficiency, considering secondary electrons and the effects of space charge.
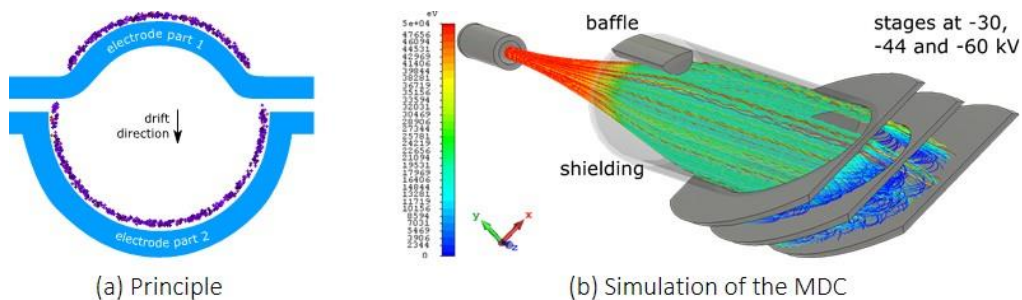
Fig. 1.5.8: Split a circular electron beam to semi-circular sheet beams.

Concept using helical electrodes

Another new concept, which utilises an azimuthal electric field and the longitudinal magnetic field has been considered. This concept does not transform the electron beam to sheet beams, therefore, it has a simpler geometry. It is based on a normal conic single-stage collector. The novel point here is that a helical slot splits the collector into two stages and induces an azimuthal (φ) component of electric field, illustrated in Fig. 1.5.9. The torsion of the helix defines the angle between the electric and magnetic field, and thus it is related to the strength of the $E \times B$ drift.

a) front side view   b) back side view
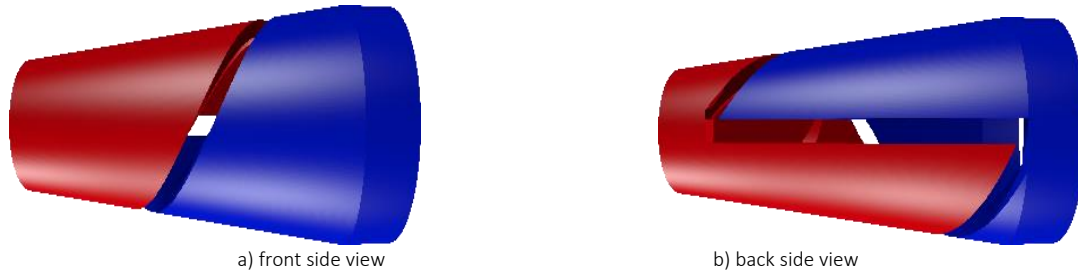
Fig. 1.5.9: Two stages separated by a conical helix slot for the E×B drift.
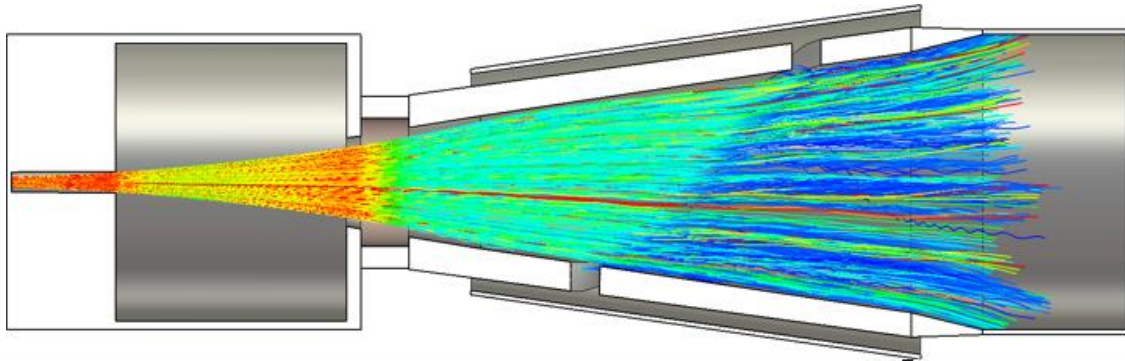
Fig. 1.5.10: Simulation of a two-stage collector with helixal slot.

A special model is simulated, as shown in Fig. 1.5.10. This two-stage collector works like the other $E \times B$ MDCs in such a way that the low-energetic electrons are drifting to the helical slot and impact the first electrode with -30 kV depression, whereas the high-energetic electrons are drifting to the second electrode with -42 kV depression. Taking secondary electrons into account, PIC simulations with CST Particle Studio show an average collector efficiency η_{col} of 77 % (compare to the state-of-the-art single-stage depressed collector η_{col} < 60 %). Secondary electrons only reduce the efficiency by 1 %. There could be less than 1.5 % of the total beam current returned beyond the mirror box (including secondary electrons). The returned current can be reduced by controlling the width of the straight slot connecting both helix ends, which can be further optimised.

1.5.6   Studies towards a 140 GHz 1.5 MW CW gyrotron for W7-X

A preliminary investigation on a possible upgrade of the 140 GHz 1 MW CW gyrotron for W7-X has been performed, with the target to increase the power of the ECRH system of the stellarator. The focus of the research has been on more than one design branches, in order to determine the feasibility of designing a tube with the specified technical goals, while maintaining flexibility with respect to the specific technical realisation. The work focused on mode selection and on preliminary design of the gyrotron cavity and launcher.

To find suitable operating modes for operation at 140 GHz, 1.5 MW, the candidate modes were divided into two categories according to their performance with respect to the ohmic wall loading. In the first category, modes exhibiting ohmic wall loading of the same level as that in the existing 1 MW gyrotron for W7-X (~1.5 kW/cm^2) were considered. This is a conservative approach, based on the experimentally successful performance of the series CW tubes for W7-X. In the second category, modes with ohmic wall loading of the level of that in the EU CW gyrotron for ITER (~2 kW/cm^2) were considered. This is a realistic approach, provided that the performance of the cavity cooling of the ITER gyrotron will be experimentally verified in CW operation. In both categories, the possibility of efficient dual-frequency operation with a second frequency at 175 GHz was also taken into account. After the selection of the best mode out of each category, two cavities were designed and optimised for the respective modes. Finally, for each of these two cavities a quasi-optical launcher was also designed. The best candidate mode from the first category was proven to be the TE$_{28,13}$ mode and the best candidate from the second category was the TE$_{32,9}$ mode. Their simulated performance is summarised in Table 1.5.3.

Table 1.5.3: Operating modes for operation at 140 GHz, 1.5 MW CW.

Modes @ 140 GHz	TE$_{28,13}$	TE$_{32,9}$
Beam voltage	80 kV	80 kV
Beam current	51 A	51 A
Magnetic field	5.57 T	5.57 T
Output power at the cavity	1.69 MW	1.69 MW
Ohmic wall loading	1.56 kW/cm^2	2.14 kW/cm^2
Interaction efficiency	43%	43%
Frequency	140.42 GHz	140.40 GHz

Following this investigation, an additional search for suitable modes was conducted, now with the goal of achieving an upgrade of the existing W7-X gyrotron with a minimum of design changes. The target was set to 1.3-1.5 MW and the requirement for highly efficient dual-frequency operation was relaxed. In order to keep the same electron gun as in the W7-X gyrotron operating in the TE$_{28,8}$ mode, the beam radius was kept the same, which confined the candidate modes to the m = 28 mode series. The candidate modes are given in Table 1.5.4, along with the simulated performance assuming a beam voltage of 80 kV and a typical cavity length of 8 free-space wave lengths. The best choice is the TE$_{28,10}$ mode, which can achieve 1.5 MW and has an eigenvalue which is lower than the one of the TE$_{32,9}$ mode, already successfully excited in the EU gyrotron for ITER. In addition, the TE$_{28,10}$ mode requires a cavity radius which is only 2.3 mm larger than the one of the existing cavity of the TE$_{28,8}$ W7-X gyrotron. Such a small increase can be easily accommodated within the existing cavity design, inducing only minor changes in the cooling structure.

Table 1.5.4: Operating modes in the $m = 28$ mode-series.

Mode	$TE_{28,9}$	$TE_{28,10}$	$TE_{28,11}$	$TE_{28,12}$	$TE_{28,13}$
Eigenvalue	63.6261	67.1036	70.5435	73.9521	77.3344
Cavity radius	21.64 mm	22.82 mm	23.99 mm	25.15 mm	26.3 mm
Beam radius	10.01 mm	10.01 mm	10.01 mm	10.01 mm	10.01 mm
Beam current	48 A	54 A	60 A	67 A	74 A
Output power at cavity	1.45 MW	1.65 MW	1.83 MW	2.17 MW	2.41 MW
Ohmic wall loading	2.10 kW/cm²	2.07 kW/cm²	2.06 kW/cm²	2.08 kW/cm²	2.07 kW/cm²

1.5.7 Studies towards an 60 GHz, 1 MW CW gyrotron for Collective Thomson Scattering applications in ITER

The Collective Thomson Scattering (CTS) diagnostic is crucial for understanding the dynamics of ions in the plasma. From considerations of spatial resolution, plasma access, scattering cross section and current or potential availability of sources, only a few frequencies are relevant. The only CTS system which can meet the ITER measurement requirements is a 60 GHz system. Most demanding for this system is the development of a 1 MW gyrotron at 60 GHz. Additionally to the specifications regarding the frequency and output power, another requirement, related to the spectrum of the electromagnetic wave, is very important: The power in spurious modes within the ±5 GHz range around the central frequency of 60 GHz must be more than 100 dB lower compared to the power at 60 GHz.

A preliminary study on the feasibility of an 60 GHz, 1 MW CW gyrotron for CTS in ITER was performed. Two gyrotron cavity designs were obtained. The operating mode of the first design is the $TE_{18,6}$ mode. Following standard mode-selection procedures that take into account the physical and technical limitations and target at maximisation of the efficieny, this mode was proven to be the best candidate. However, with a required cavity radius of 32.4 mm and an electron beam radius of 15.2 mm, such a gyrotron would be larger than all KIT-related gyrotrons and thus the development of a completely new gyrotron would be necessary for the realisation of the design. The second design was based on the dimensions of the existing 140 GHz gyrotron for the stellarator W7-X to facilitate a possible manufacturing. The operating mode of the second design is the $TE_{12,4}$ mode. With a cavity radius of 20.9 mm and a beam radius of 10.2 mm, the dimensions are close to the radial dimensions of the W7-X gyrotron.

Both cavities were optimised by a parameter study with respect to the cavity length. The cavity length was finally set to 8λ for the $TE_{18,6}$ design and to 7λ for the $TE_{12,4}$ design, where $\lambda = 5$ mm is the free-space wavelength at 60 GHz. In multimode simulations, both designs were found capable of producing 1.1 MW of output power at an operating frequency of 60 GHz without any competing modes excited. The calculated performance is summarised in Table 1.5.5.

Finally, the spectrum of the generated microwave radiation was investigated to check if the gyrotrons meet the challenging CTS requirements regarding the purity of the spectrum. The level of purity of the spectrum was found stable with respect to the operating voltage. The spurious power components in the ±5 GHz range around the central frequency were down to ~95 dB lower than the central spectal line in the simulations. This is in agreement with the high spectral purity required by CTS.

Table 1.5.5: Calculated performance of the two cavity designs.

Operating mode	$TE_{18,6}$	$TE_{12,4}$
Operating frequency	60.069 GHz	60.055 GHz
Output power at cavity	1.097 MW	1.092 MW
Peak ohmic wall loading	0.478 kW/cm^2	0.928 kW/cm^2
Interaction efficiency	43.1 %	42.1 %
Normalised field amplitude, F	0.159	0.208
Normalised interaction length, μ	12.870	11.499
Normalised detuning parameter, Δ	0.574	0.645

1.6 FULGOR (Fusion Long-Pulse Gyrotron Laboratory)

The existing gyrotron test facility at KIT, which had been designed and built about 30 years ago, plays a worldwide leading role in the development of high-power gyrotrons for nuclear fusion applications. This facility offered the unique opportunity to develop and test the first CW high power series gyrotrons for the stellarator W7-X in collaboration with IPP and Thales Electron Devices as the industrial partner.

The target parameters of the new gyrotron test facility are well beyond the capabilities of the existing one. The new test stand will strongly support KIT's leading role in the development of advanced gyrotrons. It will help to answer the questions regarding the technical limits and new physical designs for future high-power microwave tubes. The key parameters of FULGOR will be:

- Full CW operation with up to 10 MW electrical power
  (corresponding to >= 4 MW RF power (assuming an efficiency of the gyrotron >= 40 %)
- Support of advanced energy recovery concepts, e.g. multi-stage depressed collector (MSDC)

The high voltage power supply (HVPS) will support an operating voltage of up to 130 kV with up to 120 A beam current in short pulse operation and 90 kV / 120 A in continues wave regime. A superconducting magnet which allows operation of gyrotrons at frequencies well above 200 GHz will be a major component of FULGOR. Other significant components of the teststand will be: cooling system, control electronics and interlock system, RF diagnostics including high-power RF absorber loads.

The capabilities of FULGOR will enable the development and CW tests of gyrotrons for future fusion machines like ITER and DEMO. Fig. 1.6.1 is a simplified CAD view of the complete FULGOR system.

Fig. 1.6.1: CAD view of FULGOR installation including control room.

Substantial progress has been achieved in the planning, procurement and installation of major systems of the new test stand.

High Voltage Power Supply (HV PS): In 2016 the final design details of the HV PS have been discussed and agreed with the supplier (Ampegon, Switzerland (CH)). The production of components has been started and the installation of major elements has been performed (see Fig. 1.6.2 and Fig. 1.6.3). The production of the sub-assemblies of the EPSM power modules (84 in total) for CW operation has been started and first electrical and mechanical tests show a proper behavior. The procurement of components and the production of the Pulsed Power System modules (PPS modules) (40 in total) for up to 5 ms operation have been started.

Fig. 1.6.2: Left: Two 6.5 MVA transformer installed at FULGOR hall. Right: Ventilation cabin and rack for electronic modules.
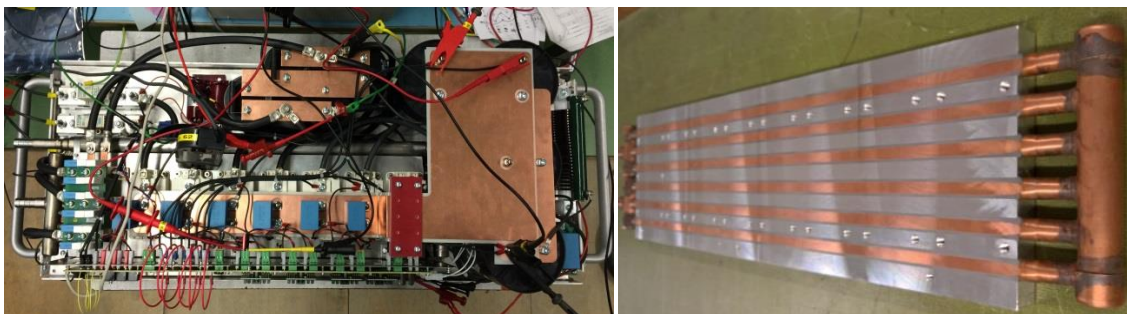
Fig. 1.6.3. Power module and cooling unit.

Cooling system: The cooling system is designed for full 10 MW operation. However, in the first step only a first single tower with a cooling power of 5 MW was installed (see Fig. 1.8.4), with the option to add a similar second tower at a later stage for full 10 MW CW cooling capacity. All pumps, piping, instrumentation and control has been installed, partially tested and accepted.

Control and data acquisition: The strategy for control of the HVPS has been discussed and decided with the supplier (Ampegon). Several components of industrial standard Siemens S7 have been procured and implemented. First components of a fast interlock system to limit the energy deposition in the tube in case of malfunction, fast data acquisition to record events occurring on a µs timescale and visualisation have been implemented and tested.

Superconducting magnet: This is the most challenging component of the FULGOR project since the requirements are far beyond what is the today's industrial standard. In particular, a large borehole diameter (min. 240 mm (target: 270 mm)) in combination with a high magnetic field requirement (up to 10.5 T to ensure gyrotron operation up to 240 GHz) calls for a very clever design of the magnet. In 2016 intense discussions with several industrial supplier took place in order to clarify technical solutions and to come to realistic specifications.

Fig. 1.6.4. 5 MW cooling tower (left) and cooling pipes in FULGOR hall (right).

Involved Staff:

KIT/IHM: K. Avramidis, J. Franck, M. Fuchs, **Dr. G. Gantenbein, Dr. S. Illy**, Dr. Z. Ioannidis, Prof. J. Jelonnek, Dr. J. Jin, Th. Kobarg, R. Lang, W. Leonhardt, M. Losert, D. Mellein, A. Meier (KIT, IAM-AWP), Dr. I. Pagonakis, A. Papenfuß, K. Parth, S. Ruess (KIT CS), **Dr. T. Rzesnicki**, Prof. Dr. Theo A. Scherer (KIT, IAM-AWP), M. Schmid, W. Spiess, Dr. D. Strauss (KIT, IAW-AWP), Prof. M. Thumm, S. Wadle, J. Weggen, Ch. Wu, A. Zein, J. Zhang, **IGVP (University of Stuttgart): Dr. W. Kasparek**, Dr. C. Lechte, R. Munk, Dr. B. Plaum, F. Remppel, H. Röhlinger, B. Roth, K.H. Schlüter, S. Wolf, A. Zeitler, **IPP (Greifswald/Garching):** B. Berndt, Dr. H. Braune, F. Hollmann, L. Jonitz, **Dr. H. Laqua**, Dr. S. Marsen, F. Noke, M. Preynas, F. Purps, A. Reintrog, T. Schulz, T. Stange, P. Uhren, M. Weißgerber, F. Wilde

2 Renewable Energy (RE): Bioenergy
– Feedstocks and Pretreatment –

2.1 Overview

In the area of PEF-assisted microalgae downstream processing, it could be shown that parasitic microalgae precipitation is controlled by the cell's zeta potential. Appropriate adjustment of the zeta potential and the application of short pulses of several microseconds and shorter can impede unwanted biomass deposition at the electrodes of the treatment chamber.

Protocols for lipid extraction from wet microalgae biomass were optimized for recovery rates of up to 97 % of the lipid inventory. Preceding analysis of various reference methods for absolute lipid content determination revealed, that Soxhlet extraction with Hexane is the most suited method.

Investigations on basic effects of nsPEF stress responses demonstrated, that nsPEF treatment at non-lethal doses can arrest cell cycle and cause pamella states due to oxidative bursts.

Optimization of cultivation strategy reduced microalgae suspension conductivity by a factor of more than 3, which is an important step for further improving energy-efficiency of PEF-assisted microalgae processing.

Efforts to elevate PEF-processing to a new technology platform of operator-friendly semiconductor (SC) based pulsed power generators has been approached. The use of a power SC as pulse switches allows for significantly higher pulse repetition rates at moderate voltage levels at a given specific processing energy. Hence, generator size can be reduced accordingly. Currently, a 30-stage pulse generator with 30 kV rated output voltage and 600 A peak pulse current has been set up.

2.2 Control of microalgae precipitation on electrode surfaces during Pulsed Electric Field (PEF) treatment by adjustment of suspension pH

PEF treatment of microalgae has been demonstrated to exhibit processing advantages compared to conventional processing. Besides low specific energy requirements, PEF treatment can separate microalgae biomass into aqueous and oleaginous fractions. To minimize processing energy demand, the treatment of pre-concentrated microalgae suspensions is advantageous. The use of concentrated microalgae suspensions resulted in precipitation at the electrodes of cross-linear treatment chambers. Reduction of the pulse duration appeared to reduce precipitation during PEF treatment significant. Furthermore, examination of this precipitation effect revealed a correlation between precipitation behavior of different microalgae species, e.g. *Chlorella vulgaris* and *Auxenochlorella prototothecoides*, and zeta potential Fig. 2.2.1. A closer inspection demonstrated that precipitation behavior of different microalgae species depends on pH of the suspension. As a result, pH-control appeared to be a suitable tool for further reduction of microalgae precipitation on electrode surfaces.

2.2.1   Zeta potential and its impact on microalgae precipitation on electrode surfaces

It is known from literature, that the zeta potential of most microalgae is negative and for that reason, we suspected that this might be a reason for predominant precipitation of algae on the anode surface. Fig. 2.2.1 displays the correlation between zeta potential and algae precipitation for two algae strains: *A. protothecoides*, and *C. vulgaris*. Both algae strains were processed with identical PEF treatment parameters (specific treatment energy, w = 50 kJ/kg; pulse duration, T = 200 µs; electric field strength, E = 5 kV/cm). Fig. 2.2.1 shows that *C. vulgaris,* which exhibits a lower zeta potential in terms of absolute values, results in a smaller amount of biomass precipitated at the anode. Consequently, precipitation of *A. protothecoides* was higher.
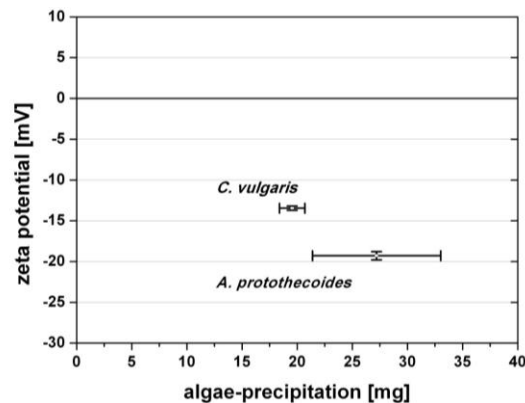
Fig. 2.2.1: Influence of the microalgae species on zeta potential and microalgae precipitation. Experiments were performed with 75 mL of algae suspension treated with 200 µs-pulses and an electric-field magnitude of 5 kV/m. Specific energy was adjusted at 50 kJ/kg and the flow of the suspension through the treatment chamber at 0.10 mL/s. Results are mean ± SD of two independent experiments for C. vulgaris, and six independent experiments for A. protothecoides.

2.2.2   Suspension-pH influences the zeta potential of microalgae

In order to confirm the link between zeta potential and precipitation, the zeta potential of *A. protothecoides* was modified by adjusting the pH of the suspension. Fig. 2.2.2 displays the results of a pH-titration experiment performed on *A. protothecoides* suspended in a Wu-cultivation medium. It shows the development of the zeta potential, as a function of pH, which was adjusted by addition of an increasing amount of 1 M MES (2-(*N*-morpholino)ethanesulfonic acid) solution. The results indicate that decreasing pH in *A. protothecoides* suspension induces a reduction of the absolute zeta potential value. In Fig. 2.2.2, the upper and lower limits of flocculation are shown. Within these limits, flocculation is expected and beyond these limits algae suspensions remain stable.
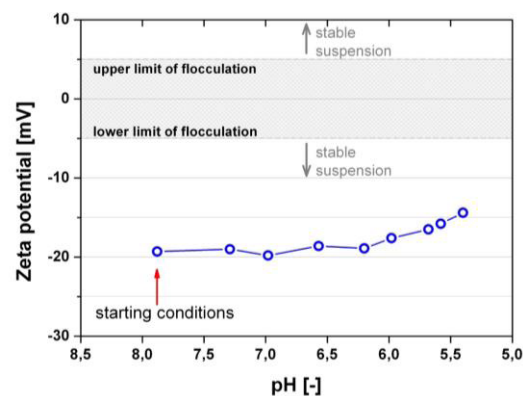
Fig. 2.2.2: Impact of pH on zeta potential of *A. protothecoides*. The pH reduction was obtained by addition of increasing quantities of 1 M MES. The upper and lower limits, where flocculation is expected are drawn.

2.2.3 Precipitation control by pH-adjustment

This result therefore supports the hypothesis that zeta potential is a major factor, influencing the quantity of microalgae that precipitates. In order to confirm the link between zeta potential and precipitation, the zeta potential of *A. protothecoides* was modified by adjusting the pH of the suspension, since the strong link between pH and zeta potential is known from the literature. To verify the impact of pH on algae precipitation by PEF processing, experiments were conducted with *A. protothecoides* either at its natural pH i.e. 7.6 or at reduced pH, i.e. 5.7. The pH-drop decreased the absolute zeta potential by 3.17 mV. Amounts of precipitated microalgae after PEF treatment (W_{spec} =50 kJ/kg, t_{Imp} = 200 µs, E = 5 kV/cm, Q = 0.10 mL/s) are displayed in Fig. 2.2.3 for the two zeta potential values. As to be seen in the Figure, the reduction of the absolute zeta potential results in a significant reduction of microalgae precipitation on the anode surface, of 17.3 mg, i.e. by more than 50 %.
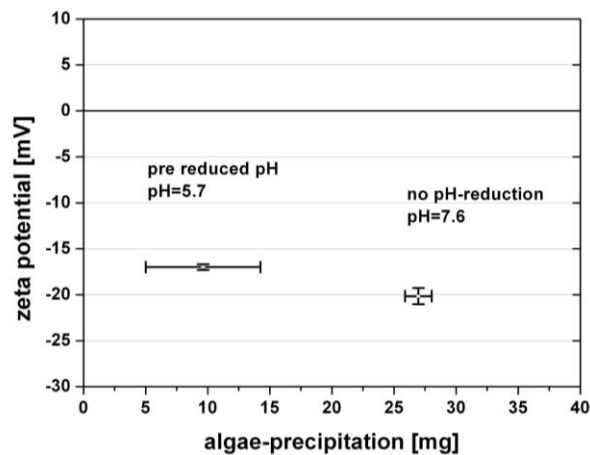
Fig. 2.2.3: Modification of zeta potential by pH reduction and consequences on microalgae precipitation. Experiments were performed with 75 mL of algae suspension (*A. protothecoides*), treated with 200 µs-pulses and an electric field magnitude of 5 kV/cm. Specific energy was adjusted at 50 kJ/kg and the flow of the suspension through the treatment chamber at 0.10 mL/s. Results are mean ± SD of three samples in two independent experiments.

2.3 Optimization of lipid extraction from wet microalgae biomass

In previous work of the bioelectric group, it was shown that Pulsed electric field (PEF) treatment was an efficient technique to permeabilize external membranes of microalgae. This was previously demonstrated by quantification of spontaneous release of intra-cellular ions and of small carbohydrate. Additionally, it was shown that PEF pre-treatment combined with solvent extraction could greatly enhanced lipid yields. During the last year, the work program has been focused on the improvement of the lipid extraction to improve quality of solvents and to analyze the extracted oil. Focus has been set on the microalgae *Auxenochlorella prototecoides* (AP) for which our group has good expertise in the cultivation.

2.3.4 Establishment of reference methods

The first working task of this project consisted in the establishment of a reference method to analyze total lipid content of the cultivated microalgae. Three of the most popular reference methods were tested on freeze-dried microalgae: a standard method based on chloroform and methanol extraction i.e. Bligh and Dyer, a method based on methanol and methyl-tert-butyl ether (MTBE), and Soxhlet extraction using Hexane as extraction solvent.

All three methods were tested on freeze-dried microalgae, eventually additionally pre-processed with bead-milling. Results are presented on Fig. 2.3.1. From the lipid yield obtained, it appears that the Bligh and Dyer method failed to extract any lipids with or without bead-milling. Additionally, it appears that Bead-milling was necessary for efficient extraction for both Soxhlet and MTBE which is of high relevance considering that in the literature all three methods are very often used without any bead-milling. This might imply that AP microalgae are perhaps more resistant to extraction and they require an intense pre-treatment process. Based on the obtained results, Soxhlet extraction has been chosen as the reference method employed in the bioelectric group since it was more efficient with higher lipid yields and could be easily automated, leaving less room for human errors.
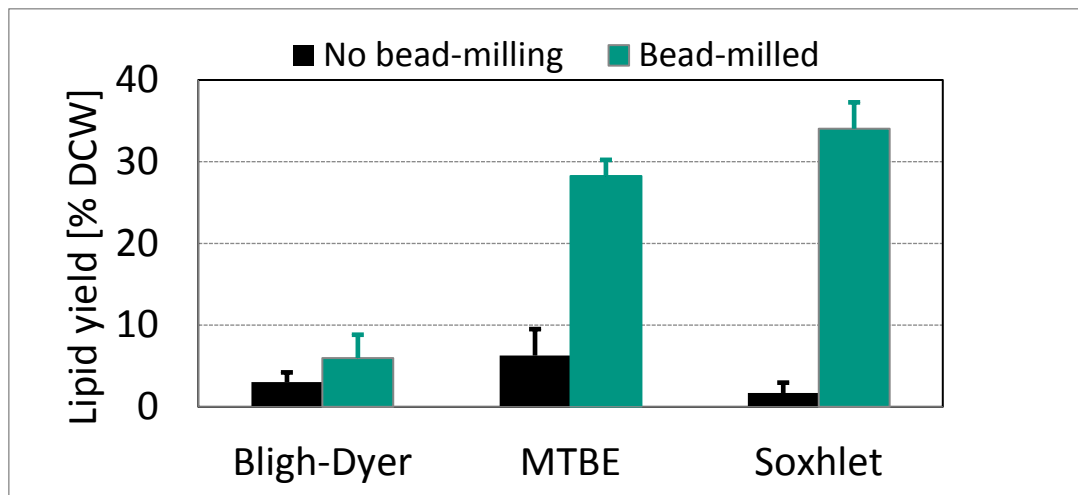
Fig. 2.3.1: Comparison of the extraction yields of three reference extraction methods: Bligh and Dyer, MTBE and Soxhlet. Extraction were performed with and without bead-milling. Blocks are the average values plus standard deviation of at least three independent extractions.

2.3.5   Extraction of lipids after PEF treatment

A standard protocol was used to process the fresh microalgae. In consisted in concentrating them at $100 g/kg_{sus}$ by centrifugation directly after harvesting and then treating them with PEF in a continuous flow mode. Electric parameters were chosen based on previous work of our group and consisted in 1 µs pulses with an electric field intensity at 4 MV/m applied with a repetition rate at 3 Hz. All experiments were performed with an energy input adjusted to 150 kJ per liter of suspension i.e. approximately 1.5 MJ per kg of algae dry mass.

Sham treatment consisted in submitting the sample to the flow through the treatment chamber but without any PEF treatment. After treatment, microalgae were observed under the microscope. The observation did not reveal any major change of morphology of the microalgae. The general shape and size were maintained and no debris was to be observed. In order to validate the efficiency of PEF treatment, the microalgae suspension was centrifuged after the treatment and the conductivity of the supernatant was measured. Supernatant of control samples had a conductivity of around 1.6 mS/cm at room temperature due to the ionic compounds of microalgae cultivation medium. After PEF treatment, conductivity increased by about a factor 2 and reached a value of approximately 3 mS/cm due to the release of the microalgae's intracellular ionic content. The doubling of supernatant conductivity therefore validated the efficiency of the chosen parameters for PEF treatment.

A lipid extraction protocol, inspired from Molina et. al., was adapted to be functional on wet microalgae. It is based on a hexane ethanol extraction. Results obtained with gravimetric method for different duration

of extraction are displayed on Fig. 2.3.2. The absolute lipid content of the microalgae was determined by Soxhlet and is also displayed in the Figure. The results show that the extraction procedure was inefficient for untreated microalgae and lipid yields always ranged between 1 and 4 %. PEF treatment had an outstanding effect on the extraction. The lipid yield after only one hour of extraction was on average 31 % of dry weight and therefore very close to the absolute lipid content of 37 %. The yield was further increased after 20h of extraction and reached 36 % of dry cell weight (CDW), i.e about 97% of the total lipid content.
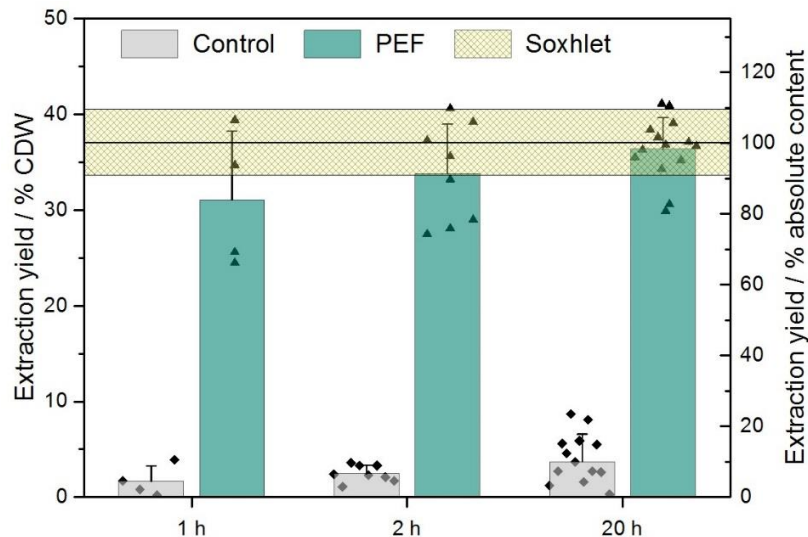
Fig. 2.3.2: Influence of PEF treatment on lipid yields obtained with solvent extraction for different extraction durations. Bars show the average plus standard deviation of at least three independent experiments. Markers show individual data points. The straight lines indicate the average plus/minus standard deviation of Soxhlet extractions. Results were obtained from mixotrophically grown microalgae *Auxenochlorella protothecoides*.

The completeness of lipid extraction could be further confirmed by using the fluorescence dye Nile-Red which stains lipids. While control samples still displayed a strong fluorescence signal indicating the presence of lipids inside the cells, the samples treated with PEF prior to extraction displayed only a very weak remaining fluorescence signal therefore confirming that the complete inventory of lipids was extracted. Currently, gas-chromatography analyses are ongoing in order to analyze the composition of the extracted oil. Preliminary analysis shows no impact of PEF-treatment on extract quality.

2.4 Nanosecond pulsed electric fields (nsPEF) trigger cell differentiation in *Chlamydomonas reinhardtii*

There are several evidences that support the basic concept of using algae as an alternative and renewable source of biomass feedstock for biofuels and/or food production. These include: high productivity per footprint, non-food based feedstock resources, use of non-arable land, reduced water demand, production of valuable co-products, etc. Due to the fast growth rate and the ability to convert light into valuable products, such as lipids, proteins and antioxidants, microalgae provide a biomass which found several applications in food, energy and pharmaceutical production. While these aspects were intensively investigated, a sustainable and economic system for algae cultivation has to be developed.

Besides the reduction of investment and operational costs of photobioreactors the increase of biomass yield, by an increased cell density or accelerated cell growth might be an alternative strategy. In previous studies, it was shown that nanosecond pulsed electric fields (nsPEF) treatment of *Arabidopsis thaliana*

seedlings and mushroom spores, results in an accelerated growth and thus to an increased yield of fruit bodies, in case of mushrooms. Nevertheless, in the efforts to stimulate algal growth by means of nsPEF treatment these effects were contradictory. In order to clarify this contradiction, basic investigations on signaling pathways for nsPEF induced stress reactions of microalgae have been study in the frame of a doctoral thesis. In general, plants, including microalgae, perceive environmental signals (abiotic and biotic stress) and further them to cellular machinery to activate adaptive responses.

In this study the unicellular green algae *Chlamydomonas reinhardtii* was used as experimental model to analyze the cellular responses evoked by nsPEFs. It could be observed that nsPEFs induce a short-term permeabilization of the membrane, accompanied by swelling and oxidative bursts. Furthermore, these responses were enhanced when the pulse duration increased from 25 ns to 50 ns. These responses are transient, but are followed, several days later, by a second wave of oxidative bursts, arrested cell division, stimulated cell expansion and the formation of an immobile palmella stage, Fig. 2.4.1. Both the stimulation of cell expansion and the formation of palmella stages, correlate with a persistent long-term increasing of lipid peroxidation. While the spontaneous formation of palmella stages could be suppressed by exogenous indol acetic acid (IAA), the palmella formation in response to nsPEFs was not responsive to exogenous auxin. Our data show that nsPEFs release a long-lasting signal that persists, although the immediate cellular changes to the treatment are mostly reversed in the first two hours after pulsing.
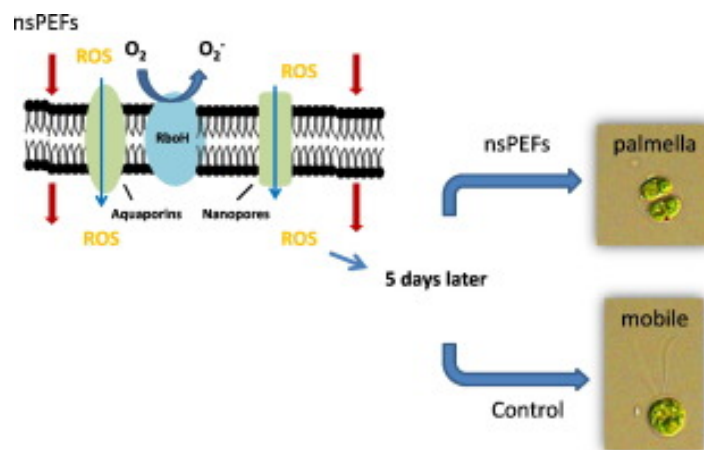
Fig. 2.4.1: Induction of palmella stage in response to pulse treatment. Representative cells after nsPEFs treatment. [Bai et al. BBA Biomembranes 2017, 5:1859].

The highlights of this study are:

- nsPEFs induce rapid membrane permeability, volume increase and lipid peroxidation,
- Cell responses to nsPEFs enhanced when pulse duration increased from 25 ns to 50 ns,
- Cell cycle arrested and palmella stages appeared during long-term response to nsPEFs,
- nsPEFs induced irreversible palmella stages could not be suppressed by exogenous IAA.

2.5 Bacterial decontamination of industrial water and paints by means of pulsed electric fields (DiWaL –Project)

In the framework of three-year project, focus on the "Decontamination of Industrial Water and Paints" DiWaL, a consortium of research institutions and manufacturers, under the coordination of KIT, has started the work on November 2016. DiWaL is funded by the Federal Ministry of Education and Research (BMBF), and has a total budget of 2.9 million euros. The main objective of the project DiWaL, is to develop innovative water-management solutions and enhanced designs for pretreatment and electrocoating systems, by employing the PEF technology, in order to improve the efficiency and the sustainability. The aim of this concept is to prevent the bacterial contamination in the pretreatment and coating process in order to eliminate the use of biocides and to reduce both fresh water consumption and waste water generation.

DiWaL bundles the experiences of partners from research, Karlsruhe Institute of Technology (KIT) and Pforzheim University of Applied Sciences, as well as production-system specialist Eisenmann SE, paint manufacturers Emil Frei and PPG Deutschland, PPG Deutschland Business Support GmbH and carmaker BMW Group. The joint project to improve decontamination of industrial water and paints commenced on November 1, 2016 and will conclude on October 31, 2019.

2.6 Microalgae cultivation for low suspension conductivity during biomass harvest

The energy demand for PEF treatment in microalgae downstream processing scales with the conductivity of the suspension to be processed. In order to avoid additional energy-extensive washing steps, a low conductivity value of the microalgae suspension of 1 mS/cm and lower at the end of the cultivation is desired. Recent values achieved at the outdoor photobioreactor ranged between 3 mS/cm and 4 mS/cm, when operated without conductivity-optimized control algorithms.

In 2016 headed by BVT cultivation media and conditions were optimized on lab-scale for low-conductivity at the end of the cultivation.

Based on ICP-OES analyses the medium components were adjusted according to the elemental composition of Chlorella vulgaris for a final cell dry weight of 5 g/L.

In previous outdoor cultivations the pH was adjusted by NaOH titration until the medium was saturated with CO_2. Due to Na+-ions of the titration solution and a medium composition which was not tailored to the needs of the algae the conductivity of the suspension unnecessarily increased.

Cultivation with optimized control parameters and medium was carried out in a 1.7 L stirred tank reactor with continuous illumination. After cultivation time of approx. 140 h a cell dry weight of 5 g/L at a conductivity of less than 1 mS/cm was achieved. In the upcoming year this approach will be implemented and tested for feasibility at the outdoor flat panel photobioreactor "pbr1000".
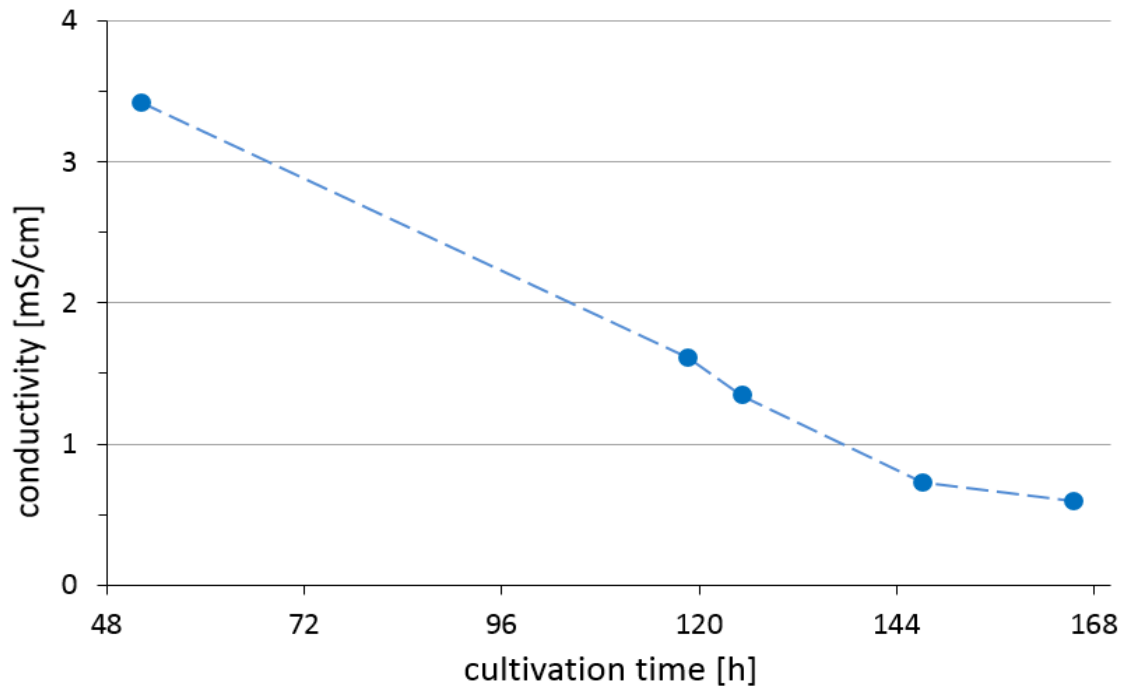
Fig. 2.6.1: Change of suspension conductivity during a batch cultivation of C. vulgaris in a stirred tank reactor with optimized medium composition and improved control algorithms.

2.7 Electroporation of crushed grapes and development of semiconductor based generators

In cooperation with the University of Otago, New Zealand, the electroporation device KEA-WEIN has been operated on-site in a winery in New Zealand in March and April 2016. Appoximately 2 t of Merlot grapes have been processed successfully. The goal of the trials was to combine electroporation with the method of fermentation on skins, which is the common processing method for grapes of red grape varieties in New Zealand. Chemical and sensorial analysis of must and wine has been performed by Prof. Oey and her colleagues from the University of Otago.

Fig. 2.7.1: Electroporation device KEA-WEIN on site in a winery in autumn 2016.

In the frame of a joint cooperation between ARMBRUSTER Keltereitechnologie, KEA-TEC, the State Institute for Viticulture and Enology, Freiburg, and KIT/IHM the technology of the electroporation of crushed grapes is currently transferred to industrial partners. This work is supported by the Federal Ministry for Economic Affairs and Energy on the basis of a decision by the German Bundestag. For the experiments in autumn 2016 the electroporation device KEA-WEIN has been upgraded to a flowrate of 2 t/h. Fig. 2.7.1 shows the electroporation device set up in a winery. The increase in flow rate has been achieved by combining a scale-up of the electroporation reactor with an increase in flow velocity. Scaling allows for an easy adaptation in size of an already existing design for an electroporation reactor without the need for field calculations. The electrode distance has been increased from originally 35 mm to 44 mm, which corresponds to an increase in tube diameter from DN40 to DN50. In combination with the existing Marx generator and power supply the new design allows for a peak electric field strength inside the electroporation reactor of $\hat{E}$ = 44 kV/cm and a strongly damped periodic pulse shape. For a higher flow rate of crushed grapes the pulse repetition rate of the Marx generator has been increased by implementing a nozzle for each spark gap switch. The nozzles guide the flow of nitrogen gas inside the spark gap housing directly to the gaps between the electrodes and hence provide a fast removal of debris. At a charging voltage per stage of 50 kV a pulse repetition rate of 39 Hz has been achieved. Fig. 9 shows the charging voltage per stage. As the power supply uses a control scheme based on pulse packets, the voltage increases stepwise. During the experiments in autumn 2016 in a winery crushed grapes of four different grape varieties (Riesling, Mueller-Thurgau, pinot noir and Zweigelt) have been processed succesfully. The wine is currently processed.

Fig. 2.7.2: Charging voltage of one stage of the Marx generator.

For the use in a PEF treatment device pulse circuits based on a series connection of capacitor, inductance, and the resistance of a PEF treatment reactor (RLC circuit) are well established for large-scale devices equipped with spark gap switches. However, the combination of such a RLC-based pulse circuit with a semiconductor-equipped Marx generator enables energy-efficient soft switching of the semiconductor switches. In last year's annual report a ten-stage Marx generator according to this design concept has already been presented. Now, a 30-stage Marx generator with IGBT switches has been developped and tested successfully. For the tests the stages have been arranged in three stacks of ten stages each (Fig. 2.7.3).

Fig. 2.7.3: Pulse generator comprising 30 modules.

The generator has been designed for a stage voltage of 1 kV. The charging path comprises current-compensated charging coils allowing for a simple single-switch design of each stage and low voltage drop during charging. The pulse generator has been tested in a circuit with an inductance L = 70 µH and a load resistance of R = 37.5 Ω. Fig. 2.7.4 shows the voltages measured at the outputs of stages #10, #20, and #30 together with the current through the load resistance. The fast voltage rise in combination with the rather slow rise of the current demonstrates the zero-current switching condition during switch-on. The switches open after complete discharge of the capacitors. In case of a flash-over at the load shorting the electrode system of the electroporation reactor immediate opening of the switches is desired to limit the energy fed into the ark. However, when opening the switches during pulse application the circuit inductance continues to drive a current. To enable a fast decay of the current the stages have been equipped with a circuitry for active voltage clamping instead of using bypass diodes. Fig. 2.7.5 shows the voltages at each stage and the load current for a three-stage configuration during active clamping. Equal voltage distribution between the stages has been achieved both during pulse application and voltage clamping. Under clamping conditions the current decays nearly linearly down to zero. The energy is transferred partly back into the stage capacitors and partly dissipates into heat at the IGBT switches.
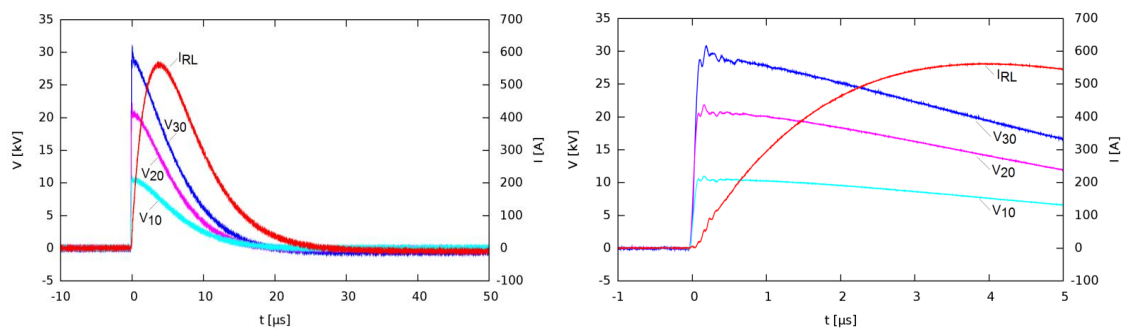
Fig. 2.7.4: Test of 30-stage generator at 1 kV per stage (L = 70 µH, RL = 37.5 Ω): Voltage at stages 10, 20, and 30 (V10, V20, V30), and current through load (IRL): left:whole pulse, and right: voltage- and current rise.
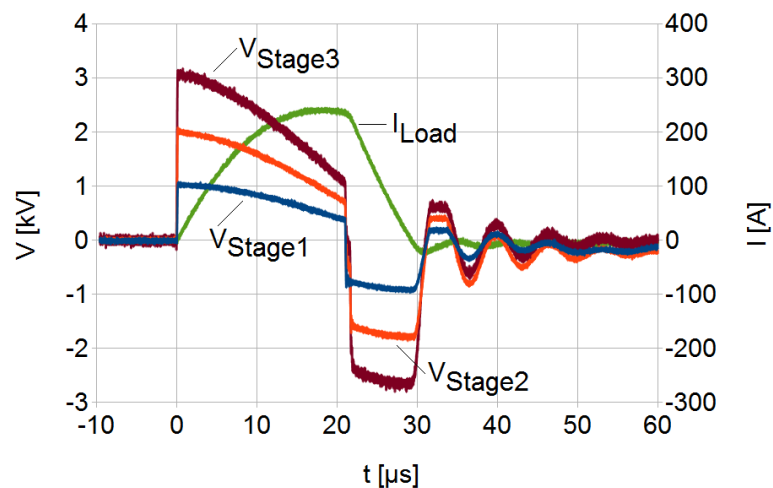
Fig. 2.7.5: Active clamping in a 3-stage configuration: Equal voltage distribution between stages.

Involved Staff:

K. Baumann, H. Brüsemeister, J. Fleig, **Dr. W. Frey**, Dr. C. Gusbeth, D. Herzog, M. Hochberg, S. Keipert, K. Leber, Prof. G. Müller, K. Paulus, D. Quattrocchi, **Dr. habil. M. Sack**, Frau Dr. A. Silve, DI R. Sträßner, R. Wüstner

2.8 Concentrating solar power (CSP)/ Liquid metal – Material research – improving the compatibility of materials for CSP

The use of liquid metals as heat-transfer- and storage media for CSP is a new research area started in the frame of POF3 together with IKET, INR and IAM. The basis of this work including experimental capabilities is funded on the experience and expertise gained in the last years on research performed in the nuclear program. Based on fundamental aspects of material liquid metal compatibility material concepts and related experimental are the major target of our research. Surface modification of materials using pulsed electron beams is well established in the nuclear community dealing with the use of liquid metal coolants. In-situ diagnostics of beam formation and target beam interaction will be targeted combining a new constructed GESA – SOFIE and simulations using MAGIC and other software tools. In addition to Na, Pb, Pb-alloys and Sn are investigated as possible CSP heat transfer materials. In the past extensive investigations regarding material compatibility with these liquid metals (especially with Pb and Pb-alloys) were done, but mainly below 550°C. The available corrosion test facilities (COSTA) for Pb, Pb alloys and Sn ca be operated also at temperatures above 600°C, which is the temperature range required for being used in CSP devices.

2.8.1 Development of material concepts for the use of liquid metals at high temperatures

Design and construction of Na corrosion test facilities for CSP tower receivers

The most promising liquid metal to be employed as heat transfer media in CSP tower receivers is liquid Na. Na was already used in the past for this purpose, but some Na fire stopped all activities in that direction. Therefore, all materials that are intended to be used have to be fully compatible with Na and no stress induced failure is allowed. Most steels are corrosion resistant at least up to 650°C in oxygen free Na. For

efficient use of CSP the final target is to operate the receiver at temperatures above 750°C. To assure the use of steels and Ni-based alloys and surface modified materials corrosion test in stagnant Na are envisaged. The day and night cycle and the occurrence of clouds induce stresses in the materials. Rapid temperature changes at high temperatures will be simulated by a dedicated test facility. Two temperature ranges are considered to be of interest. For short term realization of Na as CSP heat transfer media HT-steels without and with surface engineering (alloying with non-soluble materials or Al including pre-oxidation) will be tested at temperatures below 700°C. For long term perspective higher temperatures up to T_{boil} of 883°C are the target. There Ni base alloys with and without surface engineering, Ceramics, Maxphases or new concepts like WCu-laminated tubes will be considered.

Compared to experiments performed with Pb alloys in the past Na requires significant improved safety measures that assure to avoid any contact of Na at high temperatures with water and air. Therefore, a new Na-Corrosion lab containing a COSTA-SOL for corrosion tests in stagnant Na at temperatures up to 880°C and a high temperature thermal cycling loop SOLTEC-TCT (700°C + 880°C) was established.

The COSTA facility COSTA-SOL for Na was build, attached to the glovebox and taken into operation. The Na-melting pot was installed in the glovebox and first Na handling efforts were performed (Fig. 2.8.1). Oxygen and moisture content in the glovebox are still too high for handling oxygen free sodium. Therefore, an oxygen and moisture control loop is designed and will be attached to the glovebox. Anyway, to reduce further the oxygen and moisture content in the glovebox an additional heated stainless steel pot containing Na or Li at elevated temperature will be placed in the glovebox. This open liquid metal will be used to reduce the remaining oxygen and moisture before handling the Na. In a first test at 600°C Na was filled in an alumina crucible and placed inside the stainless steel tube of the furnace. To reduce the oxygen content of the Ar+5%H2 gas that is purged during the exposure experiment even more, the gas passes an additional furnace at around 650°C via a steel tube filled with Zr metal wire.

The design of the high temperature thermal cycling loop SOLTEC-TCT consisting of two parts, the loop and the thermal cycling test (TCT) section was already described. The SOLTEC-TCT, whose final design is shown in Fig. 2.8.2, is under construction, finally. The TCT section is ready to be adapted to the loop.

Fig. 2.8.1: Na heating and filling pot located in glovebox.
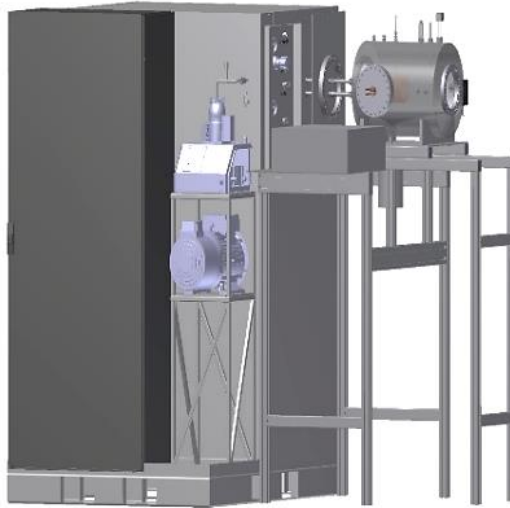
Fig. 2.8.2: Sketch of SOLTEC-TCT loop and thermal cycling test section.

High temperature compatibility test of steels and commercial FeCrAl materials in Pb

Beside Na, Pb is still an option as heat transfer fluid in. The SOMMER (Solar furnace with Molten Metal REceiver) facility, designed and build by our colleagues from IKET, will use Pb as heat transfer media with a maximum temperature of about 650 °C. The first version of the receiver will be built from stainless steel. To explore possible construction materials exposure tests performed some time ago with two steels,1.5471 and alloy 800, and alumina containing Fe-base alloys from Kanthal performed at 600 and 750 °C in Pb with an oxygen content of 10^{-6} and 10^{-8} wt% for a duration of 1000 h were re-evaluated. The steel 1.4571 do not exhibit any corrosion attack at 600 °C, while the alloy 800 exhibit dissolution corrosion at the lower oxygen conditions. All tested Kanthal alloys show excellent behaviour even at 750°C in Pb with 10^{-6} wt% oxygen. Thin Al_2O_3 scales develop at the surface and protect the materials. The alloy 800 shows locally dissolution attack that alter with Cr enrichment at the surface accompanied by deep internal oxidation. The austenitic steel 1.4571 forms a Fe rich outer Fe-Cr scale with an internal oxidation zone of about 100 µm. Some Pb penetrated the Fe-Cr scale but not resulting in sever dissolution attack, at least after 1000 h of exposure. At 750 °C in Pb with low oxygen (10^{-8} wt%) however, only one FeCrAl-alloy survived (Fig. 2.8.3), the Kanthal Akrothal with 15Cr and 4 wt% Al. A thin almost non visible oxide scale prevents the dissolution attack. All other Kanthal alloys with higher Cr content as well as the two steels (alloy 800, 1.4571) showed severe dissolution attack (Fig. 2.8.3).
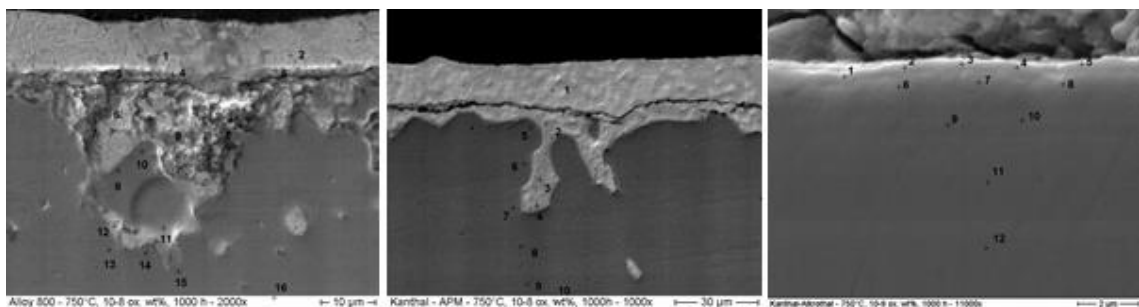
Fig. 2.8.3: SEM of cross sections of (from left to right) alloy 800, Kanthal APM and Kanthal Aktrothal after 1000h exposure to Pb at 750°C with 10^{-8} wt% oxygen.

Whether the Kanthal Akrothal as the best behaving of these materials can be employed for use in CSP even at 750°C with Pb as heat transfer media requires longer exposure tests at similar conditions. However, for

65

SOMMER, the Pb cooled KIT CSP Demonstrator, both steels and all the Kanthal alloys can be used at least for short term operation of 1000 h.

Alumina-forming high entropy alloys

High-entropy alloys constitute currently an important scientific topic for materials researchers and engineers due to their unique and even intriguing compositions, microstructures and engineering properties, such as high strength and toughness, creep and corrosion resistance.

Containing five or more principal elements (concentrations of each element ranging from 5 to 35 at. %), in contrast with the conventional metallurgical alloy-design, they form disordered solid solutions with face-centered cubic, body-centered cubic or hexagonal closed-pack structures. Thus, HEA concept with a vast number of elemental combinations, offers the possibility to design technologically relevant alloys, containing stable oxide-former elements and refractory elements, with an immense potential for high temperature applications. Recent studies on high-entropy alloys reporting good phase stability following ion irradiation up to 50 dpa make them potential candidates for the structural materials in fusion and fission reactors. Therefore, the possibility to produce HEAs with a combination of high corrosion, high creep and high irradiation resistances properties, which are required for structural materials in energy-related high temperature applications, must be explored.

It is known that molten lead and lead alloys are under consideration as working fluids for various energy-related applications, such as advanced nuclear reactors and concentrated solar power. However, the compatibility of such environment with structural steels, in terms of corrosion and mechanical resistance, causes considerable concerns.

We report some preliminary results on the corrosion behaviour of aluminium containing high-entropy alloys exposed to oxygen containing molten lead at 600°C.

Five alloys belonging to the AlCrFeNiX (X: Co Mn) high-entropy alloy system, with small addition of reactive elements (Y, Zr), were synthesized from high purity elements using arc melting procedure.

Prior to corrosion testing, the microstructure of the alloys was evaluated using scanning electron microscopy combined with energy dispersive X-Ray spectroscopy (SEM/EDS) methods. Backscattered electron images (BEI) of the as-cast alloys revealed that the microstructure consists of large, columnar grains with dendritic sub-structure (Fig. 2.8.4).
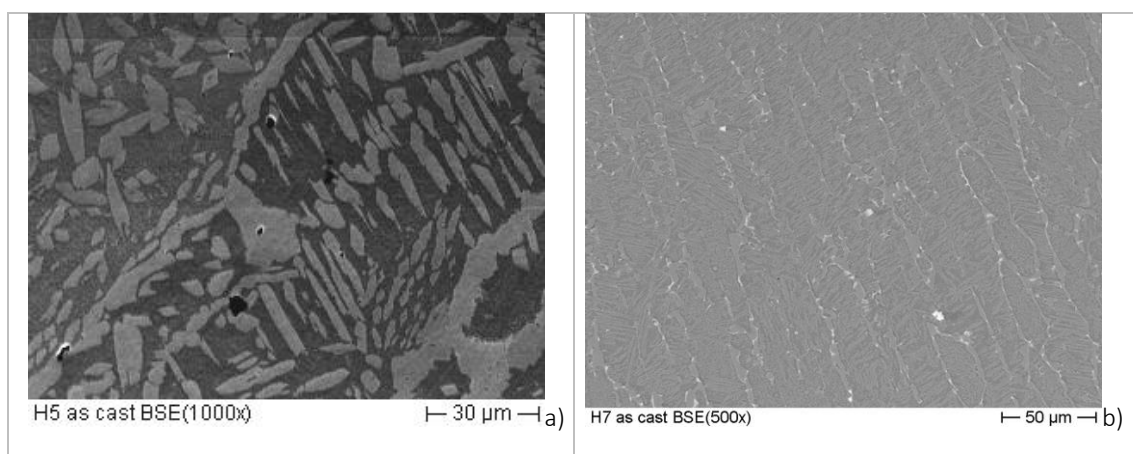
Fig. 2.8.4: Backscattered electron images (BEI) of the $Al_{11.1}Cr_{22.2}Fe_{22.2}Ni_{22.3}Mn_{22.2}$ (a) and $Al_{12.7}Cr_{21.6}Fe_{21.7}Ni_{21.7}Co_{21.6}Zr_{0.7}$ (b).

The phase composition of the alloys was determined using X-Ray diffraction (XRD). The phases constituting the as-cast alloys are the f.c.c and b.c.c., as can be seen in the patterns presented in Fig. 2.8.5.
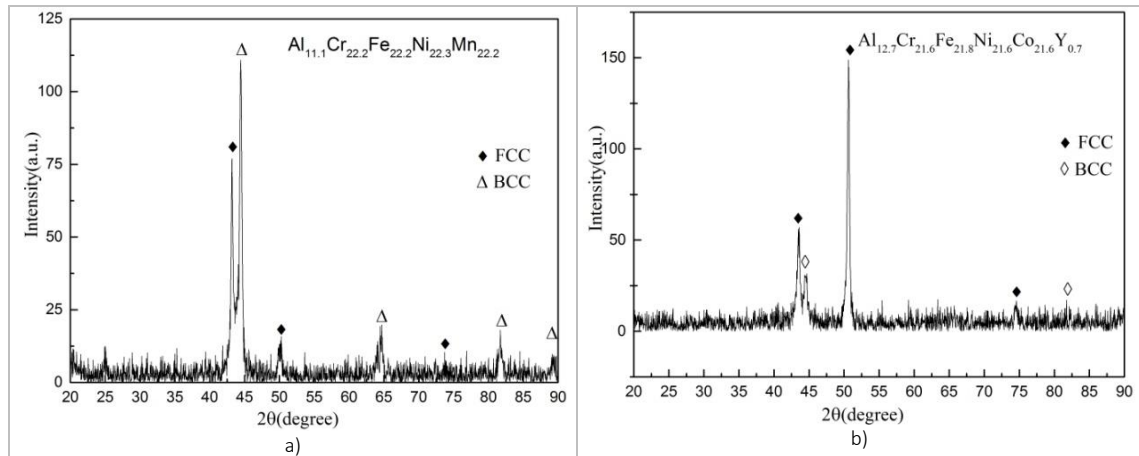
Fig. 2.8.5: XRD patterns of $Al_{11.1}Cr_{22.2}Fe_{22.2}Ni_{22.3}Mn_{22.2}$ (a) and $Al_{12.7}Cr_{21.6}Fe_{21.8}Ni_{21.6}Co_{21.6}Y_{0.7}$ (b) alloys in as-cast state.

The alloys ingots were cut into discs with around 1.2 mm thickness. All specimens were mechanically grinded with 1200 grit abrasive SiC paper and then were exposed to stagnant molten lead containing 10^{-6} wt.% oxygen in COSTA facility, at 600°C for 3500 hours. After the extraction from the melt the specimens were cleaned with a solution of ethanol, acetic acid and hydrogen peroxide (1:1:1) to remove the remaining adherent lead and to make the oxide layer itself accessible for inspection.

The morphology of the oxide scales grown, during the exposure to oxygen-containing molten lead, on the surface of the specimens was examined by SEM. No dissolution attack was observed for any of the samples tested. The general aspect is generally smooth as can be observed in Fig. 2.8.6.
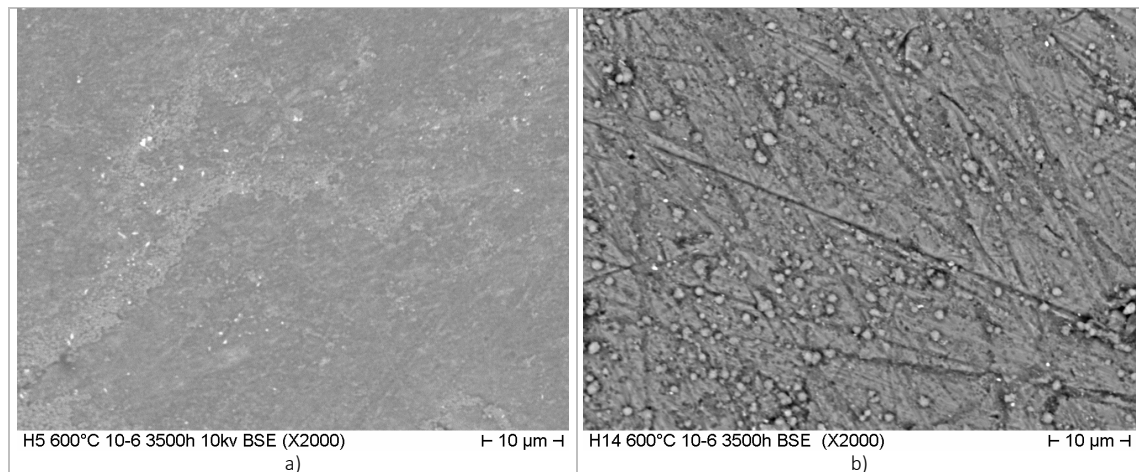
Fig. 2.8.6: Examples of the morphologies of the oxide scales grown, during the exposure to oxygen containing molten lead, on the surface of the specimens made from alloys $Al_{11.1}Cr_{22.2}Fe_{22.2}Ni_{22.3}Mn_{22.2}$ (a) and $Al_{13}Cr_{21.7}Fe_{21.8}Ni_{21.8}Co_{21.7}$ (b).

The cross section examination of the specimens revealed that the samples are covered by a protective oxide scale with thickness varying from around 2 μm in case of the alloy $Al_{11.1}Cr_{22.2}Fe_{22.2}Ni_{22.3}Mn_{22.2}$ to less than 0.5 μm in case of the samples made from $Al_{13}Cr_{21.7}Fe_{21.8}Ni_{21.8}Co_{21.7}$ and $Al_{12.7}Cr_{21.6}Fe_{21.7}Ni_{21.7}Co_{21.6}Zr_{0.7}$ alloys (Fig. 2.8.7).
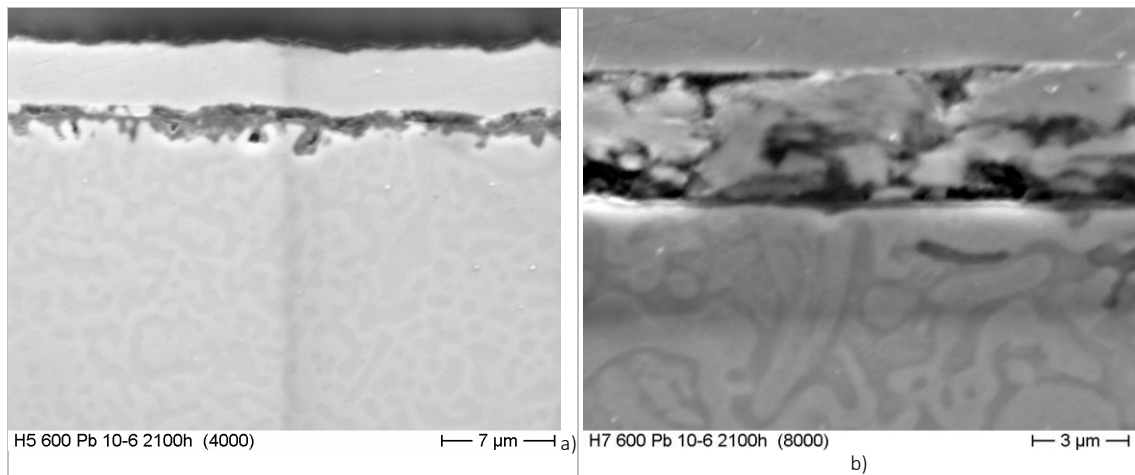
Fig. 2.8.7: Cross sections of the samples made from $Al_{11.1}Cr_{22.2}Fe_{22.2}Ni_{22.3}Mn_{22.2}$ (a) and $Al_{12.7}Cr_{21.6}Fe_{21.7}Ni_{21.7}Co_{21.6}Zr_{0.7}$ (b) alloys exposed to oxygen containing molten lead for 3500h at 600°C. The scale thickness varies from around 2 µm (a) to less than 0.5 µm (b).

The line scan presented in Fig. 2.8.8 (a), shows a duplex oxide scale which protect the sample made from $Al_{11.1}Cr_{22.2}Fe_{22.2}Ni_{22.3}Mn_{22.2}$ against dissolution attack. The outer layer is an Al-rich oxide, while the inner layer is an oxide rich in Mn. In case of the sample made from $Al_{13}Cr_{21.7}Fe_{21.8}Ni_{21.8}Co_{21.7}$ the protective layer grown only below the initial sample surface and is rich in Al (Fig. 2.8.8 b)
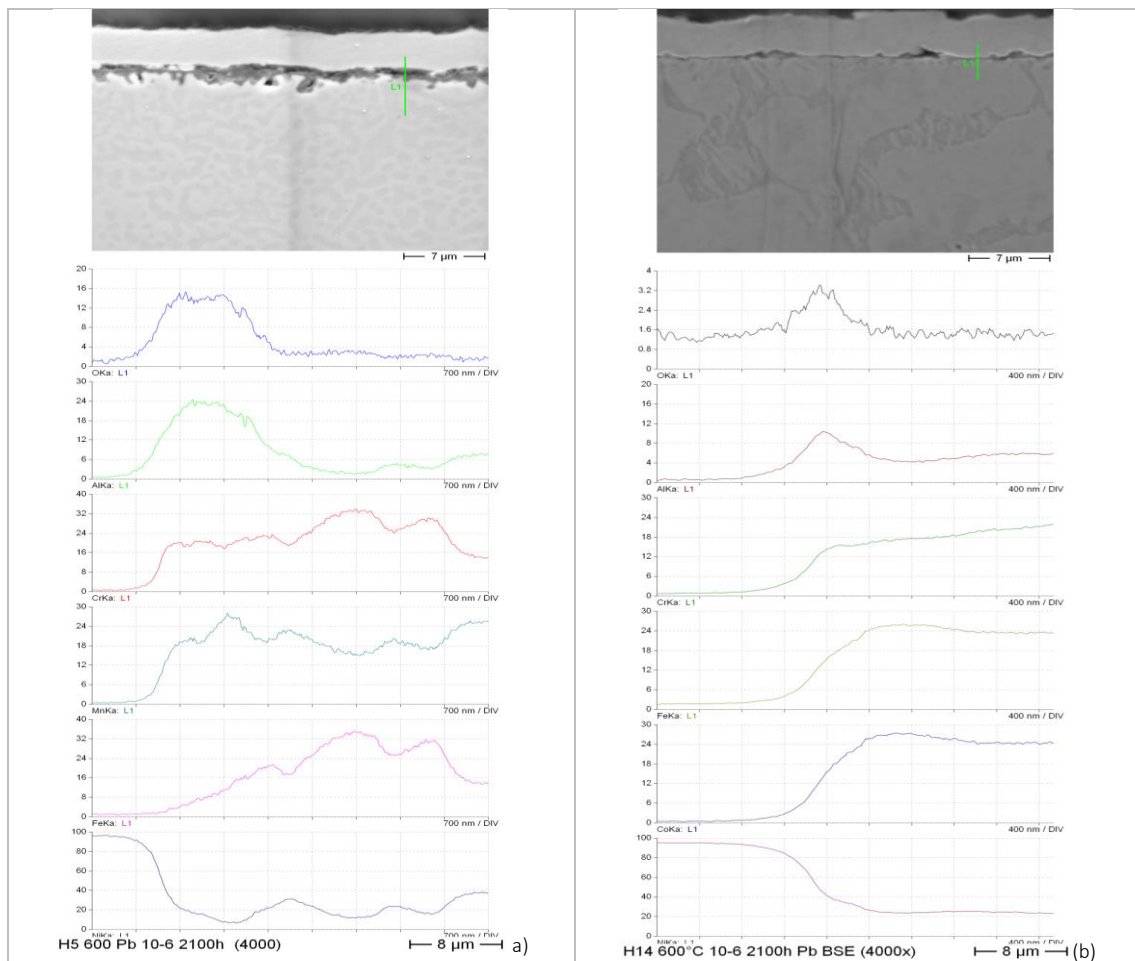
Fig. 2.8.8: EDX line scan showing the duplex oxide scale formed on $Al_{11.1}Cr_{22.2}Fe_{22.2}Ni_{22.3}Mn_{22.2}$ sample (a) and the EDX line scan of a very thin Al –rich oxide scale formed on $Al_{13}Cr_{21.7}Fe_{21.8}Ni_{21.8}Co_{21.7}$ sample.

68

The research program covering the high-entropy alloys for energy related applications will be continued during next period with activities concerning HEA's structural stability at high temperatures and under irradiation, corrosion resistance and mechanical properties. Exposure test in Pb at even higher temperatures and in Na will follow.

2.8.2   GESA-SOFIE and related simulations

The quasi-planar GESA consists of three functional regions: beam formation; beam compression and transport; target. The regions can be characterized concerning their influence on the beam quality. At the target an ion beam is formed, which has moderate influence on the electron beam; in the compression and transport region, the electron energy and beam diameter are limited from below; the beam formation region has a strong influence on the beam stability and the limitation of the beam intensity and pulse duration. Therefore, the region of beam formation is essential regarding the fundamental applicability of the electron beam for surface treatment and the investigations of GESA-SOFIE focused on the cathode-grid gap and beam formation.

In order to minimize the influence of the other functional regions (compression and transport, target) on the processes in the cathode-grid gap, a few measures were taken:
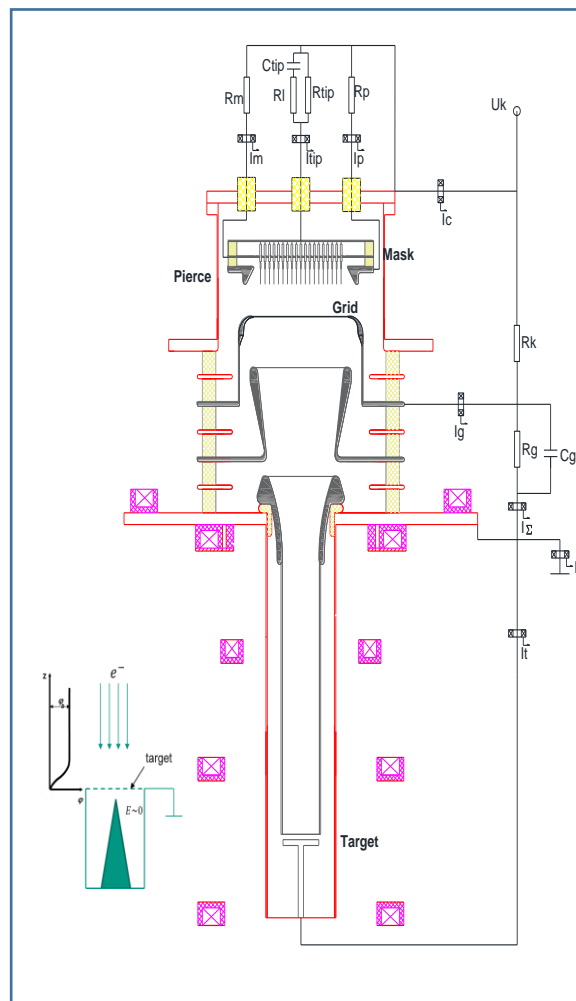
Fig. 2.8.9: Circuit of GESA-SOFIE. Position of current measurements.

Target built in the shape of a Faraday cage with 90% transparency of the entrance grid. Target plasma is formed inside the cage where only weak fields exist. Thus, the ion flow towards the cathode is suppressed. Additionally, the collector is cone-shaped with opening angle 15° at the tip in order to reduce the energy density at the target.

Installation of additional electrodes and change of transport channel diameter. The beam potential between grid and target becomes monotonic, thus trapping of electrons is avoided.

Reduction of magnetic field in transport channel. The beam diameter at the target is increased and thus deposited energy density is further reduced.

All GESA facilities are equipped with cathodes based on multipoint explosive emission. The emission plasma is generated at the tips of carbon fiber bundles. The fiber bundles are connected via resistors ($1 - 2$ kOhm), which limit the currents to the fibers until all tips are ignited (~100ns). The general observation of GESA operation with default parameters is an increasing perveance during the pulse. This increase cannot be completely captured by the voltage change. It can be concluded that the effective distance of the acceleration gap continuously decreases with time. Possible causes are the motion of the emission front towards the grid and/or generation of plasma at the grid.

Our investigations aim at

      1. Motion of the cathode plasma front – origin and possibility of control;
      2. Grid plasma – formation and influence on gap impedance.

The cathode region was reconstructed to allow current and voltage measurements on each component in contact with the cathode plasma. The components are connected to the circuit outside the vacuum chamber. This allowed flexible adjustment of the voltage distribution between the components and thus indirect control of the cathode plasma parameters.
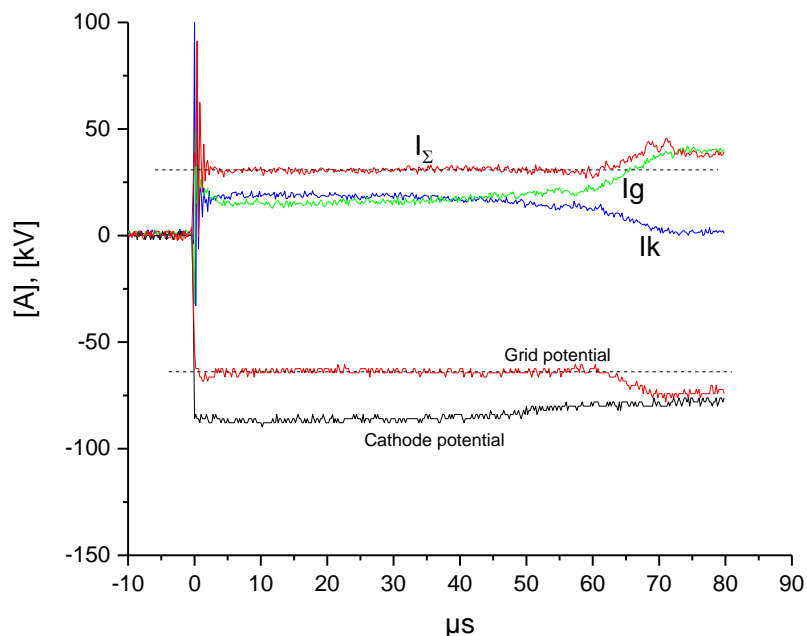
Fig. 2.8.10:   Grid potential is independent of grid current.

The grid potential is adjusted by the choice of the resistances Rk and Rg (Fig. 2.8.9). In order to minimize the influence of grid current variations on the emission plasma behavior, a constant grid potential is intended. This is feasible if Rk is chosen as small as possible compared to Rg. For constant cathode potential we have

$$dI_k = -\frac{R_g}{R_k + R_g} dI_g$$

Thus, for Rk<< Rg the change of the grid current, dI_g, is compensated by the change of dI_k and the sum that controls the grid potential is constant, $I_\Sigma = I_k + I_g$ (Fig. 2.8.10).

The streak camera Hamamatsu C7700 was used to observe the dynamics of cathode and grid plasmas. The imaging system is telecentric both on the objective and on the image side so that the cathode-grid gap is imaged with minimum perspective deformation. The framing camera Memrecam HX-3 (NAC Image Technology) was used to monitor spatial distribution and ignition behavior simultaneously at cathode and grid.
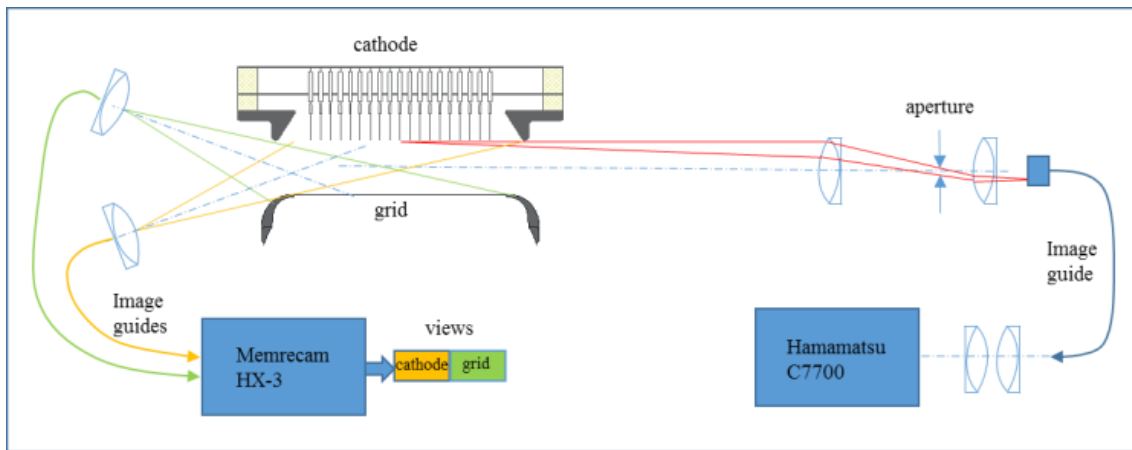
Fig. 2.8.11:   Setup for optical diagnostics.

Results: Cathode plasma

Current and voltage waveforms as well as streak images of a typical GESA-SOFIE pulse are shown in Fig. 2.8.12. The currents on the Pierce electrode and on the mask start immediately after the onset of the pulse and their qualitative evolution is identical to the one of the emission current, Ic. In spite of the significant distance of mask (50 mm) and Pierce electrode (30 mm) to the carbon fiber tips, the signals start without detectable time delay. Because the plasma expansion towards the mask occurs in a region of weak electric field, the expansion velocity can reach tens of cm/µs.
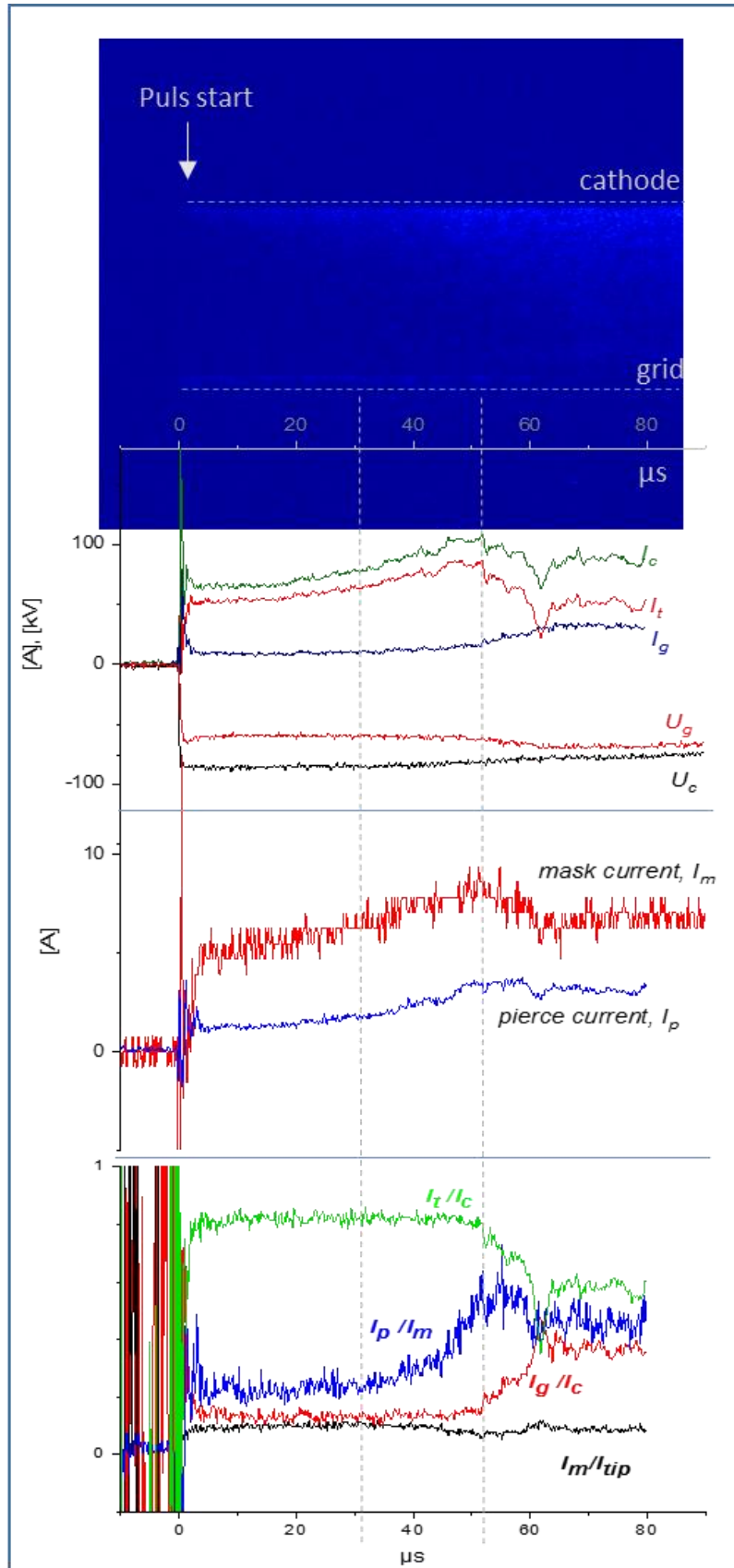
Fig. 2.8.12: Typical current and voltage waveforms of GESA-SOFIE.

In general, the currents on the mask and Pierce electrode can be composed of three contributions: ion current from grid and target plasma, Bohm current from plasma sheath, and electron current from emission spots on the surfaces of mask and Pierce electrode, which are ignited at high voltage drops between the cathode plasma and the conducting surfaces. These three contributions are discussed in the following.

Within the allowable range of mask potentials the current of the ion beam does not depend on the mask potential. Thus, the contribution of the ion current to the mask current can be determined from the asymptotic behavior of the mask current for resistance $R_m \rightarrow \infty$, see Fig. 2.8.13, and is below 1 A. The same result is obtained by estimating the maximum possible ion currents from the target and grid plasmas. The ion current from the target plasma is bounded by complete neutralization of the electron beam:

$$\frac{J_i}{J_e} \frac{\beta c}{v_i} \leq 1$$

For an electron current density of 3 A/cm² and a beam potential of ~30 kV against the target potential, we find $J_{imax} < 16$ mA/cm² or $I_{imax} < 0.5$ A. Similar values are obtained for the ion current from the grid plasma.

A strong indication for the formation of emission spots is an unstable operation of the accelerator. A continuous motion of the cathode spots, contraction and expansion, termination and re-ignition as observed in framing images strongly influence the cathode plasma parameters and result in an inhomogeneous emission behavior. An unstable regime is obtained for mask resistances below 300 Ohm.

For Rm values in the range of 300 to 2000 Ohm the mask current is determined predominantly by the saturation currents of ions and electrons in the plasma sheath:

$$I_m = I_i + I_e \, e^{-\frac{e\Delta\varphi}{kT_e}}$$

Here I_i, I_e are the ion and electron saturation currents and $\Delta\varphi$ is the potential drop between plasma and mask.
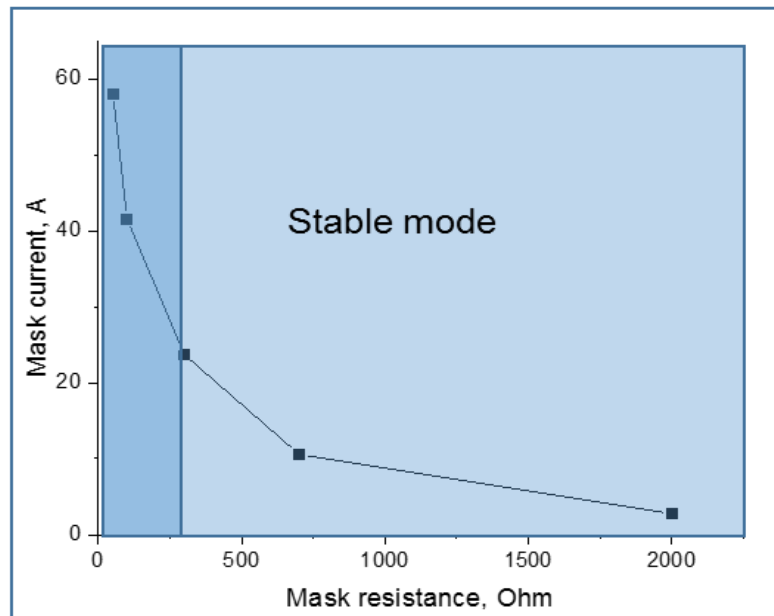
Fig. 2.8.13:   Mask current versus resistance.

As long as the mechanism of current flow between plasma and mask does not change, the mask current is determined directly by the parameters of the cathode plasma and thus indirectly by the current through the carbon fiber tips, Itip. Analysis of the current data shows that the ratio $\frac{I_m}{I_{tip}}$ remains almost constant during the pulse. This indicates stable plasma parameters. The evolution of $\frac{I_p}{I_m}$, however, shows a distinct rise after ~30 µs. This increase can be explained by an increase of the contact area between cathode plasma and Pierce electrode due to radial expansion of the plasma. Analysis of the ratio $\frac{I_g}{I_c}$ further confirms radial plasma motion perpendicular to the magnetic field lines. After ~50 µs the grid current strongly increases at simultaneously decreasing emission current. This is only possible if the effective transparency of the grid decreases. With a radial extent of the cathode plasma exceeding the grid opening, more and more emitted electron strike the grid holder.

Although an increase of the magnetic field strength at the cathode does indeed result in a lower ratio of the grid current during the pulse (Fig. 2.8.14), the radial plasma expansion can not be avoided.
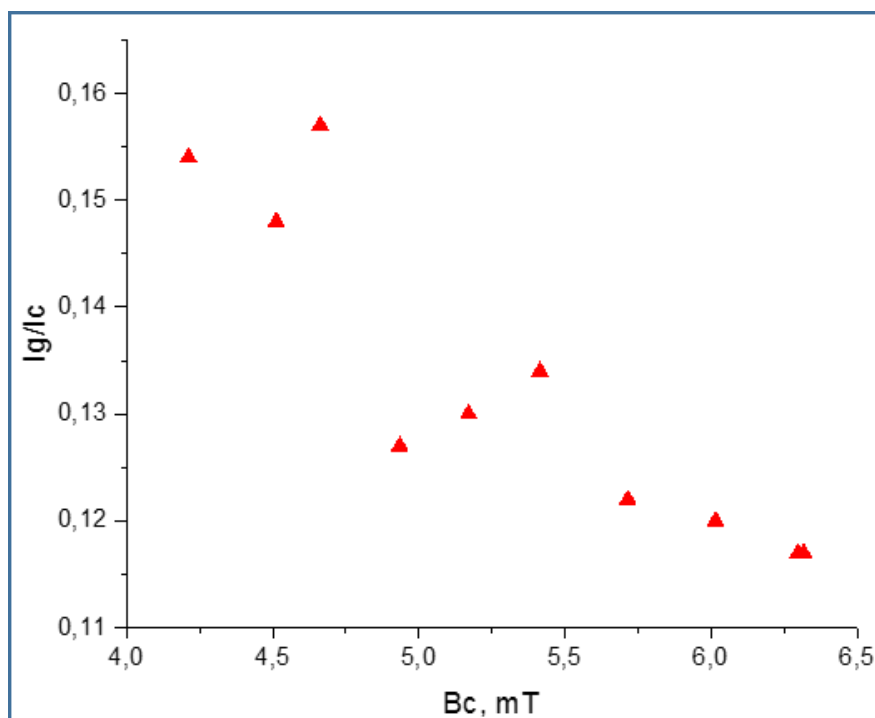
Fig. 2.8.14: Ratio of grid current versus magnetic field strength at cathode.

Results: Grid plasma

For default operation of GESA-SOFIE (mask current below 20 A), grid plasma is recognized after ~45 µs. Although light emission at the grid is observed very early in the pulse (Fig. 2.1.15), this does not necessarily indicate the existence of plasma. Plasma requires ionization rates in the vapor cloud exceeding recombination and ion emission towards the cathode. Once plasma is formed, it will expand towards the cathode. Therefore, expansion of the region showing light emission indicates the existence of plasma. After ~45 µs the grid plasma starts to expand. At the same time the grid current increases. The fastest rise of Ig is observed for decreasing emission current. As discussed above, this is caused by the radial expansion of the plasma and the fact that an increasing number of emitted electrons strike the grid holder. The increase of the grid current leads to a decrease of the potential drop between cathode and grid. This results in a lower emission current.
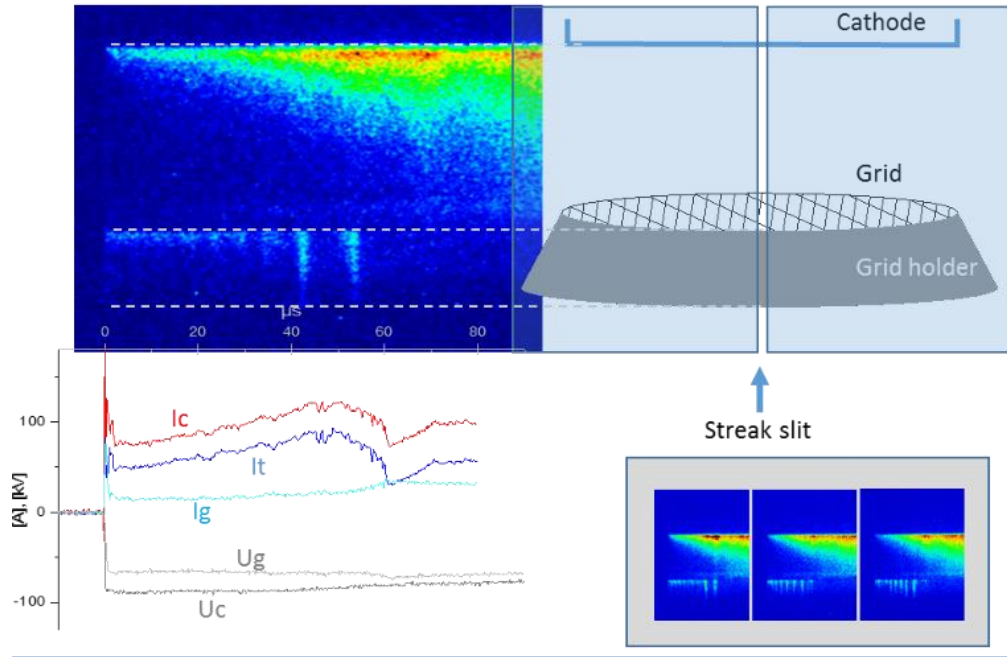
Fig. 2.8.15: Streak images of the cathode-grid region. The grid is imaged with a slight perspective deformation, the cathode without. The focus is on the front rim of the grid holder.

The cathode-grid voltage reaches a minimum after ~60 µs, then slightly increases and stabilized at ~10 kV for a rather long time (hundreds of µs). This stabilized potential drop depends on the plasma parameters. For high emission current a plasma with higher density is generated and the voltage drop is lowered to values around 3-4 kV. For thinner cathode plasmas, voltage drops of up to 13-14 kV were achieved.

The minimum of the voltage drop at ~60 µs coincides with the minimum of the emission current and the maximum of the grid current. Obviously closure of the gap between the cathode plasma and the grid plasma occurs at that moment. Although the gap impedance reaches a minimum value, short-circuiting does not occur, because the current is limited by the saturation currents of the electrons,

$$J_e = e n_k \sqrt{\frac{kT_{ek}}{2\pi m}} \text{ and ions, } J_i = e n_g \left(0.4 \sqrt{\frac{kT_{eg}}{M}} + v_g \right).$$

Here, the indices "k" and "g" denote cathode and grid plasma and v_g is the expansion velocity of the grid plasma. Once this limit is reached, a double layer is formed across which the total voltage drop occurs. The further evolution of the double layer depends on the plasma parameters and the voltages applied by the circuit.

Plasma gap closure is hardly detectable by the streak images. The reason is that grid plasma is formed primarily adjacent to the grid holder and the location of the gap closure is expected to occur outside the transparent part of the grid. Due to the small extent of the grid plasma above the grid holder the optical path is not long enough to obtain a good signal.

Conclusion

The radial expansion of the cathode plasma significantly influences the operation of the accelerator. It induces processes that lead to a transition from a regime of vacuum between cathode and grid to a regime of plasma-filled cathode-grid gap. Whether this transition is advantageous or disadvantages for the application depends on the applicability of the electron beam formed in the double layer of the plasma-

filled regime. In any case, the reason of plasma expansion perpendicular to the magnetic field lines needs to be further explored in order to either suppress or control this process.

Another important aspect of future research is the control of the cathode plasma parameters. The aim is to uncouple the plasma generation rate and the perveance evolution of the system. Possible approaches are the introduction of a modified mask with larger contact area or the use of a plasma generator with independent power source.

Involved Staff:

DP W. An, A. Neukirch, Dr. A. Heinzel, DI (Fh) F. Lang, Prof. G. Müller, Dr. G. Schumacher (Gast), H. Shi (SCS-PhD student), A. Sivkovich, **Dr. A. Weisenburger**, W. Zhen (SCS-PhD student), DI (Fh) F. Zimmermann,

3 Safety Research for Nuclear Reactors (NUSAFE): Transmutation – Liquid Metal Technology –

3.1 Materials and oxygen transport and control in heavy liquid metal cooled subcritical systems (MYRRHA)

Long-living high-level radioactive waste from existing nuclear power reactors should be transmuted in short-living radio nuclides using fast neutrons provided by a spallation target in an accelerator driven subcritical system or by a fast nuclear reactor. The objective is to reduce the final disposal time of high-level radioactive waste (plutonium, minor actinides) from some 10^6 years down to about 1000 years. Lead (Pb) and lead-bismuth (PbBi) are foreseen as spallation-target and coolant of such devices.

The aim of the institute's contribution is the development of a suitable corrosion protection especially for parts under high loads like fuel claddings or pump materials in contact with liquid Pb or PbBi. Pulsed large area electron beams (GESA) are used to modify the surface of steels such that they fulfill the requirements of their surrounding environment. Corrosion test stands for exposure of specimens under relevant conditions are developed and operated. Test facilities for combined loads like erosion and corrosion and fretting corrosion were developed, built and operated. Conditioning the Pb with regard to its oxygen concentration and the transport of oxygen in PbBi are additional aspects of the work.

All tasks are embedded in European and international projects and cooperations like e.g. ESNII+, MaTISSE and MYRTE.

The most relevant results obtained in the reporting period are briefly presented:

3.2 Erosion-tests of promising materials for liquid metal pumps (MATISSE)

In MATISSE so called MAXPHASE materials (ternary carbides) are explored for their use in Pb alloy cooled nuclear systems. One objective beside the production of new types of such materials including CERMETS is the testing of their stability against erosion-corrosion in the CORELLA facility. Three different MAXPHASE materials (Zr_3AlC_2, Zr_2AlC, $(Nb,Zr)_4AlC_3$ ground & milled) and 316L steel ground as reference were tested under following conditions: Temperature – 500 °C, duration - 1000 h, LBE with [O] ~ $1x10^{-8}$ mass%, v ~ 8 m/s (800 rpm) – highly turbulent flow. Surface profilometry using a white light interferometer before and after the test run in combination with SEM observation of cross sections were employed for inspection. All specimens were cleaned from sticking LBE prior to inspection. Both Zr based Maxphases were broken during the take out, the NbZr Maxphases stay intact (Fig. 3.2.1). From the 316L sample not all LBE could be removed, which indicates an at least starting corrosion attack. At the Zr-based Maxphases no LBE remained after cleaning. However the Zr_3AlC_2 looks somehow attacked. The edges look rounded and the roughness increased significantly (Fig. 3.2.2). The SEM cross section of the Zr_3AlC_2 specimen reveals the formation of a Zr-oxide scale. The other Maxphases do not show any corrosion attack, which is in contrary to the 316L specimens considered as reference. There, the SEM cross section clearly shows a localized corrosion-erosion attack.

Before CORELLA Testing					After CORELLA Testing				
Zr$_2$AlC ground	Zr$_3$AlC$_2$	(Nb,Zr)$_4$AlC$_3$	(Nb,Zr)$_4$AlC$_3$	316L	Zr$_2$AlC ground	Zr$_3$AlC$_2$	(Nb,Zr)$_4$AlC$_3$	(Nb,Zr)$_4$AlC$_3$	316L
		ground	milled				ground	milled	

Fig. 3.2.1: Photos of specimens before and after 1000h erosion corrosion test at 500°C.
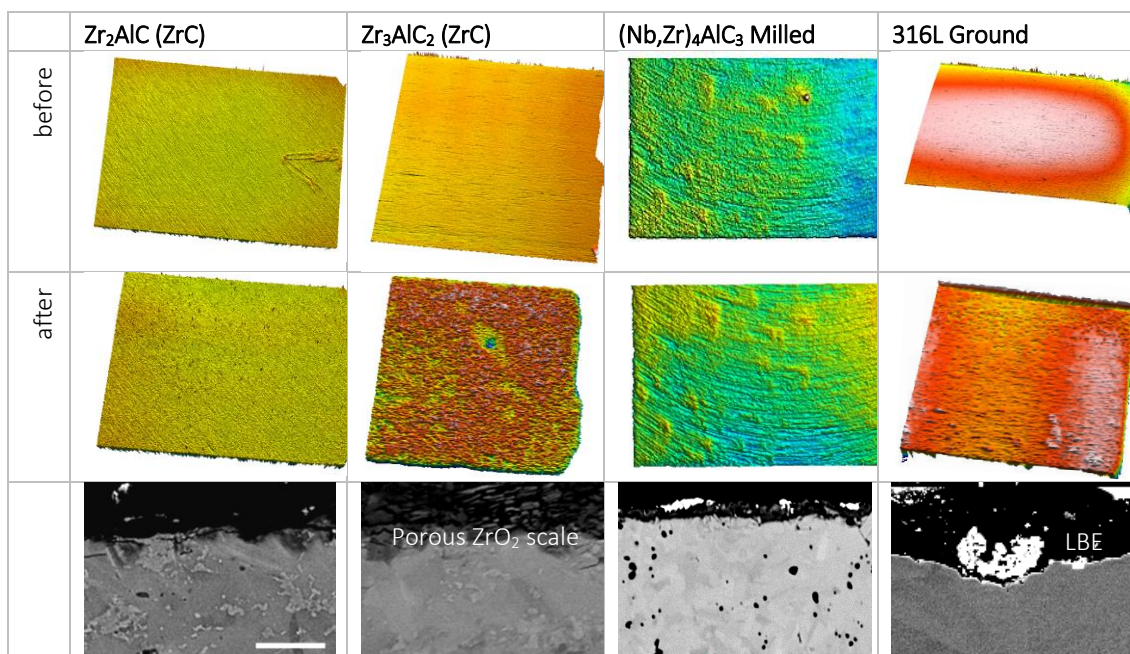
Fig. 3.2.2: Surface profiles and SEM cross sections of Maxphases before and after 1000h erosion corrosion test at 300°C.

3.3 Fretting tests in PbBi – wire wrapped configuration (MYRTE)

The MYRRHA reactor designed at SCK-CEN has a wire wrapped core configuration. The FRETHME facility used for fretting tests in liquid Pb-alloys in the past was designed for spacer grid fuel cladding configuration. Therefore, the sample holder were adapted to wire wrapped geometry allowing three geometrical configurations (parallel, cross and diagonal) having different contact areas. The contact pressure in cross configuration is about 10 times higher compared to the parallel arrangement (Fig. 3.3.1).

$$ppoint := 0.388 \cdot \sqrt[3]{\frac{F \cdot E^2}{r^2}} = \left(6.369 \cdot 10^9\right) \; \boldsymbol{Pa}$$

$$pline := \sqrt{\left(\frac{F \cdot E}{2 \cdot \pi \cdot r \cdot l \cdot \left(1 - \mu^2\right)}\right)} = \left(3.606 \cdot 10^8\right) \; \boldsymbol{Pa}$$
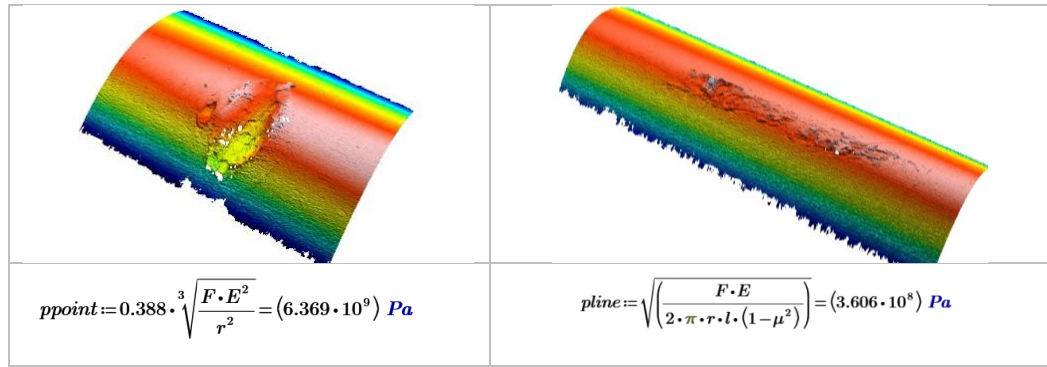
Fig. 3.3.1: Contact pressure of fretted samples in cross (left) and parallel (right) configuration.

To evaluate the influence of load, amplitude, time and geometrical configuration a set of experiments was performed during the internship of Mr. Nakabo from Japan. The load was varied between 20 and 100 N, the amplitude between 35 and 275 μm and the time from 100 to 300 h in cross and parallel and diagonal configuration (not all parameters are tested in all three configurations). All tests were performed with a frequency of 10 Hz in 400 °C hot PbBi having 10^{-7} wt% oxygen. The tested specimens were cleaned after the tests from residual PbBi and evaluated applying optical microscopy, scanning electron microscopy for surface and cross section inspection and white light interferometry for surface profilometry. Some experimental issues emerge during the tests; setting up the load especially at low values is quite challenging; the error resulting from this is significant larger at low loads compared to high loads; the parallel set-up is significantly more sensitive to misalignment compared to the cross configuration. Therefore, at time no final conclusions can be made, only preliminary tendencies are reported.

Varying in cross configuration the applied load at a constant amplitude range between 30 and 50 μm the maximum fretting depth increases first up to a turning point at a load between 50 N and 75 N and then decreases at 100 N load (Fig. 3.3.2 left). At higher amplitude of 150 μm the measured fretting depth of the 20 N test was disregarded due to experimental uncertainties. The two reliable fretting depths obtained at loads of 50 and 100 N indicate the excepted shift of the turning point to higher values at larger amplitudes.
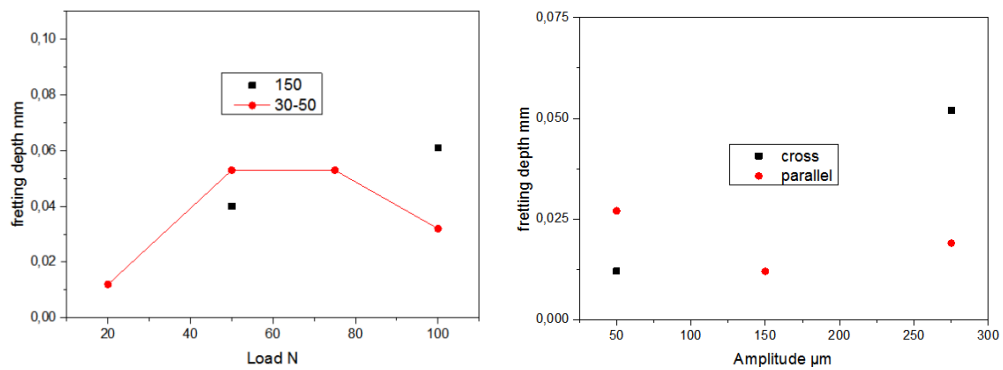
Fig. 3.3.2: (left) Maximum fretting depth as a function of applied load at constant amplitude of 30-50 μm and 150 μm (right) Maximum fretting depth as a function of amplitude at constant applied load of 20 N.

This phenomena is attributed to a threshold pressure required for the debris retention in the fretting area. Up to this threshold pressure the fretting depth increases as expected with increasing load. Further increase of load results in the retention and compaction of the debris and the creation of a kind of protecting layer. Comparing the fretting depth obtained with 20 N at different amplitudes in cross and parallel configuration two conclusions can be drawn (Fig. 3.3.2 right). First the difference in contact pressure between cross and parallel configuration is reflected in the difference in fretting depth. A more

detailed and perhaps quantitative analysis requires more experimental data that will be obtained in upcoming experiments. Second increasing the amplitude at constant load results in general in an increased fretting depth. Two SEM cross section (Fig. 3.3.3) made at the fretting area of the 20 N and 75 N specimen show the difference in damaging. At 20 N (Fig. 3.3.3 left) a kind of loose compacted debris is visible in the damaged area, the adjacent bulk material looks unchanged. At the 75 N specimen (Fig. 3.3.3 right) however, the debris is highly compact and the microstructure of the adjacent bulk looks deformed.

sample 15 tube 30-50µm 20N 100h 250x   ⊢ 100 µm ⊣   sample 17 wire 35-50µm 75N 100h 1000x   ⊢ 30 µm ⊣
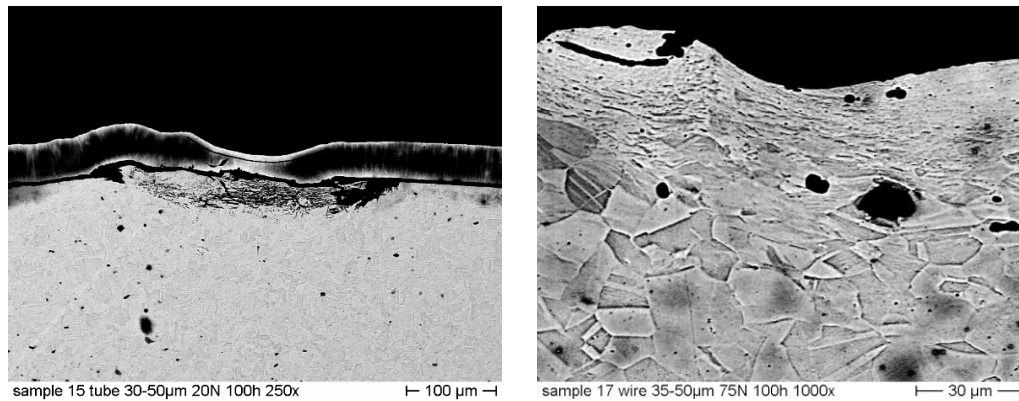
Fig. 3.3.3: SEM of cross section of tube tested with a 30-50 µm amplitude; left at load of 20 N; right at load of 75 N.

A reconditioning, including the exchange of some of the bearings, of the FRETHME facility to allow a more precise and reliable control of the amplitude is underway. After this dedicated experiments at 50 N, 100 h duration varying the amplitude between 25 and 200 µm to investigate the influence of the amplitude in more detail are targeted. In a second test cycle the duration will be changed from 100 h to 1000 h with a load of 50 N and a constant amplitude of 50 µm. Proceeding post investigations including the evaluation of the specific wear coefficient and possibly the prediction of expected wear at operating conditions are further objectives of this research.

3.4 Characterization of ODS under safety-related operation conditions (MaTISSE)

ODS (Oxide Dispersion Strengthened) alloy versions of ferritic steel can be a solution for high dpa resistant materials to be deployed in future GenIV nuclear reactors. Within the EU Horizon 2020 project MaTISSE, 9 and 12Cr-ODS are under investigation as potential fuel cladding materials. One focus is on their behavior in liquid lead under transient conditions and off-normal conditions like high temperatures as well as under low oxygen conditions. A test plan was established considering the analyses of representative DEC events of the ETDR (Alfred - EU project LEADER). In the conducted transient test the temperature of 550 °C was hold for 2000 h, increased to 750°C for 24h and hold again at 550 °C up to a total exposure time of 5000 h. Furthermore for comparison, tests with a constant temperature of 550 °C and 650 °C were conducted. For all tests an oxygen content of 10^{-6} wt% in the liquid lead was chosen. The ODS specimens were exposed in two conditions; as received or with a pulsed electron beam surface treatment. The latter was applied to homogenize the surface aiming to reduce localized corrosion. After GESA treatment 9Cr-ODS shows an around 23.5 µm restructured layer, while that of 12Cr-ODS was melted up to a depth of around 21 µm. However, the restructuring and cleaning was less prominent than expected.

The non-surface treated 9Cr-ODS sample showed after the transient test the known multilayer oxide on the surface consisting of magnetite, spinel and inner diffusion zone (IOZ) while the 12Cr-ODS sample showed a Fe rich Fe-Cr spinel with a IOZ underneath and at the border to bulk a Cr rich Fe-Cr spinel with Kirkendall Pores below. A negative influence of the temperature excursion was no detectable so far. At 650 °C (constant) after 2000 h a Cr-Mn-Si spinel with oxide roots was formed on the surface of 9Cr ODS. The roots show Pb inclusions and in one area dissolution attack was observed. After 5000 °C the entire surface showed a mixture between Cr-Mn-Si spinel with prominent Pb inclusions. Due to the higher Cr content the 12Cr ODS sample showed a slightly better corrosion behavior at 650 °C. A Cr-Mn spinel layer was formed at the surface with oxide nodes after 2000 °C and occasionally Pb inclusions can be observed after 5000 h exposure (Fig. 3.4.1). The changed microstructure in the GESA modified layer seems to favor diffusion along the grain boundaries, leading to an enhanced corrosion attack in time (Fig. 3.4.2). Exposure tests performed with the same material by CIEMAT (Madrid) at 600 and 700 °C in lead with 10^{-6} wt% oxygen showed a slightly improved compatibility of the GESA treated specimens compared with the non-treated ones.

Therefore, also considering the relatively weak changes in the microstructure of the treated area, the GESA parameters were investigated and adjusted to achieve an optimized structure. In addition an Al-coating applied by PVD was alloyed into the surface of the ODS samples using a GESA pulse. Such specimens are still exposed to Pb and the results will be reported as they are available.
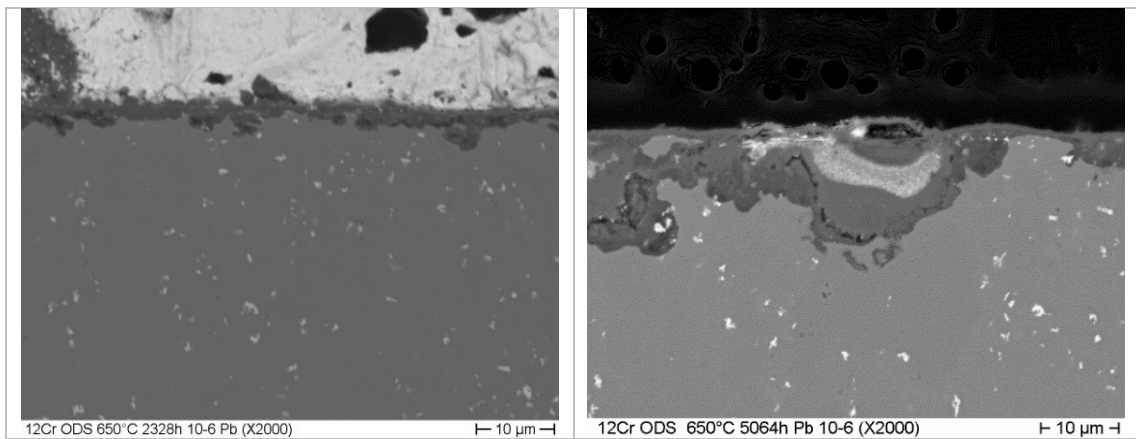
Fig. 3.4.1: SEM of 12Cr-ODS after exposure to Pb at 650 °C: left-after 2000 h, right after 5000 h.
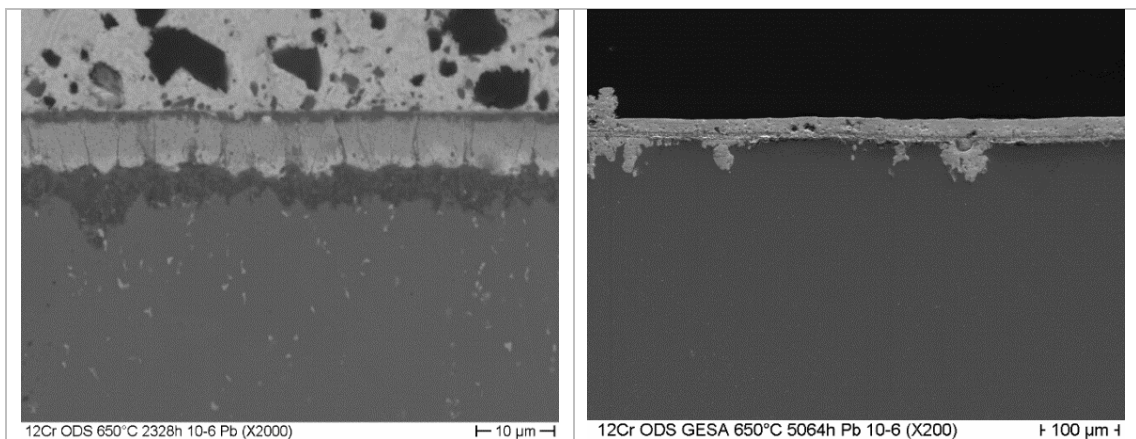
Fig. 3.4.2: SEM of 12Cr-ODS with GESA – pulse after exposure to Pb at 650 °C: left-after 2000 h, right after 5000 h.

3.5 Development of a Semiconductor-based Marx Generator for the GESA 1 device

The pulse power source currently driving the GESA 1 device consists of a LC-chain Marx generator using spark-gap switches and is capable of delivering a rectangular voltage pulse of around 120 kV to the cathode. As can be seen in Fig. 3.5.1 (left), the control grid is connected to ground via the resistor R_g causing a shift in the grid potential towards the cathode potential for increasing grid current. This negative feedback has a stabilizing impact on the cathode current. Due to the inherent dynamics of the cathode plasma, this passive control of the grid voltage via the grid resistor is insufficient in certain parameter ranges.
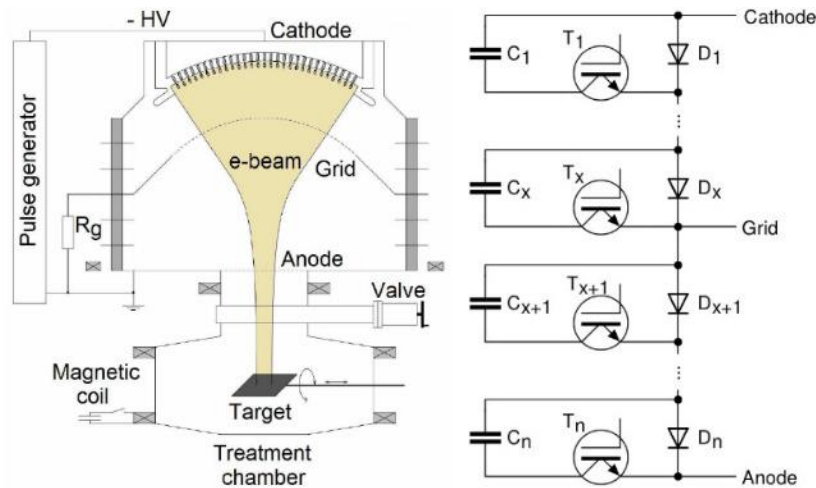
Fig. 3.5.1: Topology of the semiconductor-based Marx generator under development. Left: Schematic of the GESA 1 device, Right: Circuit.

The new pulsed power source currently under development will allow for a precise control of pulse length, cathode and grid voltage. The circuit topology is shown in Fig. 3.4.2 (right). The generator concept consists of around 150 individual modules, each comprising a capacitor (C), a switching element T and a by-pass diode (D). After all capacitors have been charged in parallel, closing the switching elements results in a series connection of the capacitors and, hence, a voltage multiplication at the output. Due to the by-pass diodes, stages may remain inactive, not contributing to the output voltage pulse. By subsequently opening or closing the switches during the pulse, the output voltage can be modified according the number of active stages and the remaining charge in their capacitances. For a direct control over the grid voltage, the grid is planned to be connected directly to the generator as can be seen in Fig. 3.4.2 (right), thereby allowing for a nearly independent control of grid and cathode voltage.

The main challenge for the employed switching elements is the required fast voltage rise time for a homogeneous cathode plasma ignition of around 100 kV/100 ns. This necessitated the development of a gate-boosting circuit for the IGBT switches as well as a fast optical signal transmission for trigger signal distribution. On each stage, a fast microprocessor and logic circuitry handle the switching signal generation during the pulse to create desired output voltage shape. The capacitor voltage droop during the pulse is compensated by subsequently adding active stages once the output voltage has dropped by 1 kV. Thereby, a flat top quality is expected to be around 1 %. The resulting high number of stages will be addressed via optical communication from a control unit handling the fast signal distribution, whereas the user interface for designing the output voltage shape will be situated on a PC. In the current stage of the project, the first stage of the Marx generator has been operated successfully in the complete control chain consisting of a preliminary PC user interface, the control unit and the stage itself. The graphs in Fig. 3.5.1 show first results

for one stage with the final output capacitance of 200 µF with 6 IGBTs in parallel configuration. The upper graph of Fig. 3.5.1 thereby shows the load current (red trace) of 250 A with a rise time of around 50 ns together with the voltage across the switching elements. The lower graph shows an example of the feasible arbitrary waveform generation. After the verification of the generator concept in a small scale version, the complete generator is scheduled to be operational in fall 2017.
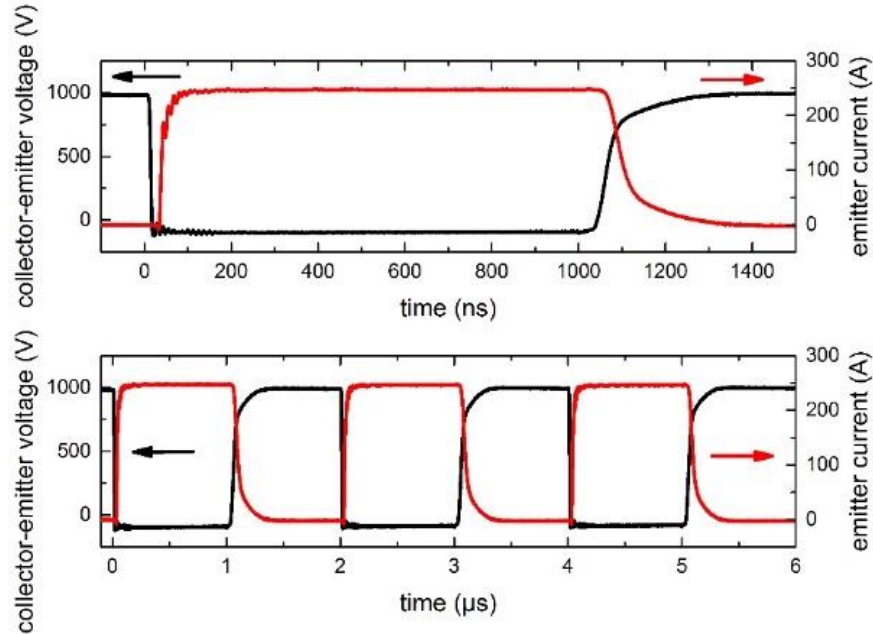
Fig. 3.1.8: Output voltage and current waveforms for one pulse (upper graph) and for an arbitrary waveform (lower graph).

3.6 GESA Beam Dynamics Simulations

The cylindrical triode-type pulsed electron accelerator GESA IV was specifically designed for surface treatment of cylindrical tubes such as cladding tubes of GEN IV fission reactors. However, due to the large difference between cathode and grid diameter on the one hand and the comparatively small target (anode) diameter on the other hand, unstable operation and inhomogeneous treatment is often observed. This may be caused by the formation of a virtual cathode between grid and anode or by the large distortion of electron trajectories due to the self-induced magnetic field. Another crucial phenomenon is the generation of ions at the target. In order to understand the underlying processes and improve the beam homogeneity and stability, a systematic numerical study of GESA IV beam performance was undertaken in the reporting period. Stable and homogeneous operation regimes could be identified.

For the numerical study, the PIC code simulation package MAGIC2D by Orbital ATK, USA, was used. The system geometry is shown below. A high voltage pulse is applied to the cathode via the input port. The potentials of cathode and grid against the grounded anode are controlled via the resistors R_{cg} and R_{ga}. Beam current reaching the target flows in axial direction along the target to the outer boundary. Primary beam electrons are generated at the cathode via the explosive emission routine. The beam electrons then move in accordance with the relativistic Lorentz equation in the free space of the simulation area until they hit a conductor. Backscattering of electrons at the target is included, i.e., when electrons hit the surface, secondary electrons (backscattered electrons) are emitted according to the target material specifications (in the shown case aluminum). The third type of charged particles considered in the simulation are protons. If included, they are emitted from the target surface obeying the space charge limit. Once emitted, also ions move according to the Lorentz equation until they hit a conductor.
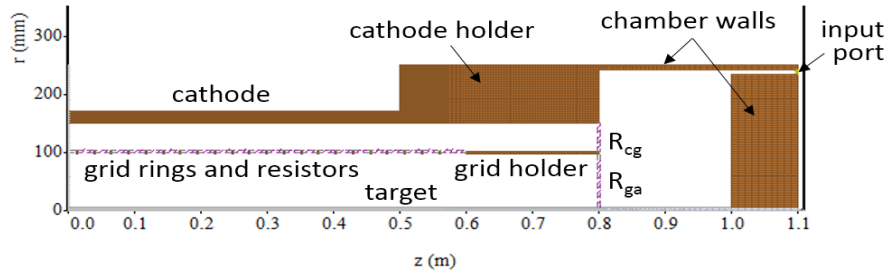
Fig. 3.6.1: System geometry. Mirror symmetry at z=0 is assumed as well as azimuthal symmetry. The accelerator is composed of the outer chamber walls, cathode and cathode holder, grid rings and grid holder, and the target anode. Line resistors R_{cg} and R_{ga} connect cathode holder, grid holder, and target. Additional line resistors connect the individual grid rings.

First, unipolar electron flow is considered, i.e., protons are not included in the simulations. The performance of unipolar flow is of interest for the initial stage of pulsed electron beam application when ion generation at the target and ion motion towards the cathode are negligible. The cathode voltage is fixed at U_{ca} = 120 kV in the simulations, while the ratio of the controlling resistors R_{cg} and R_{ga} is varied. Results of the simulation with U_{cg} = 18 kV are shown in the figure.
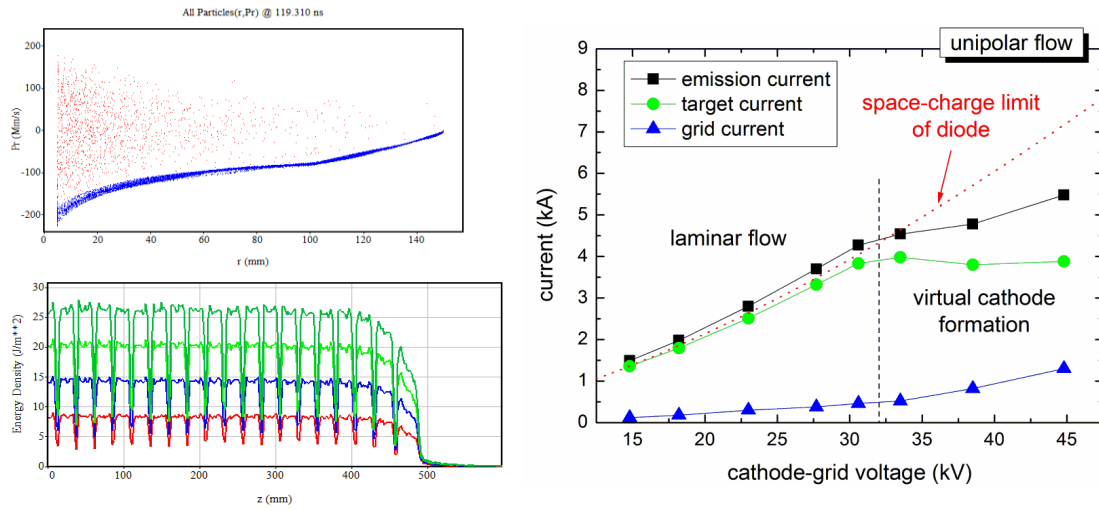
Fig. 3.6.2: Simulation results for unipolar flow and constant cathode-anode voltage 120 kV. Left: Situation for U_{cg} = 18 kV. (a) Radial momentum versus radial position; blue dots represent primary beam electrons, red dots indicate electrons backscattered at the target; (b) accumulated beam energy density at target surface versus axial position at four times between 47 ns and 119 ns. Right: Emission, target, and grid currents of the full length accelerator versus cathode-grid voltage.

The beam electrons (blue dots) are continuously accelerated from the cathode at r = 150 mm via the grid at r = 100 mm to the anode at r = 5 mm. The radial momentum of all beam electrons is negative, i.e., no primary electrons return towards the cathode. Backscattered electrons (red dots) are found mainly in the vicinity of the target. The beam energy density measured at the target is homogeneous (except the positions shaded by the grid rings). Laminar flow of beam electrons is obtained.

The emission current, grid current, and target current of the full accelerator are also shown in the figure for various grid potentials. Two different regimes are found, with the transition occurring at a cathode-grid voltage of about 32 kV. The previously described situation of laminar flow is obtained below this threshold. The emission current of the laminar flow regime agrees very well with the predicted space-charge limit of the corresponding cylindrical diode. Thus, processes between grid and target do not influence the beam characteristics in the cathode-grid gap.

For cathode-grid voltages above the laminar flow threshold of ~32 kV, the emission current stays well below the space charge limit of the corresponding diode. As the cathode-grid voltage is increased and the emission current and space charge become larger, a potential well between grid and target is formed and grows until a virtual cathode is obtained, see next figure. Due to electrons returning towards the cathode, the space charge also in the cathode-grid gap is increased, which lowers the emission current. Another consequence of the formation of a virtual cathode is the inhomogeneous beam power density at the target.
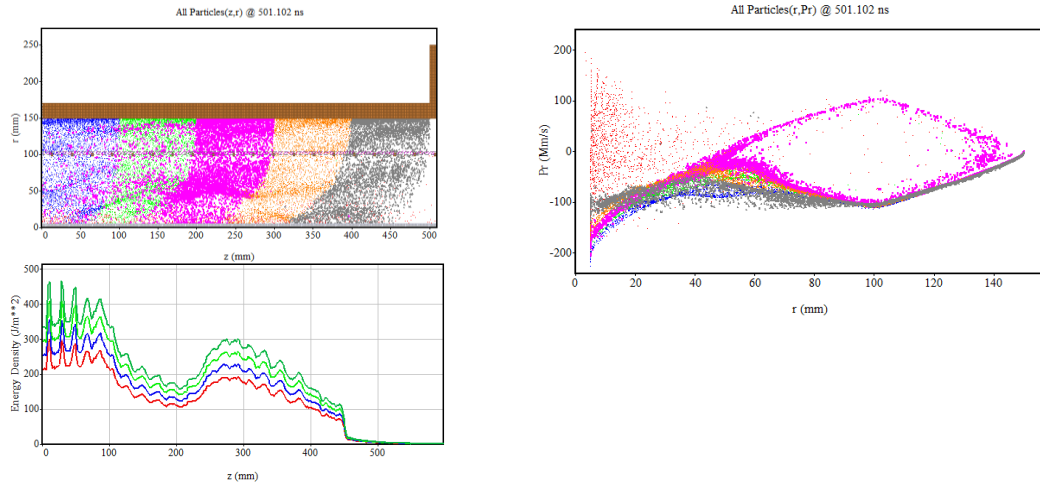
Fig. 3.6.3: Virtual cathode formation, observed for unipolar flow with U_{cg} = 33.5 kV: (a) particle distribution in (z,r) space, (b) radial momentum distribution versus radial position; beam electrons are represented by, respectively, blue, green, pink, orange, and grey dots; electrons backscattered at the target are represented by red dots; (c) accumulated beam energy density distribution at the target surface versus axial position at four times between 329 ns and 501 ns.

In order to achieve melting during target treatment, pulse durations in the microsecond range are usually chosen. On such time scales, ion flow from the target cannot be neglected. Therefore, space charge limited ion emission from the target is introduced in the simulations and the situation of bipolar flow is studied. The next figure shows the emission, target, and grid electron currents of bipolar flow for the full range of cathode-grid voltages investigated. Again a regime of laminar flow is found for low cathode-grid voltages. In this regime, the presence of counter-streaming ions results in an increase of the electron emission current by roughly 50 % against unipolar flow.
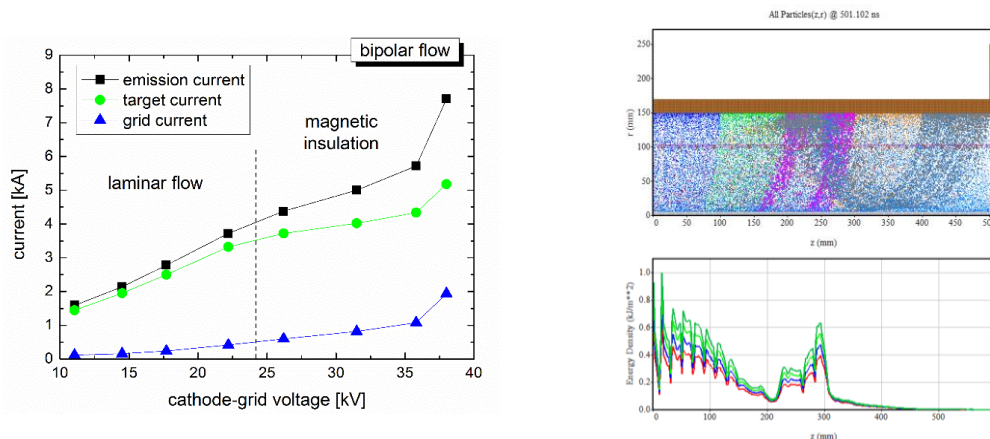
Fig. 3.6.4: Simulation results for bipolar flow and constant cathode-anode voltage 120 kV. Left: Emission, target, and grid currents versus cathode-grid voltage. Right: Situation for U_{cg} = 35.8 kV. (a) particle distribution in (z,r) space; beam electrons are represented by, respectively, blue, green, pink, orange, and grey dots; electrons backscattered at the target are represented by red dots, ions are represented by light blue dots; (b) accumulated beam energy density distribution at the target surface versus axial position at four times between 329 ns and 501 ns.

Beyond a cathode-grid voltage of ~24 kV the electron emission current seems to be reduced against the trend observed for laminar flow, although virtual cathode formation is not observed for bipolar flow. The reason for the emission reduction is magnetic insulation. The further away from the central axial position, the higher is the accumulated target current. The higher induced azimuthal magnetic field results in stronger bending of the electron trajectories on their way towards the target. Beyond a certain magnetic field strength, electrons are unable to reach the target and return towards the cathode (magnetic insulation). In the particular case shown in the figure, all electrons emitted at axial positions larger ~350 mm are unable to reach the target directly (i.e., all 'grey' electrons and some of the 'orange' electrons).

The increased electron space charge in the cathode region due to returning electrons from the beam edge leads to a reduced emission current. Returning electrons also result in an increase of the grid current and in an inhomogeneous beam power density at the target.

To summarize, simulations of the beam performance of the cylindrical pulsed electron beam accelerator GESA IV at given cathode voltage -120 kV showed different operation regimes depending on the cathode-grid voltage applied. For low cathode-grid voltages and low beam current, laminar flow conditions with homogeneous energy density at the target are obtained. The laminar flow regime exists for both unipolar electron beams and bipolar beams with counter-streaming ions generated at the target. It is the only feasible operation regime for homogeneous treatment of metal surfaces.

3.7 AFA-Alumina-forming austenitic – steels

Alumina-forming austenitic alloys, exhibiting high-temperature creep strength and oxidation resistance in dry and humid air, are a relatively new class of stainless steels. These main characteristics are due to the formation of stable nano-NbC, submicron B2-NiAl and Fe_2Nb Laves precipitates, which determine the creep resistance increase and the formation of an alumina protective scale, which improves the oxidation resistance in the 600-900 °C temperature range. The above mentioned properties, make alumina-forming austenitic steels potential candidates for structural materials in energy related applications.

So far only one attempt, performed by a research group from KTH – Stockholm, was made to evaluate the compatibility (at 550°C) of this class of stainless steels with heavy liquid metals, which are considered as working fluids in several energy-related applications. Therefore a systematic study is mandatory for defining the composition of alumina-forming stainless steels having compatibility with such environments.

Some preliminary results concerning the corrosion behaviour of alumina-forming austenitic steels, during their exposure to oxygen-containing molten lead, are reported below.

Two model alloys of FeCrAlNiX system (X: Ti, Nb, Zr, Mn), designed using Thermo-Calc software, to form protective alumina scale and in the same time to preserve the austenite structure during long term exposure in heavy liquid metals, were prepared by arc melting under argon atmosphere. XRD patterns of the as-cast alloys are presented in Fig. 3.7.1.
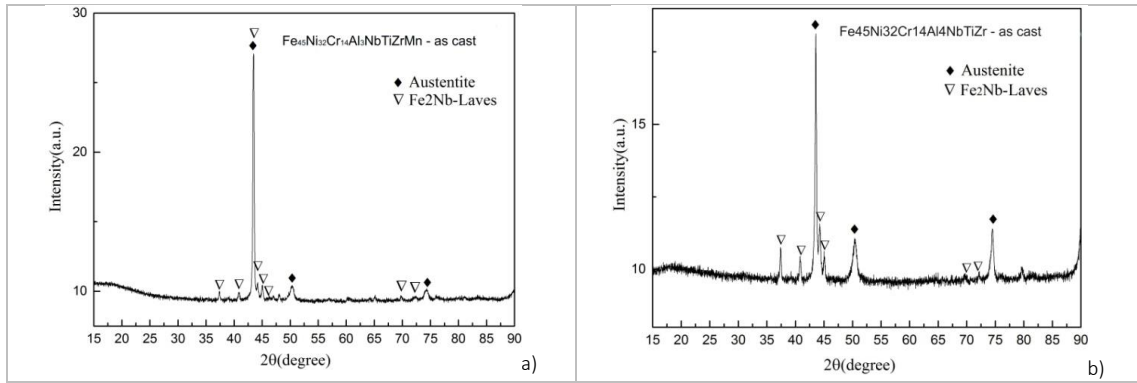
Fig. 3.7.1: XRD patterns of aluminium-containing stainless steels in as cast state: f.c.c. matrix and Fe2Nb Laves phase.

The constituting phases of both alloys are austenite (face centered cubic - f.c.c.), as matrix, and Fe_2Nb-type Laves phase (hexagonal) precipitated at the austenite grains boundaries.

The typical microstructure of the as-cast model alloys is presented in Fig. 3.7.2.
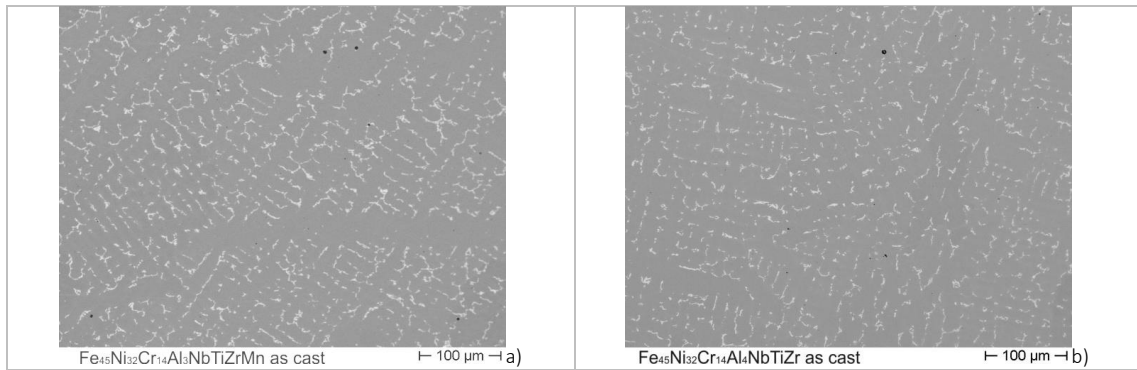
Fig. 3.7.2: SEM backscattered electron images of the model alloys in the as-cast state: f.c.c matrix with Fe_2Nb Laves phase at the grains boundaries.

Samples cut from these model alloys were exposed in stagnant molten lead with 10^{-6} wt.% oxygen, at 600°C for 2100 hours.

The morphology of the oxide scales grown, during the exposure to oxygen-containing liquid lead, on the surface of the specimens was examined by SEM. No dissolution attack was observed for any of the samples tested. The general aspect is generally smooth as can be observed in Fig. 3.7.3.
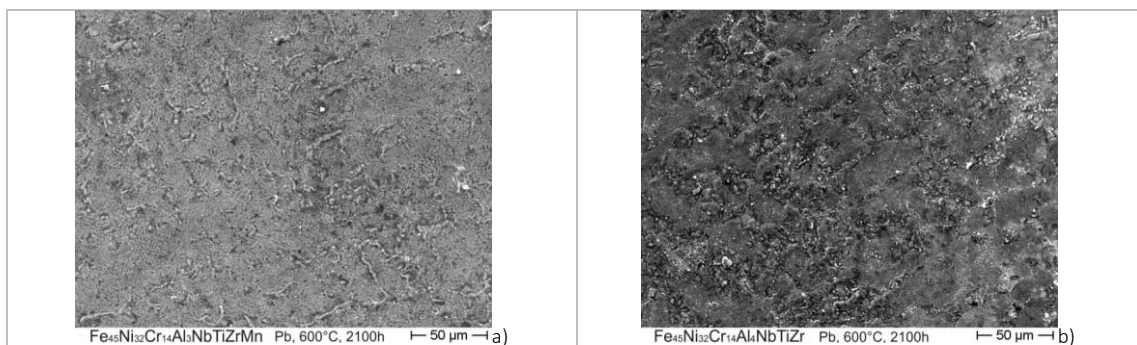
Fig. 3.7.3: The morphologies of the oxide scales grown during the exposure to oxygen containing liquid lead on the surface of the specimens.

The evaluation of the thickness and of the chemical compositions of the oxide scale, grown during exposure to oxygen-containing liquid lead, was performed on the cross sections of the exposed specimens. It was observed that the specimens were protected by a thin (300-400 nm) inward growing oxide scale, rich in Al and Ti, on around 80 % of their surface, while the remaining part were covered by islands of a thicker, also inward growing, Al-Cr-oxide (Fig. 3.7.4).
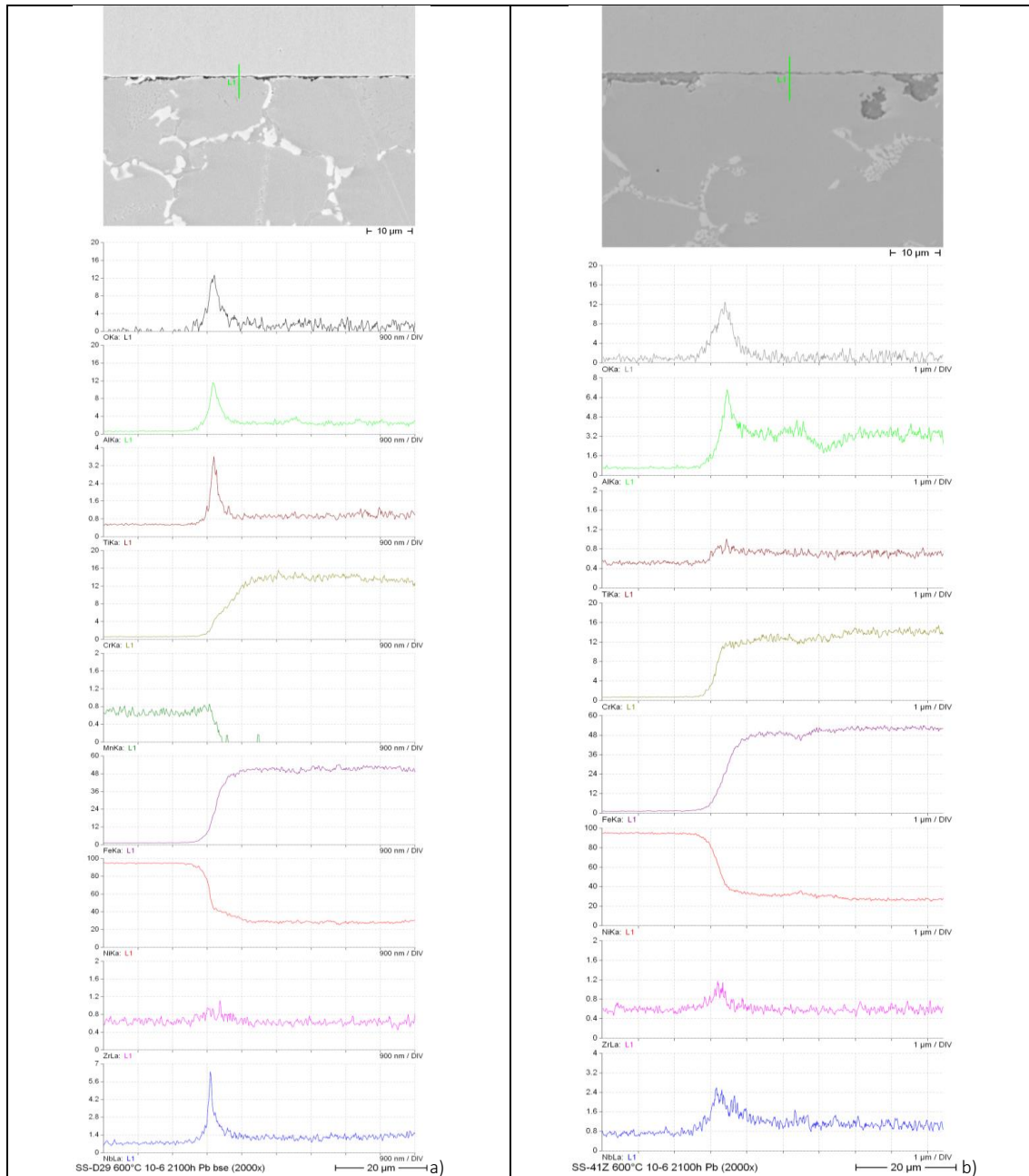
Fig. 3.7.4: EDX line scans of the thin oxide scale grown on the model alloys $Fe_{45}Ni_{32}Cr_{14}Al_3NbTiZrMn$ (a) and $Fe_{45}Ni_{32}Cr_{14}Al_4NbTiZr$ (b).

Involved Staff:

DP W. An, Dr. R. Fetzer, Y. Nakabo (Internship), A. Neukirch, Dr. A. Heinzel, DI. M. Hochberg, Dr. A. Jianu, DI (Fh) F. Lang, Prof. G. Müller, Dr. G. Schumacher (Gast), H. Shi (SCS-PhD student), W. Zhen (SCS-PhD student), A. Sivkovich, **Dr. A. Weisenburger**, DI (Fh) F. Zimmermann.

4 Energy Efficiency, Materials and Resources (EMR): Energy-Efficient Processes – Materials Processing with Microwaves –

4.1 Characterization of dielectric materials

4.1.1 In-situ dielectric characterization and calorimetry of pressurized chemical reaction

Owing to the selective and volumetric nature of heating the application of microwave enables faster and more energy efficient processing in various fields of applications such as for example microwave chemistry. For the successful design of microwave assisted chemical reactors, beside the knowledge of dielectric properties, calorimetric information as well as information about the reaction kinetics are important. Calorimetric measurements always imply samples under test being in thermodynamic equilibrium with its environment. Since in case of microwave heating this never happens, beside an accurate measurement of the microwave power, absorbed in the system, the detailed knowledge about its thermodynamic behavior is mandatory.

Till know only qualitative calorimetric measurements, combined with dielectric characterization in microwave cavities, had been reported. Here, the sensitive microwave power measurements were extended with heat transfer simulations to enable a more quantitative estimation of the power absorbed in the material under test.

To account for the heat transfer losses from the sample heated with microwave the COMSOL Multiphysics software package was employed (see Fig. 4.1.1). For that problem, the heat source defined as the microwave energy dissipated in the dielectric material, was estimated by means of electromagnetic simulations using CST Microwave Studio.
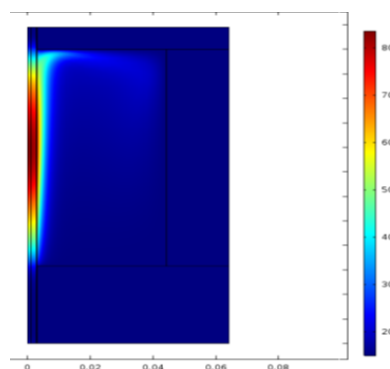
Fig. 4.1.1: COMSOL simulation of the temperature distribution in the cavity.

4.1.2 Ku-Band Fabry Perot-Resonator

To enable the dielectric characterization of low loss liquid as well as solid samples at frequencies close to the ISM Band at 24.125 GHz, a so called Fabry Perot Resonator has been designed and build (see Fig. 4.1.2).

This is an open resonator concept consisting of a planar and a spherical aluminum mirror. The cavity built reveals a measured quality factor of about 85000 that provides a resolution limit of the dielectric loss tangents at values as low as 10^{-4} as could be demonstrate for a low loss sample of CaF_2 single crystal (see Fig. 4.1.3). The planar mirror which holds the material under test can be heated to temperatures up to 150°C and therefore allows temperature depended in-situ measurements as well. The measurement procedure as well as the data interpretation is fully computer controlled, what allows a reproducible and comfortable data acquisition.
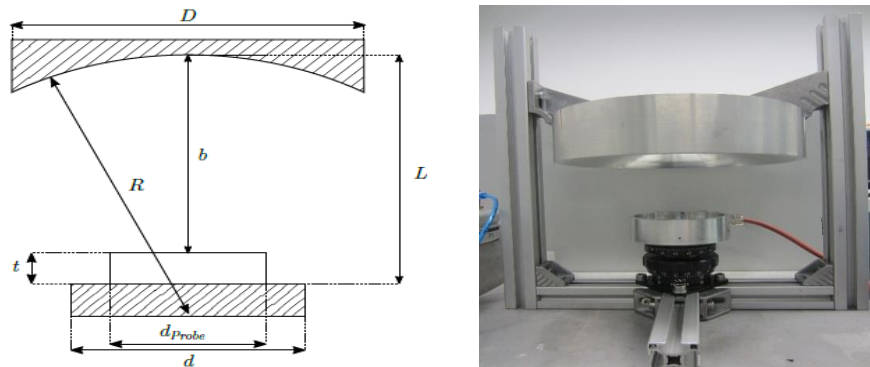
Fig. 4.1.2: Scheme (left) and photo (right) of the Ku-Band Fabry Perot resonator.
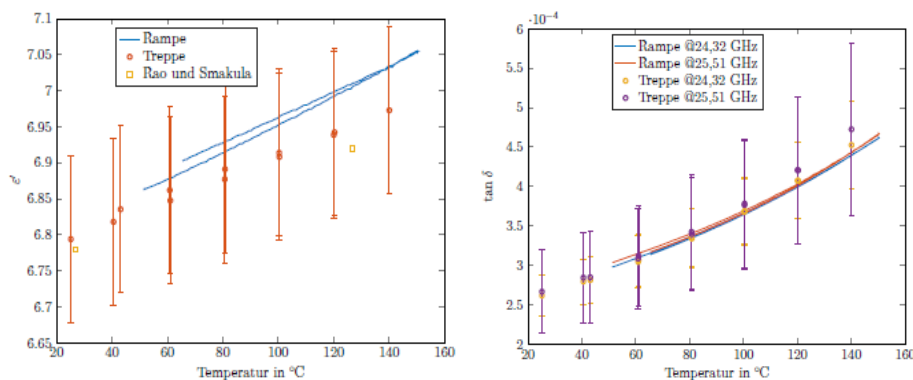
Fig. 4.1.3: Dielectric constant (left) and dielectric loss factor (right) of a CaF_2 single crystal as a function of temperature for continuous and stepwise heating at 24 GHz.

4.2 Plasma chemistry

End of 2016 a new lab was established for investigations on microwave assisted plasma chemistry. Most of the necessary infrastructure has already been installed (see Fig. 4.2.1). The first plasma and experimental investigations on plasma assisted CO_2 conversion are planned for 2017. For the perspective chemical reactions the optimal microwave sustained plasma scenarios and applicators will be developed. For that purpose the equipment of the new plasma laboratory is under development. Already now a 6 kW microwave plasma source which can operate at atmospheric pressure is available, that will allow plasma and gas temperatures up to 3500 K. For analysis of reaction products optical emission spectrometer Ocean Optics HR2000+ with the working wavelength rage of 200 to 1100 nm will be used. Mass flow controller will allow the precise control of feeding gases like argon, air, carbon dioxide and hydrogen. The laboratory is equipped with a system for removal of exhaust gases and a gas monitoring and alarm system.
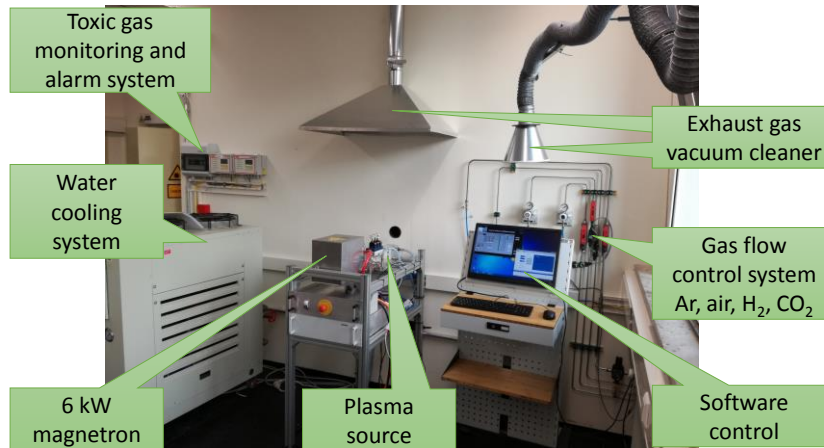
Fig. 4.2.1: Photo of the plasma laboratory.

4.3 Microwave assisted extraction of microalgae

The extraction of oil from micro algae provides an alternative, regenerative source of liquid fuels. First experiments on the treatment of algae cells with microwave radiation have motivated the development of an advanced microwave applicator operating in pulse regime at a frequency of 2.45 GHz. A short pulse of high power microwave being absorbed in the algae cells facilitates greatly the release of oil to the surrounding medium. For short microwave pulses heating of the surrounding medium is negligibly and the microwave energy is spent fast and for oil extraction solely. It makes such an approach very energy efficient and attractive for industrial application. The scheme of the experiment is presented in Fig. 4.3.1, where the main element is the microwave cavity (3). The magnetron source (1) isolated with a circulator (9) couples the wave into the cavity (3). The algae suspension (4) is pumped (2) through the cavity and collected (4) for further analysis. The temperature of the suspension (5) is controlled at the input and output of the cavity with thermocouples (5). The absorbed energy is measured by use of a directional coupler (8) and an oscilloscope (7).
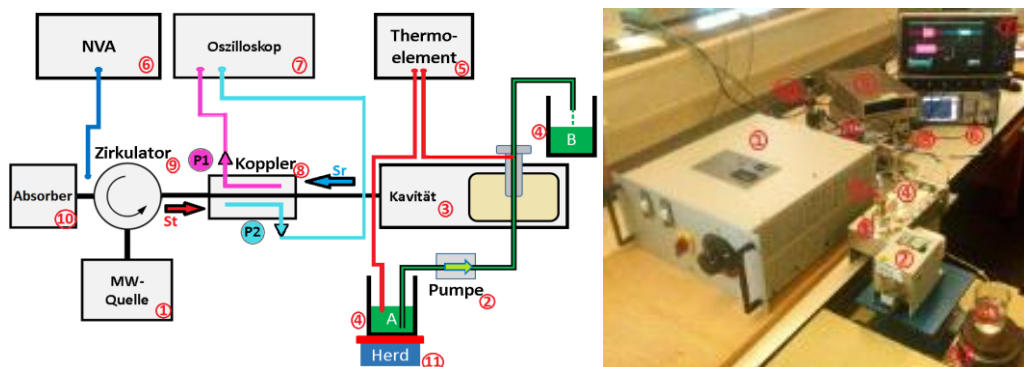
Fig. 4.3.1: Scheme of experiment on the oil extraction from algae by means of pulsed microwave radiation (left) and the photo of the experiment in the lab (right).

The microwave applicator design and fabrication was the central part of the present work. The design is based on an optimized cylindrical cavity operating at the TM_{010} mode. This provides the concentration of the microwave energy in the algae suspension flowing through the region where the electric field is maximal. Additionally the design features a tuning element allowing to shift the resonance frequency and to maximize the energy coupling into the algae dispersion for different dispersion media.

4.4 Collaboration Projects

4.4.3 Microwave assisted selective bonding

In the frame of a collaborative project with CARL MEISER GMBH & CO.KG on the microwave assisted bonding of thin decorative technical textiles to plastic substrates the model of the heat transfer and microwave absorption in the coating-glue-substrate sandwich structure (Fig. 4.4.1) was developed. This project has been funded by the Federal Ministry of Economy Affairs and Energy within the Central Innovation Programme for SMEs
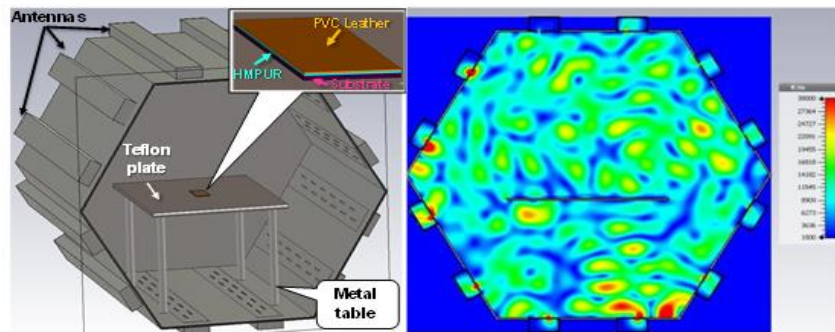
Fig. 4.4.1: Electromagnetic simulation of the HEPHAISITSOS VHM100/100 oven. Geometrie of the model (left), distribution of the electric field in a vertical cross section (right).

The project objective was the process optimization by variation of the microwave susceptibility of a polyurethane hot-melt (HMPUR) adhesive, the launched microwave power and the radiation time, respectively to enable a good selective heating within the sandwich structure (see Fig. 4.4.2) and a temperature profile, resulting in a high quality bonding.
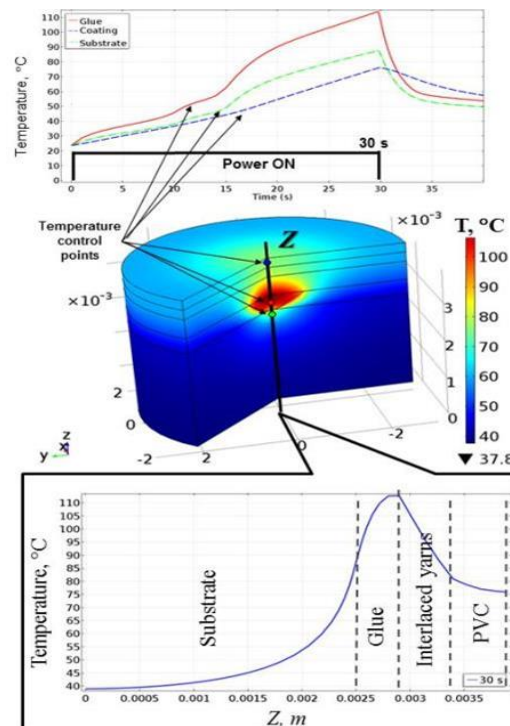
Fig. 4.4.2: Result on heat transfer modelling with COMSOL Multiphysics.

A variation of the HMPUR susceptibility has been achieved by blending it with carbon fibers in the range from 1 wt.% to 4 wt.%. The modelled coating was a PVC synthetic leather with a PET interlaced yarn textile layer at the wrong side. The substrate was a dense ABS-PC material. For process analysis the absorbed microwave power was estimated by use of CST Microwave Studio (Fig. 4.4.1). The resulting temperature fields inside the materials were modelled by use of COMSOL Multiphysics taking the results from CST simulations as heat source (Fig. 4.4.2).

After 30 seconds of heating the resulting temperature profile within the sandwich structure of only 4 mm in thickness enables the curing of the HMPUR adhesive at 110 °C whereas the coating material remains at lower temperatures with no thermal damaged. The temperature difference of 40° C between the glue and coating domains due to selective heating is remarkable, accounting the distance between them of about 1 mm only (see Fig. 4.4.2). For the found optimal heating scenario and glue formulation the microwave assisted coating of a Land Rover glove-box cover was successfully demonstrated (see photo in Fig. 4.4.3).

Fig. 4.4.3: Result on microwave assisted coating of Land Rover glove-box cover.

4.4.4 SYMBIOPTIMA

The KIT task within the H2020-SPIRE-2015 European project SYMBIOPTIMA is to support the development of an industrial scale microwave reactor for the recycling of PET plastic waste. The objective is the energy efficient microwave assisted chemical depolymerization of the polyethylene terephthalate (PET) into its monomers terephthalic acid (PTA) and ethylene glycol.

The basis for that design is a precise knowledge of the dielectric properties of the reactive mixture as well as the materials of the applicator within the working temperature range. For this purpose an advanced dielectric measurement setup for in-situ dielectric characterization of lossy liquids under microwave heating conditions and under pressure conditions had been developed. Here the cavity perturbation method based on the simultaneous excitation of two modes, TM_{010} and TE_{111}, at a frequency of about 2.45 GHz is applied. That allows the dielectric characterization of high permittivity materials with sufficient accuracy, not feasible with the classical analytical perturbation method. To do so the TM_{010}-mode was used to measure the dielectric constant and of the TE_{111}-mode for the dielectric loss, respectively. The following figure shows the designed test-set.
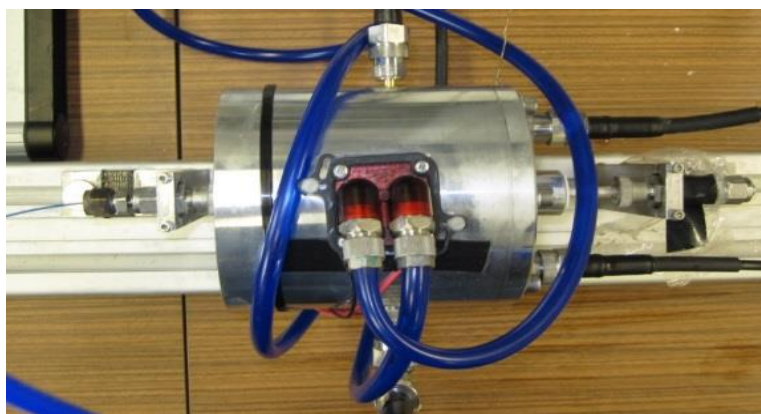
Fig. 4.4.4: Test setup for dielectric measurements.

The quartz tube sample holder was closed at both ends with Swagelok connectors, which can withstand a pressure of 18 bars. For active control and stabilization of the cavity temperature, two Peltier elements of type QC-241-1.0-3.9M were installed. The sample temperature was measured by use of a fibre optic sensor located in the centre of the sample.
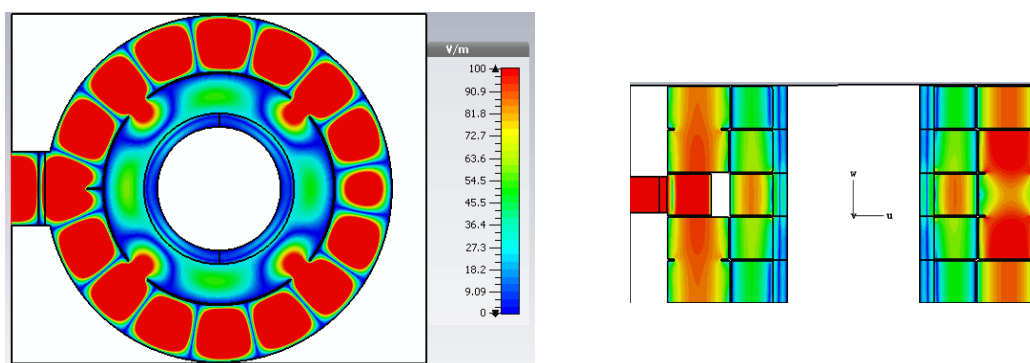
Fig. 4.4.5: Simulated field distribution in a tubular chemical reactor

Based on the measured dielectric properties and using common 3D software tools, an optimised industrial scale microwave applicator design has been developed and optimized. The achieved design offers a well-defined and even distribution of the power from a single magnetron source within the applicator and the process material, as can be shown from simulation results (see Fig. 4.4.5). This can be achieved by using a network based on rectangular waveguides, mutually connected by coupling ports that were optimized in size and position. This applicator design enables high field homogeneity in azimuthal as well as axial direction in a tubular reactor. At the same time the energy efficiency is high with less than 10 % reflected power in the overall range of expected material permittivities.

4.4.5   InnoConTemp

Microwave heating has a great potential to replace classical heating processes, such as convection or radiation heating. The main advantage is the possibility to heat in the whole volume of the product, therefore the slow thermal conduction doesn't limit the heating process. Compared to a classical heating system both energy consumption and cycle time can be reduced. However, there aren't a lot of microwave systems implemented in industry because of insufficient temperature uniformity in the product.

Therefore, the aim of the technology transfer project InnoConTeMP (Innovative Control of Temperature Distributions for Microwave heating Processes), which is co-financed by the KIT Innovation Fund and has started in September 2016, is to improve the temperature distribution of a workpiece in the HEPHAISTOS systems licensed to the industry partner Vötsch Industrietechnik GmbH. As a starting point some ideas of the FLAME project are used. The idea is to control the power levels of each distributed antenna in the HEPHAISTOS oven with an intelligent algorithm, so that the temperature distribution of the product is improved. One or more of the three different control algorithms, which were developed within the FLAME project, will be used and optimized: model predictive control (MPC), neural network control (NNC) and reinforcement learning control (RLC). The improvement compared to a classical PID controller, that only regulates the power levels of all microwave sources to the same value (no independent control of each source), is shown in Fig. 4.4.6. There's a much smaller temperature difference ΔT between all measured values by using the model predictive controller.
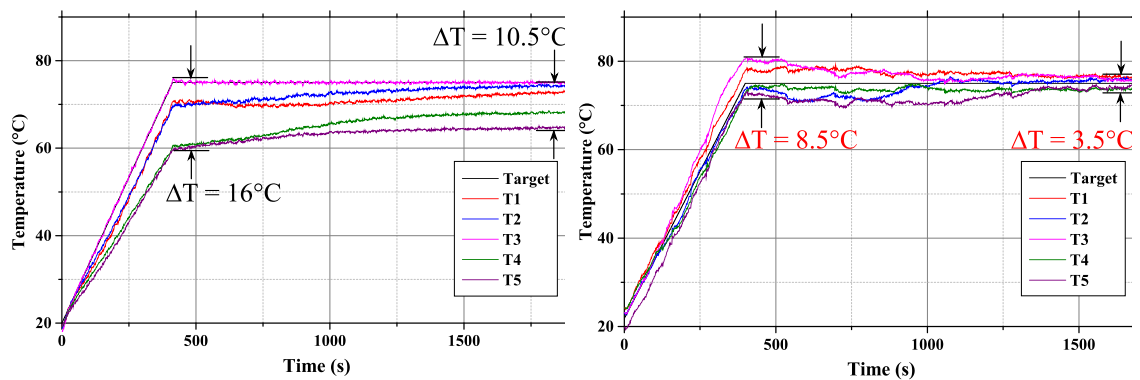
Fig. 4.4.6: Comparison of a PID (proportional–integral–derivative) controller (left) and an innovative model predictive controller (right).

At the end of the project the control algorithms will be implemented in the control software S!MPAC of our partner Vötsch, so that the HEPHAISTOS systems can be sold with an improved temperature homogeneity. This will allow to develop new applications where heating uniformity is more critical and could not be achieved with existing technology.

Involved Staff:

K. Ayhan, L. Baureis, Prof. J. Jelonnek, Dr. T. Kayser, S. Layer, Dr. B. Lepers, **Dr. G. Link**, D. Neumaier, V. Nuss, Ramopoulos, T. Seitz, S. Soldatov, Y. Sun, Frau S. Wadle

Journal Publications

Nuclear Fusion (FUSION)

A. Abou-Sena, F. Arbeiter, S. Baumgaertner, T. Boettcher, A. Heinzel, H. Piecha, K. Zinn (2016), Chemical compatibility of Eurofer steel with sodium-potassium NaK-78 eutectic alloy. Fusion Engineering and Design, vol. 103, 31-37.

A.V. Arzhannikov, N.S. Ginzburg, P.V. Kalinin, S.A. Kuznetsov, A.M. Malkin, N.Y. Peskov, A.S. Sergeev, S.L. Sinitsky, V.D. Stepanov, M. Thumm, V.Y. Zaslavsky (2016), Using Two-Dimensional Distributed Feedback for Synchronization of Radiation from Two Parallel-Sheet Electron Beams in a Free-Electron Maser, Physical review letters, vol. 117 (11), p. 114801.

A.V. Arzhannikov, A.V. Burdakov, V.S. Burmasov, I.A. Ivanov, A.A. Kasatov, S.A. Kuznetsov, M.A. Makarov, K.I. Mekler, S.V. Polosatkin, S.S. Popov, V.V. Postupaev, A.F. Rovenskikh, S.L. Sinitsky, V.F. Sklyarov, V.D. Stepanov, I.V. Timofeev, M.K.A. Thumm (2016), Dynamics and Spectral Composition of Subterahertz Emission From Plasma Column Due to Two-Stream Instability of Strong Relativistic Electron Beam, IEEE Transactions on Terahertz Science and Technology, vol. 6 (2), 245-252.

J. Franck, K.A. Avramidis, G. Gantenbein, S. Illy, I.Gr. Pagonakis, M. Thumm, J. Jelonnek (2016), Direct voltage depression calculation of arbitrary electron beams in misaligned coaxial gyrotron cavities, IEEE Transactions on Elctron Devices, vol. 63, pp. 3740-3746.

I. O. Girka, M. Thumm, (2016), Excitation of azimuthal surface waves in the electron cyclotron frequency range by a rotating electron beam in presence of dissipation, Physics of plasmas, vol. 23 (12), 122124.

I. O. Girka, M. Thumm, (2016), Excitation of Azimuthal Surface Waves Above the Upper-Hybrid Frequency by External Relativistic Flows of Electrons in Coaxial Plasma-Vacuum Waveguide, IEEE transactions on plasma science, vol. 44 (11), pp. 2859-2866.

I.O. Girka, V.O. Girka, R.D. Sydora, M. Thumm (2016), Instability of surface electron cyclotron TM-modes influenced by non-monochromatic alternating electric field, Physics of Plasmas, vol. 23 (6), pp. 062106/1-9.

Y. Igitkhanov, R. Fetzer, B. Bazylev (2016), Effect of heat loads on the plasma facing components of demo, Fusion engineering and design, vol. 109-111 (Part A), pp. 768-772.

Z.C. Ioannidis, K.A. Avramidis, I.G. Tigelis (2016), Selectivity Properties of Coaxial Gyrotron Cavities With Mode Converting Corrugations, IEEE Transactions on Electron Devices, vol. 63 (3), 1299-1306.

P.C. Kalaria, K.A. Avramidis, J. Franck, G. Gantenbein, S. Illy, I.Gr. Pagonakis, M. Thumm, J. Jelonnek (2016), Systematic cavity design approach for a multi-frequency gyrotron for DEMO and study of its RF behavior, Physics of Plasmas, vol. 23, pp. 092503-9.

J. Jelonnek, G. Gantenbein, K. Avramidis, J. Franck, S. Illy, Z. Ioannidis, J. Jin, P. Kalaria, I. Pagonakis, S. Ruess, T. Rzesnicki, T. Scherer, M. Schmid, D. Strauss, C. Wu, M. Thumm, Gyrotron-Forschung und –Entwicklung am KIT, Vakuum in Forschung und Praxis, vol. 28, 6, pp. 21-27, 2016.

I.G. Pagonakis, S. Illy, M. Thumm (2016), Influence of emitter ring manufacturing tolerances on electron beam quality of high power gyrotrons, Physics of plasmas, vol. 23 (8), p. 083103.

I.Gr. Pagonakis, C. Wu, S. Illy, J. Jelonnek (2016), Multistage depressed collector conceptual design for thin magnetically confined electron beams, Physics of Plasmas, vol. 23, pp. 043114-8.

I.Gr. Pagonakis, B. Piosczyk, J. Zhang, S. Illy, T. Rzesnicki, J.P. Hogge, K. Avramidis, G. Gantenbein, M. Thumm, J. Jelonnek (2016), Electron trapping mechanisms in magnetron injection guns, Physics of Plasmas, vol. 23, pp. 023105/1-11.

S. Ruess, I.Gr. Pagonakis, G. Gantenbein, S. Illy, T. Kobarg, T. Rzesnicki, M. Thumm, J. Weggen, J. Jelonnek (2016), An inverse magnetron injection gun for the KIT 2 MW coaxial- cavity gyrotron, IEEE Transactions on Electron Devices, vol. 63, pp. 2104-2109.

R. Seviour, D. Shiffler, J. Jelonnek, C. Grabowski, S. Hemmady, S. Ang, L.K. Ricky (2016), Guest editorial the sixteenth special issue on high-power microwave generation, IEEE Transactions on Plasma Science, vol. 44, 8, pp. 1257.

G. Singh Baghel, S. Illy, M.V. Kartikeyan, (2016), I/O System for A 77/154-GHz, 0.5-MW Dual Regime Gyrotron, IEEE transactions on electron devices, vol. 63 (11), pp. 4459 – 4465.

R.C. Wolf, C.D. Beidler, A. Dinklage, P. Helander, H.P. Laqua, F. Schauer, T. Sunn Pedersen, F. Warmer, Wendelstein 7-X Team (2016), Wendelstein 7-X Program - Demonstration of a Stellarator Option for Fusion Energy, IEEE transactions on plasma science,vol. 44 (9), pp. 1466-1471.

J. Zhang, S. Illy, I.Gr. Pagonakis, K.A. Avramidis, M. Thumm, J. Jelonnek (2016), Influence of emitter surface roughness on high power fusion gyrotron operation, Nuclear Fusion, vol. 56, pp. 026002/2-9.

Scientific Reports

M. Thumm, State-of-the-Art of High Power Gyro-Devices and Free Electron Masers. Update 2015. (KIT Scientific Reports; 7717), 2016, KIT Scientific Publishing, Karlsruhe.

Renewable Energy (RE)

A. Abánades, R.K. Rathnam, T. Geißler, A. Heinzel, K. Mehravaran, G. Müller, M. Plevan, C. Rubbia, D. Salmieri, L. Stoppel, S. Stückrad, A. Weisenburger, H. Wenninger, T. Wetzel (2016), Development of methane decarbonisation based on liquid metal technology for CO_2-free production of hydrogen, International Journal of Hydrogen Energy / Special Issue on Progress in Hydrogen Production and Applications, vol. 41 (19), pp. 8159–8167.

M.A. de Menorval, F.M. Andre, A. Silve, C. Dalmay, O. Francais, B.L. Pioufle, L.M. Mir (2016), Electric pulses: a flexible tool to manipulate cytosolic calcium concentrations and generate spontaneous-like calcium oscillations in mesenchymal stem cells, Scientific reports, vol. 6, p. 32331.

A. Golberg, M. Sack, J. Teissie, G. Pataro, U. Pliquett, G. Saulis, S. Töpfl, D. Miklavcic, E. Vorobiev, W. Frey (2016), Energy-efficient biomass processing with pulsed electric fields for bioeconomy and sustainable development, Biotechnology for biofuels, 9 (1), p. 508.

M. Hochberg, M. Sack, G. Mueller (2016), A Test Environment for Power Semiconductor Devices Using a Gate-Boosting Circuit, IEEE transactions on plasma science, vol. 44 (10), pp. 2030-2034.

M. Polikovsky, F. Fernand, M. Sack, W. Frey, G. Müller, A. Golberg (2016), Towards marine biorefineries: Selective proteins extractions from marine macroalgae Ulva with pulsed electric fields, Innovative food science & emerging technologies, vol. 37, pp. 194-200.

J. Raso, W. Frey, G. Ferrari, G. Pataro, D. Knorr, J. Teissie, D. Miklavcic, (2016), Recommendations guidelines on the key information to be reported in studies of application of PEF technology in food and biotechnological processes, Innovative food science & emerging technologies, vol. 37, pp. 312-321.

M. Sack, G. Mueller (2016), Scaled design of PEF treatment reactors for electroporation-assisted extraction processes, Innovative food science & emerging technologies, vol. 37, pp. 400-406.

A. Silve, I. Leray, C. Poignard, L.M. Mir, (2016), Impact of external medium conductivity on cell membrane electropermeabilization by microsecond and nanosecond electric pulses, Scientific Reports, vol. 6, p. 19957.

R. Straessner, A. Silve, C. Eing, S. Rocke, R. Wuestner, K. Leber, G. Mueller, W. Frey (2016), Microalgae precipitation in treatment chambers during pulsed electric field (PEF) processing, Innovative food science & emerging technologies, vol. 37, pp. 391-399.

Safety Research for Nuclear Reactors (NUSAFE)

V. Altsybeyev, V. Engelko, A. Ovsyannikov, D. Ovsyannikov, V. Ponomarev, R. Fetzer, G. Mueller (2016), Numerical simulation of a triode source of intense radial converging electron beam, Journal of applied physics, vol. 120 (14), p. 143301.

A. Heinzel, A. Weisenburger, G. Müller (2016), Long-term corrosion tests of Ti_3SiC_2 and Ti_2AlC in oxygen containing LBE at temperatures up to 700 °C, Journal of nuclear materials, vol. 482, pp. 114 - 123.

A. Heinzel, G. Müller, A. Weisenburger (2016), Corrosion behaviour of welds and Ta in liquid lead, Journal of Nuclear Materials, vol. 469, pp. 62-71.

A. Jianu, R. Fetzer, A. Weisenburger, S- Doyle, M. Bruns, A. Heinzel, P. Hosemann, G. Mueller (2016), Stability domain of alumina thermally grown on Fe-Cr-Al-based model alloys and modified surface layers exposed to oxygen-containing molten Pb, Journal of nuclear materials, vol. 470, pp. 68-75.

Energy Efficiency, Materials and Resources (EMR)

M.N. Hassan, M.M. Mahmoud, G. Link, A.A. El-Fattah, S.H. Kandil, (2016), Sintering of naturally derived hydroxyapatite using high frequency microwave processing, Journal of Alloys and Compounds, vol. 682, pp. 107-114.

S. Soldatov, M. Umminger, A. Heinzel, G. Link, B. Lepers, J. Jelonnek (2016), Dielectric characterization of concrete at high temperatures, Cement and concrete composites, vol. 73, pp. 54–61.

Appendix

Equipment, Teaching Activities and Staff

IHM is equipped with a workstation cluster and a large number of experimental installations: KEA, KEA-ZAR, three GESA machines, eight COSTA devices, one abrasion and one erosion teststand, two gyrotron test facilities with one common power supply and microwave-tight measurement chamber, one compact technology gyrotron (30 GHz, 15 kW, continuous wave (CW)), several 2.45 GHz applicators of the HEPHAISTOS series, one 0,915 GHz, 60 kW magnetron system, one 5.8 GHz, 3 kW klystron installation and a low power microwave laboratory with several vectorial network analysers.

The project FULGOR, targeting for a renewal of the KIT gyrotron teststand is progressing. In 2013, an agreement on the project structure including the involvement of the KIT project and quality management has been achieved. The final start of the procurement of the equipment was in 2014.

Prof. John Jelonnek has continued to teach the lecture course entitled "High Power Microwave Technologies (Hochleistungsmikrowellentechnik)" for Master students at KIT. Prof. Georg Müller has continued to teach the lecture on "Pulsed Power Technologies and Applications" at KIT. Dr. Gerd Gantenbein has been teaching the part "heating and current drive" of the lecture "Fusionstechnologie B" by Prof. R. Stieglitz, IFRT. Dr.-Ing. Martin Sack hold the lecture course "Elektronische Systeme und EMV" at KIT.

At the turn of the year 2016/2017 the total staff with regular positions amounted to 38 (16 academic staff members, 12 engineers and 10 technical staff member and others).

In addition 10 academic staff members, 1 engineer and 2 technical staff members (and others) were financed by acquired third party budget.

In course of 2016, 3 guest scientists, 13 PhD students (1 of KIT-Campus South, 7 of KIT-Campus North, 5 Scholarship, 1 in cooperation with IPP Greifswald), 4 DHBW student, 1 trainee in physics laboratory and 4 trainees in the mechanical and electronics workshops worked in the IHM. 7 Master students have been hosted at IHM and 12 Bachelor student has been at IHM during 2016.

Strategical Events, Scientific Honors and Awards

Martin Hochberg received the "Tom R. Burkes outstanding Graduate Student Award in the field of solid state power modulators and analyzing gate-boosting circuits for fast switching", 2016 IEEE Int. Power Modulator and High Voltage Conference, San Francisco, CA, USA.

Martin Hochberg received the "Outstanding Young Researcher Awards for paper presentation", 6th Euro-Asian Pulsed Power Conference, Portugal.

Andreas Schlaich received the "ICOPS 2016 NPSS Student Paper Awards", Banff, Canada.

Prof. Manfred Thumm with Prof. Igor O. Girka, "International Publicaton Encouragement Award 2016".

Dr.Ing. habil. Martin Sack successfully completed his habilitation at KIT´s faculty on Electrical Engineering and Information Technology (ETIT), in 2016. He now represents the topic on electromagnetic compatibility.

Longlasting Co-operations with Industries, Universities and Research Institutes

- Basics of the interaction between electrical fields and cells (Bioelectrics) in the frame of the International Bioelectrics Consortium with Old Dominion University Norfolk, USA; Kumamoto University, Japan; University of Missouri Columbia, USA; Institute Gustave-Roussy and University of Paris XI, Villejuif, France; University of Toulouse, Toulouse, France, Leibniz Institute for Plasma Science and Technology, Greifswald, Germany.

- Desinfection of hospital wastewater by pulsed electric field treatment in cooperation with University of Mainz and Eisenmann AG.

- Integration of the electroporation process for sugar production with SÜDZUCKER AG.

- Development of protection against corrosion in liquid metal cooled reactor systems in the following EU-Projectes: LEADER, GETMAT, MATTER, SEARCH (Partner: CEA, ENEA, SCK-CEN, CIEMAT).

- Development of large area pulsed electron beam devices in collaboration with the Efremov Institute, St. Petersburg, Russia.

- Experiments on liquid Pb and PbBi-cooling of reactor systems with the Institute for Physics and Power Engineering (IPPE), Obninsk, Russia.

- Development, installation and test of the complete 10 MW, 140 GHz ECRH Systems for continuous wave operation at the stellarator Wendelstein W7-X in collaboration with the Max-Planck-Institute for Plasmaphysics (IPP) Greifswald and the Institute of Interfacial Process Engineering and Plasma Technology (Institut für Grenzflächenverfahrenstechnik und Plasmatechnologie, IGVP) of the University of Stuttgart.

- Development of the European ITER Gyrotrons in the frame of the European GYrotron Consortium (EGYC) and coordinated by Fusion for Energy (F4E). The other members of the Consortium are CRPP, EPFL Lausanne, Switzerland, CNR Milano, Italy, ENEA, Frascati, Italy, HELLAS-Assoc. EURATOM (NTUA/NKUA Athens), Greece. The industrial partner is the microwave tube company Thales Electron Devices (TED) in Paris, France.

- Development of new diagnostic systems for improvement of electron guns for gyrotrons and cavity interaction calculations in collaboration with the St. Petersburg Polytechical University, Russia and the University of Latvia, Latvia.

- Development of Microwave Systems of the HEPHAISTOS Series for materials processing with microwaves with the Company Vötsch Industrietechnik GmbH, Reiskirchen.

The Institute for Pulsed Power and Microwave Technology (Institut für Hochleis-tungsimpuls- und Mikro-wellentechnik (IHM)) is doing research in the areas of pulsed power and high-power microwave technologies. Both, research and development of high power sources as well as related applications are in the focus. Applications for pulsed power technologies are ranging from materials processing to bioelectrics. High power microwave technologies are focusing on RF sources (gyrotrons) for electron cyclotron resonance heating of magnetically confined plasmas and on applications for materials processing at microwave frequencies.

The IHM is doing research, development, academic education, and, in collabora-tion with the KIT Division IMA and industrial partners, the technology transfer. The IHM is focusing on the long term research goals of the German Helmholtz As-sociation (HGF). During the ongoing program oriented research period (POF3) of HGF (2015 – 2020), IHM is working in the research field ENERGY. Research projects are running within following four HGF programs: "Energy Efficiency, Materials and Resources (EMR)"; "Nuclear Fusion (FUSION)", "Nuclear Waste Management, Safety and Radiation Research (NUSAFE)" and "Renewable Energies (RE)".

During 2016, R&D work has been done in the following areas: fundamental theo-retical and experimental research on the generation of intense electron beams, strong electromagnetic fields and their interaction with biomass, materials and plasmas; application of those methods in the areas of energy production through controlled thermonuclear fusion in magneti¬cally confined plasmas, in material processing and in energy technology.